HYDRODYNAMIC LUBRICATION OF FLOATING VALVE PLATE IN AN AXIAL PISTON PUMP

by

David Richardson

A Dissertation

Submitted to the Faculty of Purdue University

In Partial Fulfillment of the Requirements for the degree of

Doctor of Philosophy

School of Mechanical Engineering

West Lafayette, Indiana

May 2019

THE PURDUE UNIVERSITY GRADUATE SCHOOL
STATEMENT OF COMMITTEE APPROVAL

Dr. Farshid Sadeghi, Chair
School of Mechanical Engineering
Dr. Steven Wereley
School of Mechanical Engineering
Dr. Charles Krousgrill
School of Mechanical Engineering
Dr. Andrea Vacca
School of Agricultural and Biological Engineering

Approved by:
Dr. Jay P. Gore
Head of the Graduate Program

To my Friends and Family:

Thank you for your support.

ACKNOWLEDGMENTS

My work at Purdue was made possible through the financial support of Honeywell. I am particularly grateful to Mr. Richard Rateick and Mr. Scott Rowan from Honeywell who have constantly guided and supported me throughout my research process.

I thank Professor Farshid Sadeghi, for his mentorship and direction in all of my research challenges and throughout various aspects of my life. He is an invaluable resource to me.

Thanks to all my colleagues and friends in the Mechanical Engineering Tribology Lab, especially, Matthew Brouwer, Neil Paulson, Arnab Ghosh, Aditya Walvekar, Abdullah Alazemi, Lijun Cao, Sina Mobasher Moghaddam, Zamzam Gholmohamadi, Dallin Morris, Akhil Vijay, Steve Lorenz, Arman Ahmadi, Akshat Sharma, Xin Xu, Kushagra Singh, and Wyatt Peterson. Also I thank my friend Joseph Fisch with whom I have gone on many enjoyable adventures. Thank you Noelle, Jayne, and Mary, you have brough so much joy into my life.

Finally, and most importantly I thank my wife Ashley. Your constant support throughout this process has made it infinitely more gratifying. I love you, and I am most grateful for the guidance and encouragement you have given me to take chances and continue my pursuit for higher education.

TABLE OF CONTENTS

LIST OF TABLES

LIST OF FIGURES

NOMENCLATURE

Symbol	Units	Description
η_0	Pa s	reference viscosity
η		non-dimensional viscosity ($\bar{\eta}/\eta_0$)
$\bar{\eta}$	Pa s	viscosity
ω	rad/s	rotational velocity
R_O	m	outer radius
R_I	m	inner radius
$\bar{r}$	m	radial position
r		non-dimensional radius ($\bar{r}/R_I$)
h_0	m	minimum film thickness
β	Pa	bulk modulus
h		non-dimensional film thickness ($\bar{h}/h_0$)
$\bar{h}$	m	film thickness
θ_n	rad	radial position
F		cavitation switching function
ϕ		non-dimensional density ratio($\bar{\rho}/\rho_C$)
$\bar{\rho}$	kg/m^3	density
ρ_C	kg/m^3	fluid density at the cavitation pressure
$\bar{P}$	Pa	gage pressure
P_a	Pa	atmospheric pressure
γ	Rad	angular width of transition pressure
λ	Rad	angular half width of piston
P_c	Pa	cavitation pressure
P		non-dimensional pressure ($(\bar{P} + P_a)/(P_a - P_c)$)
m		Slope of the instantaneous piston pressure near top and bottom dead center

ξ	Rad	Angular distances to and from the inlet and outlet ports on the valve plate
φ	Rad	Angular distance of valve plate to y-axis
θ	Rad	Angular distance of valve plate to x-axis
Z_{cm}	m	Vertical displacement of center of mass of valve plate
$x_{1,2,3,4}$	m	X-locations of balance pistons
$y_{1,2,3,4}$	m	Y-locations of balance piston
L	N	load
k	N/m	spring coefficient of balance piston
c	Ns/m	damping coefficient of balance piston
$x(t)$		Response amplitude at time t
n		Number of periods used in logarithmic decrement method
T		Period of vibration in logarithmic decrement method
δ		Logarithmic decrement of response amplitude
ζ		Damping ratio
ω_n	Hz	Natural frequency
M	kg	Mass of floating valve plate system
X	m	Distance from reformation boundary to pocket edge
Φ_k		Correlation function for PIV analysis
f_k		Grayscale intensity values for first image in image pair
g_k		Grayscale intensity values for second image in image pair
x	m	x-location inside of bearing pocket
y	m	y-location inside of bearing pocket
z	m	z-location inside of bearing pocket
V_z	m/s	Velocity in the z-direction
V_θ	m/s	Velocity in the theta-direction
V_r	m/s	Velocity in the r-direction
IM_i		Influence matrix and node i

p_{ref}	MPa	Reference pressure for elastic deformation
$\bar{T}$	K	Dimensional fluid temperature
$\overline{T_{cb}}$	K	Dimensional cylinder block temperature
$\overline{\overline{T_{vp}}}$	K	Dimensional valve plate temperature
T_0	K	Reference temperature
T_{cb}		Non-dimensional cylinder block temperature ($\overline{T_{cb}}/T_0$)
T		Non-dimensional fluid temperature ($\bar{T}/T_0$)
T_{vp}		Non-dimensional valve plate temperature ($\overline{T_{vp}}/T_0$)
u_{total}	m	Total elastic deformation of valve plate
h_{FLUID}	W/(m^2-K)	Fluid convection coefficient
k_{vp}	W/(m-K)	Valve plate thermal conductivity
C_{cb}	J/(Kg-K)	Cylinder block specific heat

ABSTRACT

Author: Richardson, David, W. PhD
Institution: Purdue University
Degree Received: May 2019
Title: Hydrodynamic Lubrication of Floating Valve Plate in an Axial Piston Pump
Committee Chair: Farshid Sadeghi

The valve plate/cylinder block interface in an axial piston pump is often subject to extreme pressures, which can cause wear of the valve plate and ultimately, failure of the pump. The purposes of this study were to: a) experimentally investigate the film thickness generated between a floating valve plate and cylinder block in situ using proximity probes, b) develop a model which can predict the motion, film thickness and pressures of the floating valve plate and corroborate with experimental results, c) investigate surface pockets to provide additional lubricant at the valve plate interface by measuring the flow velocities and cavitation areas in a thrust washer bearing, d) numerically investigate surface modifications of the floating valve plate to observe any changes in lubricant pressure, temperature, cavitation, or valve plate deformation. Two different test rigs were designed, developed and used to investigate the performance of axial piston pumps and surface pockets. The axial piston pump test rig (APTR) was designed to operate and measure the steady state conditions of an axial piston pump. The APTR utilizes three non-contact proximity probes to measure the valve plate motion and film thickness between the cylinder block at various speeds and pressures. A thrust washer test rig (TWTR) was developed to measure the cavitation areas and flow velocities of lubricant in a pocketed thrust washer using μPIV. Through a novel interpolation approach, the depths of the micro-particles in the bearing pocket were determined using an analytical model. Using this approach, the μPIV measured 2D velocity field was employed to develop a 3D velocity field, which illustrates the fluid motion inside a pocketed thrust bearing at various speeds and viscosities. A dynamic lubrication model was developed using the thermal Reynolds equation augmented with the JFO boundary condition and the energy equation to determine the pressure, cavitation regions and temperature of the lubricant at the valve plate cylinder block interface. The lubricating pressures were then coupled with the equations of motion of the floating valve plate to develop a dynamic lubrication model. The stiffness and damping coefficients of the floating valve plate system used in the dynamic

lubrication model were determined using a parametric study. The elastic deformation of the valve plate was also considered using the influence coefficient matrix approach. The experimental and analytical motion of the valve plate were then corroborated and found to be in good agreement. Four and eight pocket designs were then added as surface modifications to the floating valve plate in the dynamic lubrication model. The addition of surface modifications improved the lubricating conditions at the valve plate/cylinder block interface and resulted in increased minimum film thicknesses and lowered lubricant temperatures at the same operating conditions.

1. INTRODUCTION

1.1 Axial Piston Pump

The axial piston pump was designed and developed approximately four hundred years ago. Figure 1.1 illustrates the first axial piston pump designed by Ramelli [1588]. As the wheel T is driven by a water source, it also turns the pinion K. The lantern engages with the teeth of wheel P. The wheel A tilts to a specific angle and is along the same shaft as wheel P. There are four rods arranged circularly around the shaft of the wheel P. The rollers H and N rotate along the guide with the rods and guide them along the tilted wheel A. As the four rods move along the tilted wheel they move up and down and keep vertical by the rollers D. The pistons are set at the lowest end of the rods and enter the cylinders G, R, S, & Z under the water. The water enters the cylinders as the rods rise and are pushed into the chamber B as the rods fall. As the wheel T keeps rotating, the water is pressed to the container X through the pipe Q.

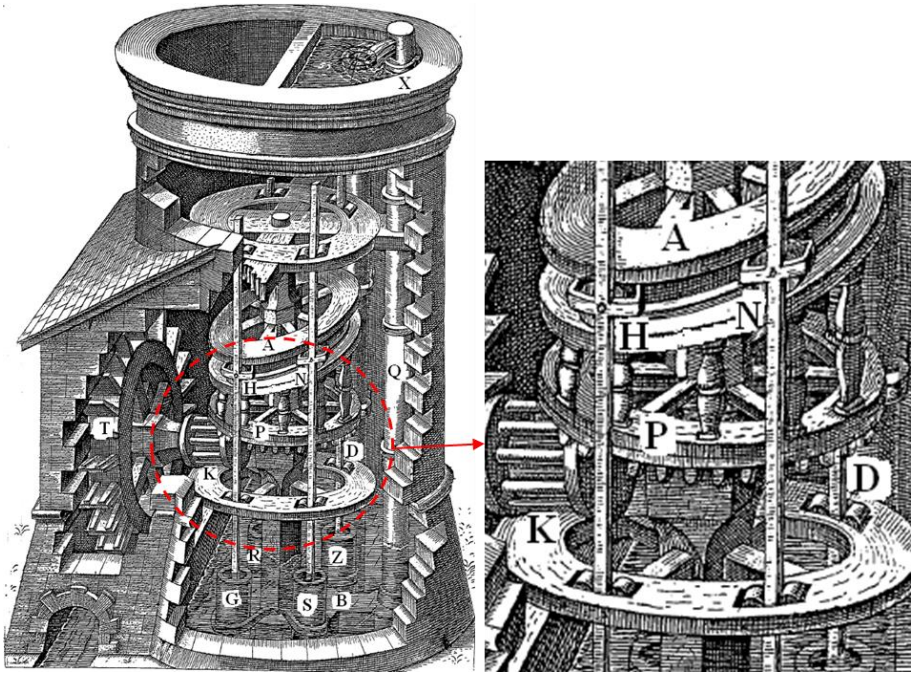

Figure 1.1: First Axial Piston Pump[Ramelli 1588]

The basic elements of the axial piston pump have not changed significantly and are quite similar to the first design. Figure 1.12 shows a schematic of a modern axial piston pump. One of

the main differences between the present pump and the original design described in Figure 1.1 is that rollers H & N are replaced by the slippers. In order to keep the slippers contacting with the swash plate, a hold-down device is necessary to be installed between the slippers and the pistons to keep the slippers moving stably. In addition, a valve plate is used to guide the fluid in and out of the pump instead of the chamber B in Figure 1.1. The details of axial piston pump are described comprehensively in Ivantysyn and Ivantysynova [2001].

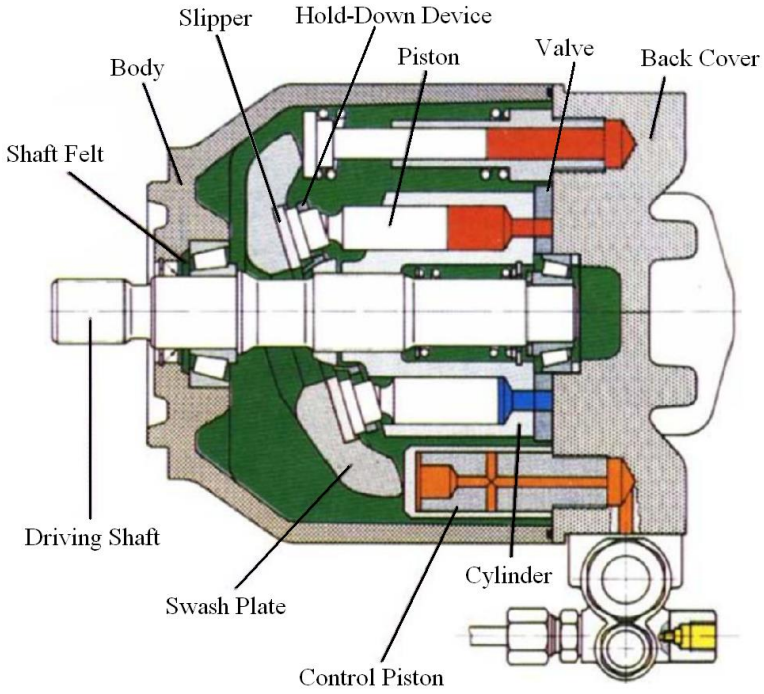

Figure 1.2: Section View of the Axial Piston Pump [Canbulut et al. 2009]

Many tribological interfaces can affect the overall performance of the axial piston. For example, the interface between the swash plate and the slipper has been investigated due to the wear that can occur on the slipper and swashplate. E. Koc et al. [1992] presented the experimental and theoretical investigation of the effect of clamping ratio and orifice size on the performance of slippers in an axial piston pump. Three different profiles of the slipper land were examined, including conical, outside of land polished, and inside and outside of land polished as shown in Figure 1.3. They showed that in order to let the slippers to move smoothly, the slippers require a slightly convex surface on the slipper running surface and a design that has no

connection between the piston and slipper can have the maximum resistance to tilt and make the slipper to run stably.

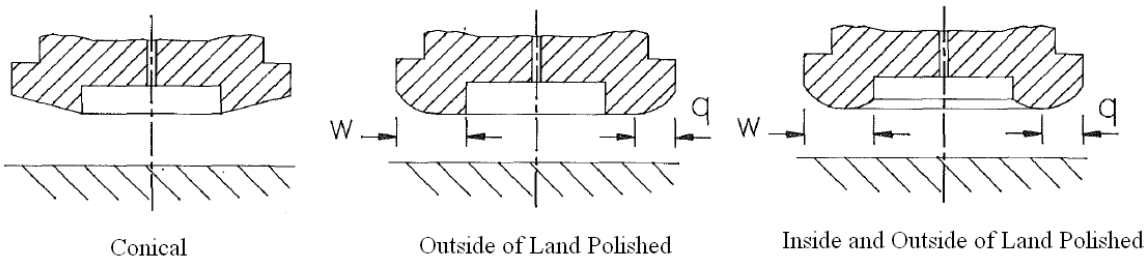

Figure 1.3: Cavitation in a Spiral Groove Thrust Bearing [Broman 2001]

In addition to the slipper and swash plate interface many researchers have investigated the cylinder block/valve plate interface. Zecchi and Ivantysynova [2012] have experimentally investigated the thermal deformation of the VP and its effect on the lubricating pressure. Using a grid of thermocouples on the valve plate they were able to map the temperature distribution across the valve plate in situ. The resulting temperatures were then used to calculate the thermal deformation. They found that thermal deformation was a significant portion of the film thickness on the discharge side of the pump which caused variations in the pressure distribution.
Kim et al. [2012] and Bergada et al. [2008] experimentally measured the film thickness of a fixed valve plate type axial piston pump. Kim et al. [2012] achieved this by using a single proximity probe mounted on the side of the cylinder block in a 68 cc/rev pump at speeds between 1500-2500 RPM and pressures between 25-35MPa,. In this approach as the cylinder block rotated, the sensor detected the film thickness as a function angular position. They found that as the speed increased the minimum film thickness also increased. Also, the maximum film thickness greatly increased with an increase in discharge pressure. Bergada et al. [2008] achieved this through the use of three proximity probes mounted directly into the valve plate of a 24.1cc/rev pump at a speed of 1440 RPM and pressures between 2.5-19.5 MPa. They also showed that with an increase in discharge pressure there was a decrease in film thickness. The resulting film thicknesses can be seen in Figure 1.3

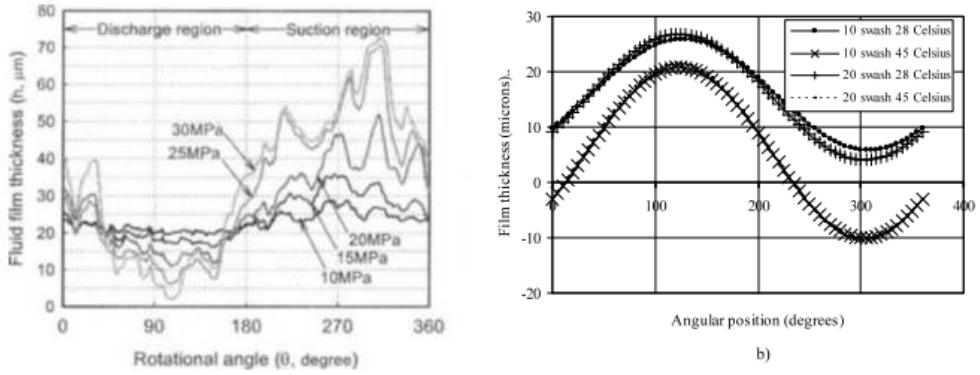

Figure 1.4: Film Measurements of valve plate/cylinder block interface a) [Broman 2001] b)[Kim 2012]

Latas and Stojek [2011], Chen et al. [2006], and Nishimura et al. [1995] have used spring & dashpot systems to describe the dynamic motion and vibrations seen between the various parts of an axial piston pump. Nishimura et al. [1995] developed the equations of motion to characterize the dynamics and vibrations observed in the pump housing during a typical axial piston pump operation. Chen et al. [2006] used a 14-DOF system to predict the vibrations seen in the outer shell of an axial piston pump. Latas and Stojek [2011] used a 13 DOF system seen in Figure 1.5 to predict the wear tracks that occurred as the piston shoes slid on the swash plate, as well as the vibrations observed in the pump housing and valve plate.

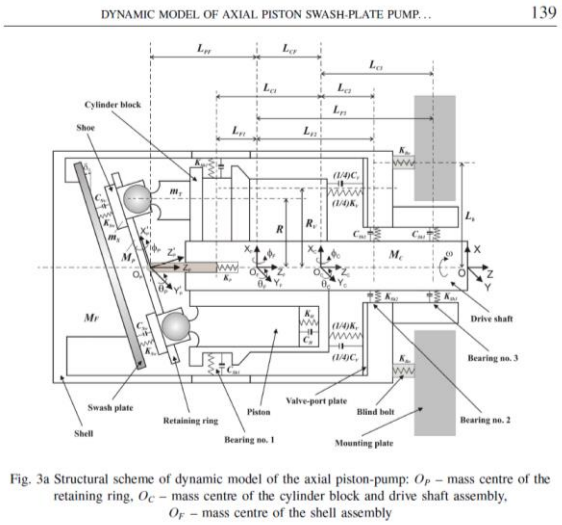

Fig. 3a Structural scheme of dynamic model of the axial piston-pump: O_P – mass centre of the retaining ring, O_C – mass centre of the cylinder block and drive shaft assembly, O_F – mass centre of the shell assembly

Figure 1.5: 13 DOF System to describe pump vibrations [Latas and Stojek 2011]

It is important to note that axial piston pumps either have a fixed or floating valve plate. In the floating valve plate axial piston pump, the valve plate is fixed in its rotation; however, it is free to move along the axial direction of the pump to develop a lubricating gap. The cylinder block is free to rotate but it is fixed in the axial direction. In the fixed plate axial piston pump, the valve plate is fixed in all directions. The cylinder block for a fixed valve plate is however, free to rotate and move axially along the pump to create a lubricating gap. Consequently, in a fixed valve plate axial piston pump the cylinder block moves to create a lubricating gap, whereas in a floating valve plate axial piston pump, the valve plate is the moving part which creates the lubricating gap. Whereas the aforementioned investigations have been performed with fixed valve plate axial piston pumps, this study has focused on how the performance of floating valve plate axial piston pump.

1.2 Surface Modifications

Thrust washers and surface modifications that have been extensively used in the automotive, aerospace and pump industries to increases the load carrying capacity and film thickness between bearing surfaces. Thrust washers are desirable when support for a thrust load is needed but the space requirement is limited. Thrust washers are able to support thrust loads by utilizing the geometric wedge effect to generate pressure in the lubricant. The resulting pressure separates the bearing surfaces and supports the applied load. Different surface geometries such as pockets, dimples, and groves are used to support load, generate appropriate film thickness and reduce friction and wear. The shape and design of the surface geometry is often determined through analytical modeling to optimize the load carrying capacity of the bearing while also providing sufficient lubricant film between the two surfaces.

Etsion et al. [1999] and Ryk [2002] presented an analytical and experimental study of laser textured mechanical seals as shown in Fig. 1.6. They developed a steady state hydrodynamic model and assumed that the contact interface remains fully flooded. The Reynolds boundary condition was used to account for lubricant cavitation. Their model indicated that the depth to diameter ratio was much more influential than the density of textured surface pores. They indicated that properly designed pores could significantly improve the hydrodynamic lubrication condition. Results showed that a very shallow dimple depth of 6μm with a diameter of 96μm at

an area coverage ratio (dimple area / land area) of 20% provided the best load support. The results showed a strong relation to the dimples' depth-to-diameter ratio.

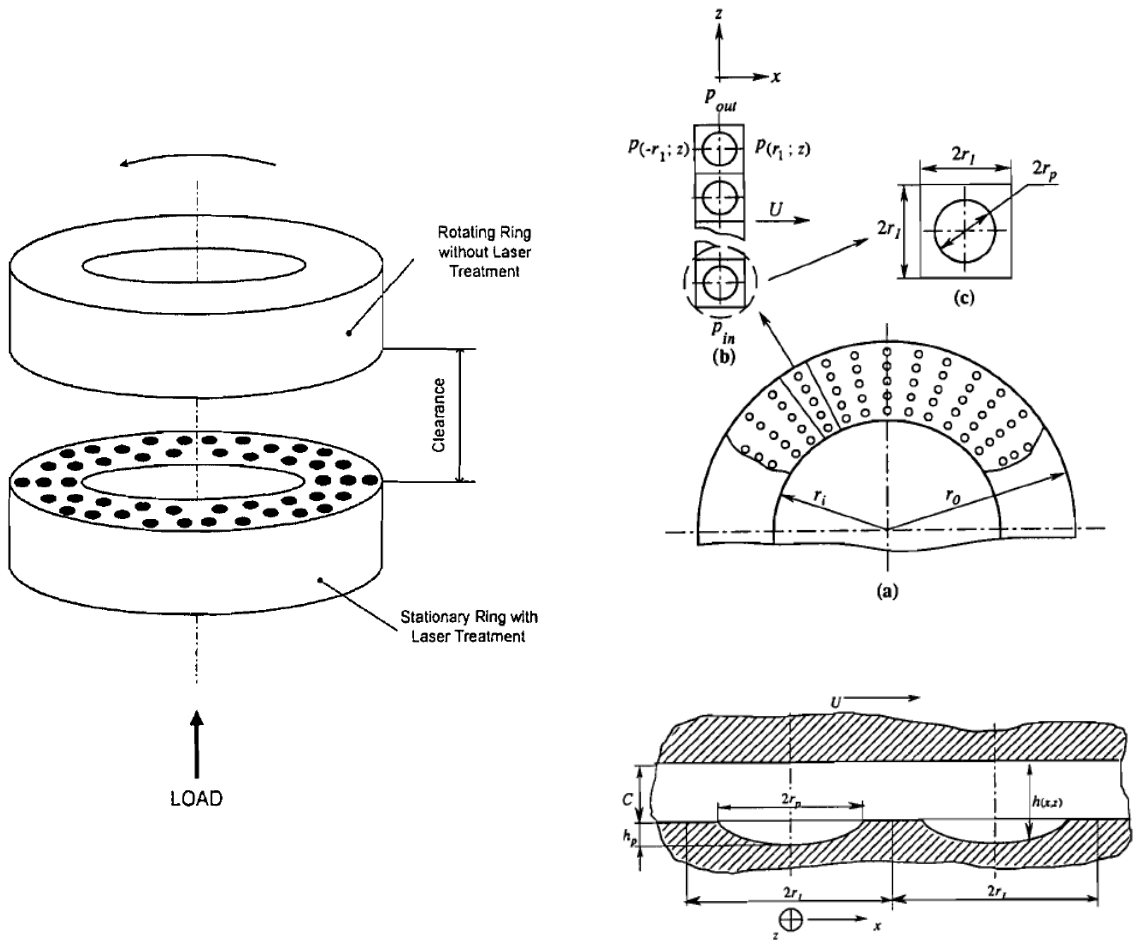

(a) Seal Model and Mode of Operation (b) Geometry of Pores

Figure 1.6: Laser Textured Mechanical Seals [Etsion et al. 1999]

Vaidya and Sadeghi [2008] developed an analytical model to predict the hydrodynamic pressure distribution and film thickness at the thrust interface of an orbiting scroll bearing with grooves and circular pockets. The pockets ranged from 7 mm to 9 mm in diameter and 50 to 80 μm in depth. The results show that the surface with pockets has a much significant improvement as compared to that of the grooves. Figure 1.6 depicts the effect of number of grooves/pockets on the load carrying capacity for different surface profiles. The load carrying capacity for pockets is much larger than that for grooves. Similarly, the surface with pockets causes a significant reduction in friction coefficient as that of the grooves as shown on Figure 1.7. The main reason is

that the pockets can cause a larger magnitude of pressure build up than the grooves when the velocity of the thrust surface is in both radial and tangential directions. Findings also showed that shallow, wide pockets provided the best load support and lowest friction.

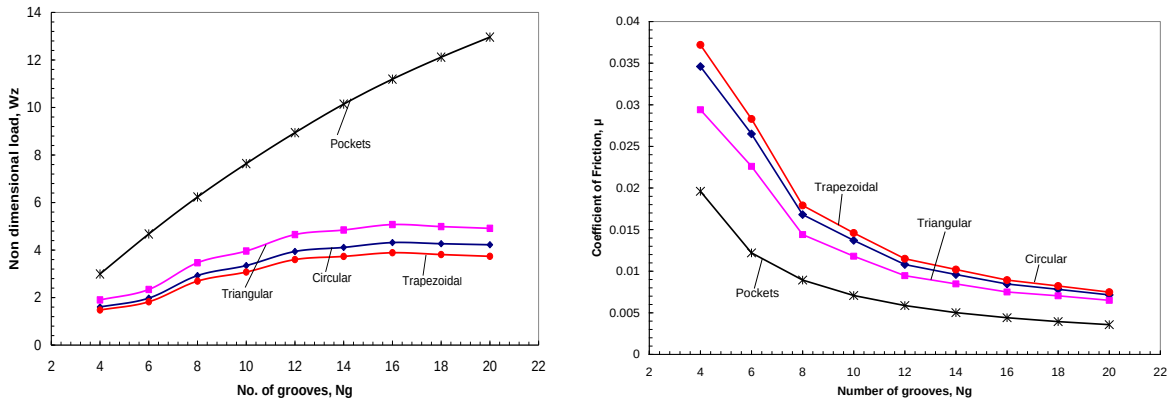

Figure 1.7: Effect of Number of Grooves/Pockets [Vaidya and Sadeghi 2008]

Many types of surface modifications have been added to axial piston pumps to improve performance. Kim et al[2003] investigated adding bearing pads to the valve plate surface as seen in Figure 1.8. They developed a test rig to measure the film thickness of the valve plate/cylinder block interface, and compare between a valve plate that has surface modifications and one that does not. They found that if the valve plate surface was modified to include bearing pads the minimum film thicknesses observed for the most extreme cases increased from 3μm to 10μm.

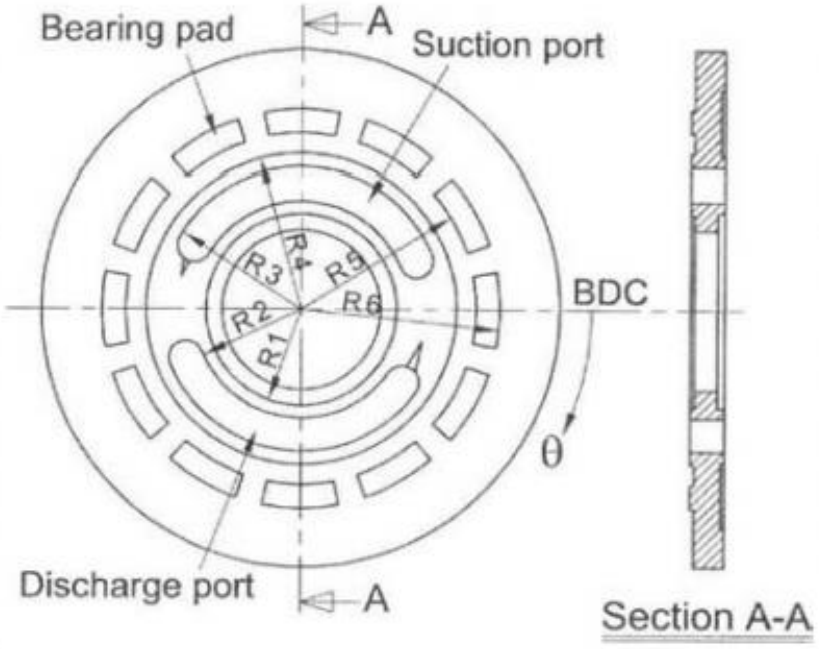

Figure 1.8: Valve Plate design with bearing pads[Vaidya and Sadeghi 2008]

Chacon et al. [2014] developed a numerical model to investigate the effects of adding a wavy surface texture to the valve plate. 10-30 waves of an amplitude between 1-4 µm, were added to the surface of the valve plate in the circumferential direction. Figure 1.9 illustrates the resulting pressure profiles and film thickness calculated for the valve plate. An overall increase in the fluid film was observed, as well as pressure spikes due to the geometry wedge effect from the wave texture. Additionally it was found that applying a sinusoidal wave of ±2 µm amplitude, frequency of 9 waves on the cylinder block surface predicts up to 35% reduction in total energy dissipation due to an increase in leakage flow at low pressure and low speed.

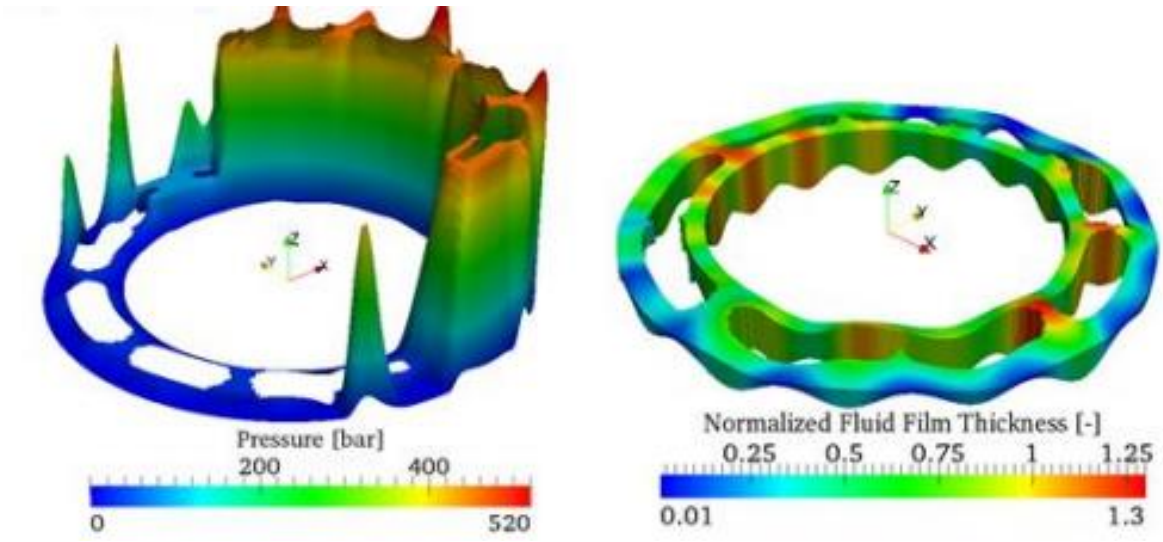

Figure 1.9: Wavy Valve Plate Pressures and Film thickness [Chacon 20014]

1.3 Lubricant Flow Visualization

Investigators have used visualization techniques such as particle image velocimetry (PIV) to measure the flow of lubricant in shear drive flow and compare with analytical models. Taneda [1979] provided measured the streamlines of low Reynolds number flows, including flows around bodies placed in a uniform flow, flows past a fence, flows past a wall pocket etc as shown in Fig. 1.9. Taneda determined that the time taken for the steady flow to be established is negligible and the streamline pattern remains unaltered even though the direction of flow is reversed.

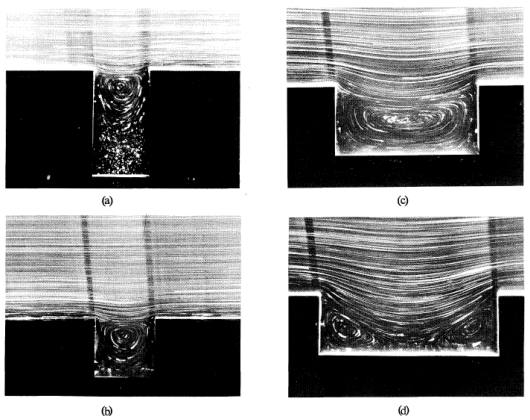

(a) Depth/Width=2, (b) D/W=1, (c) D/W=0.5, (d) D/W=1/3

Figure 1.10: Streamline Patterns of the Flow Past a Cavity [Taneda 1979]

O'Hern et al. [1994] introduced particle image velocimetry (PIV) and laser Doppler velocimetry (LDV) to investigate pressure driven flow in a large square pocket. Well characterized separated recirculating flow was observed inside of the pocket. The Reynolds number for their experiments ranged from 100 to 900. LDV is a standard technique for measuring point velocities. PIV uses image correlation to determine full-field velocity maps. The results between LDV and PIV were compared and showed good agreement between in most of the pocket area.

Wang et al. also set out to measure lubricant flow in micro pockets, and micro channels. Micro particle image velocimetry (μPIV) was utilized to measure streamline velocities in micro channels. Images captured during operation were correlated and flow velocity vectors were calculated. A large recirculation vortex was observed inhibiting lubricant flow out of the channel. Wang [2011, 2012] also used μPIV to study the flow in cylindrical dimples to evaluate their usefulness as lubricant reservoirs under starved conditions. Figure 1.11 depicts the flow in a single dimple. Figure 1.11 illustrated that there is actually reverse flow within the dimple while the leading edge begins to empty. It was demonstrated that dimples significantly extend the duration of hydrodynamic lubrication compared to an unmodified, flat specimen.

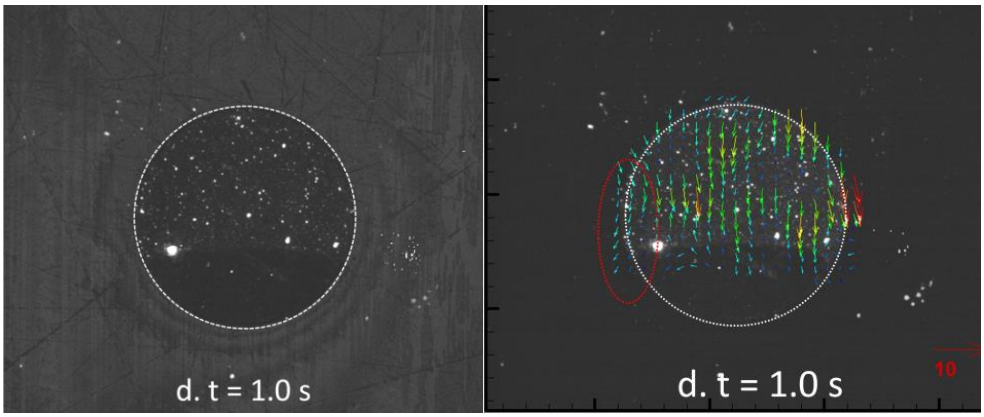

Figure 1.11: Streamline Patterns of the Flow Past a Cavity [Taneda 1979]

1.4 Thermal Effects on Lubricant Development

The effects of temperature is of significant importance when determining lubricant film thickness and pressures in a tribological interface. This is mainly due to exponential effect of temperature on lubricant viscosity. Cross et al. [2015] and Yu and Sadeghi [2002] have

investigated thermal effects of lubricant on cavitation in thrust washer bearings. Cross et al. [2015] experimentally measured the lubricant temperatures using a thermochromic material and illustrated a temperature drop in cavitated areas. Figure 1.12 illustrates how the cavitated area yielded a 10% decrease in temperature due to the fact that the air in the cavitated region conducts heat poorly.

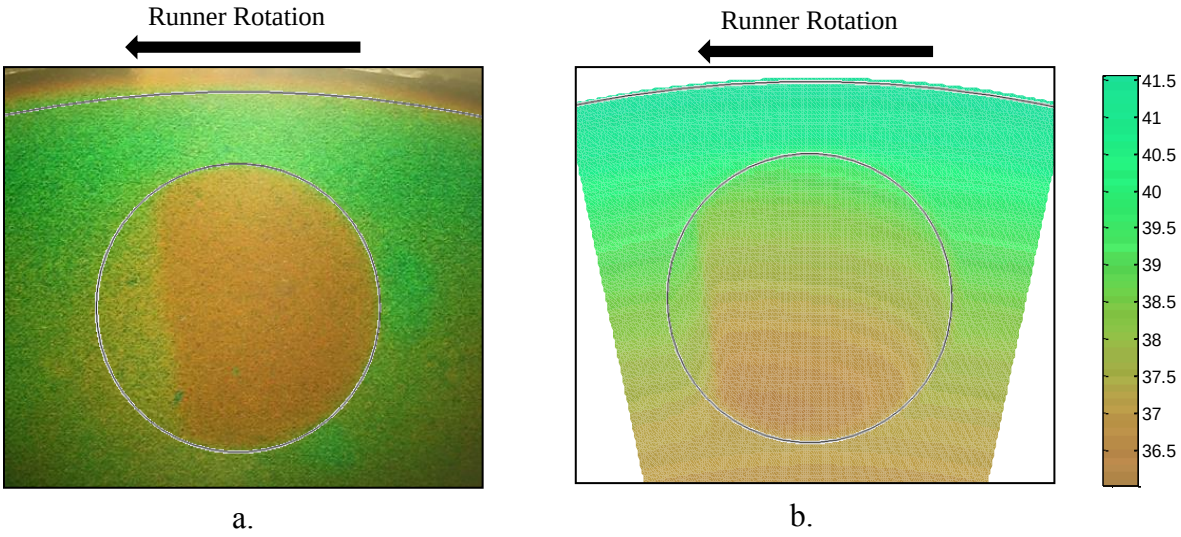

Figure 1.12 Comparison between Experimental and Simulated Temperature Profiles in a Pocket Thrust Washer Experimental (a), Simulated (b).[Cross 2012]

Boncompain [1986] similarly demonstrated that for the cavitated regions in journal bearings it was valid to assume the thermal properties of air. Using the thermal properties of air, it was illustrated that the surfaces around the cavitated regions decreased in temperature. Yu and Sadeghi [2002] developed a numerical model for thrust washers which indicated that the thermal effects not only reduce the load carrying capacity of the thrust washers and frictional torque but also increase the flow rate significantly due to the lubricant viscosity reduction. In addition, Bergada et al. [2011] experimentally explored the effects of temperature on the film thickness between a fixed valve plate and cylinder bloc. They showed that higher operating lubricant temperatures yielded a decrease in film thickness, putting the valve plate at an increased risk of wear and failure.

1.5 Reynolds Equation

The Reynolds and film thickness equations were simultaneously solved to determine the lubricating pressures between the floating valve plate and cylinder block. Equation 1.1 illustrates a 2D Cartesian coordinate Reynolds equation. The physical meaning of each term is also shown. The details of the Navier-Stokes equation and the Reynolds equation can be found in Hamrock et al. [2004].

$$\underbrace{\frac{\partial}{\partial x}\left(\frac{\rho h^3}{12\eta}\frac{\partial p}{\partial x}\right)}_{\text{Poiseille}} = \underbrace{\frac{\partial}{\partial x}\left[\frac{\rho h(u_a+u_b)}{2}\right]}_{\text{Couette}} + \underbrace{\rho\left(\omega_a-\omega_b-u_a\frac{\partial h}{\partial x}\right)}_{\text{Squeeze}} + \underbrace{h\frac{\partial \rho}{\partial t}}_{\text{Local Expansion}} \qquad (1.1)$$

$$\underbrace{\frac{h(u_a+u_b)}{2}\frac{\partial \rho}{\partial x}}_{\text{Density Wedge}} \quad \underbrace{\frac{\rho h}{2}\frac{\partial}{\partial x}(u_a+u_b)}_{\text{Stretch}} \quad \underbrace{\frac{\rho(u_a+u_b)}{2}\frac{\partial h}{\partial x}}_{\text{Physical Wedge}}$$

The left hand side of this equation is the Poiseuille term. The Poiseuille term describes the flow rates due to the pressure observed in the fluid. The pressure accelerates or impedes the flow to ensure mass is conserved. The first term on the right hand side is related to the bearing surface velocities and is the Couette term. This term can be divided into three different components, including density wedge ($\frac{h(u_a+u_b)}{2}\frac{\partial \rho}{\partial x}$), stretch ($\frac{\rho h}{2}\frac{\partial}{\partial x}(u_a+u_b)$), and physical wedge ($\frac{\rho(u_a+u_b)}{2}\frac{\partial h}{\partial x}$). The flow rate due to squeeze motion and the net flow rate due to local expansion are also described in the Reynolds equation. The two most common mechanisms for generating pressure in a bearing application are due to the physical wedge, and squeeze terms.

1.5.1 Physical Wedge

Figure 1.12 shows the lubricant between two non-parallel plates with the outlet smaller than the inlet. When the top moving plate drives lubricant through the channel, the flow rate at the outlet has to be larger than that at the inlet to satisfy the continuity of fluid flow for an incompressible fluid. Therefore, the pressure will increase due to physical wedge mechanism.

This hydrodynamic pressure provides thrust which balances the applied load and separates the surfaces. All of hydrodynamic lubrication is based on generating pressure due to the film geometry or physical wedge.

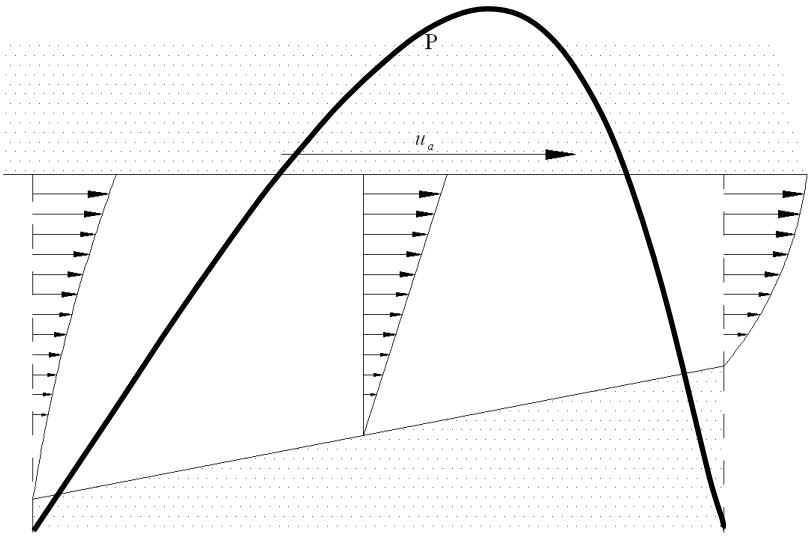

Figure 1.13: Physical Wedge

1.5.2 Squeeze Term

Hydrodynamic pressure can be generated by two surfaces approaching or distancing one anouthe, which is often referred to as squeeze motion. When the top surface approaches the bottom surface down, the lubricant film thickness decreases with time and pressure is developed between these two plates providing a valuable cushioning effect. Squeeze film dampers operate based on this principle and are used in many transient conditions. Figure 1.14 shows the mechanism of the squeeze motion and how pressure is generated.

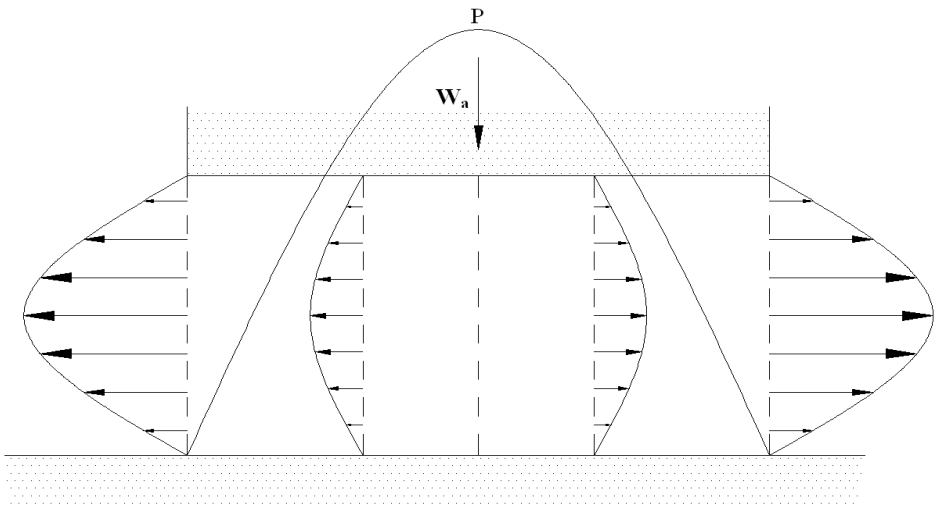

Figure 1.14: Squeeze Motion

1.6 Scope of Thesis

The scope of thesis is to investigate the performance of a floating valve plate in an axial piston pump both analytically and experimentally. Dynamic studies of the floating valve plate have led to a better understanding of how the lubricant film is developed between the valve plate and cylinder block. Pocketed thrust washers are also investigated as a potential mitigation technique to reduce wear of the valve plate by providing additional lubricant between the bearing surfaces.

Chapter 2 presents the study of the motion of the floating valve plate at various operating conditions. The motion is measured through the use of three non-contact proximity probes. The film thickness between the valve plate and cylinder block was also measured and used in a lubrication model to calculate the pressures that occur inside of the lubricating gap. Chapter 3 presents the results of a dynamic model to predict the valve plate motion and film thickness. Dynamic equations were developed to describe valve plate motion with the appropriate stiffness and damping coefficients for the system. The stiffness and damping coefficients were found using both the logarithmic decrement method and a parametric study. The dynamic model was then paired with a Reynolds lubrication model to simultaneously solve for the film thickness and lubricant pressure between the valve plate and cylinder block. Chapter 4 investigates the lubricant flow inside of a pocketed thrust washer. μPIV was implemented to measure the 2D

velocity fields inside of the bearing pocket. A numerical model was also developed to calculate the 3D velocity fields of the lubricant. Through an interpolation method the z-locations of the measured velocities were determined and used to create 3D velocity fields from experimental data. Chapter 5 presents the results of a study investigating the effects of surface modifications on lubricant temperatures and floating valve plate motion. The thermal Reynolds equation augmented with the JFO boundary condition and the energy equation were simultaneously solved to determine the pressure, cavitation regions and temperature of the lubricant at the valve plate cylinder block interface. 4 and 8-pocket designs were then added as surface modifications to the floating valve plate in the dynamic lubrication model. The addition of surface modifications on the valve plate yielded increased film thicknesses when compared to the standard design. In Chapter 6, a summary of the major achievements of this work is described. Recommendations for future work are also addressed

2. EXPERIMENTAL AND ANALYTICAL INVESTIGATION OF FLOATING VALVE PLATE MOTION IN AN AXIAL PISTON PUMP

2.1 Introduction

The purpose of this investigation was to experimentally measure the motion of the floating valve plate in an axial piston pump under various operating conditions and to develop a model to determine how the floating valve plate motion affected the lubricating pressures between the valve plate and cylinder block. In order to achieve the objectives, a hydraulic circuit was designed and developed to incorporate and operate a floating valve plate axial piston pump. The hydraulic circuit integrating the axial piston pump (axial piston pump apparatus, APPA) consists of a series of valves, pressure sensors, a charge pump, flow meters, temperature sensors, heat exchanger and proximity probes. The floating valve plate axial piston pump housing was modified to incorporate three proximity probes to measure the valve plate position and motion relative to the cylinder block, thus allowing for determination of the film thickness within this contact. The results illustrate that as the pump starts up the valve plate experiences vibrations and begins to lift relative to the cylinder block. Then as the pump reaches steady state operation the valve plate achieves a fixed position and tilt. The results also demonstrate that under steady state operation, the valve plate vibrates and that this vibration correlates well with the speed and the number of pistons in the pump. The measured film thickness results were then used in a lubrication model to determine the pressures generated between the floating valve plate and the cylinder block. The analytical results highlight how the motion of the valve plate directly correlates to the pressure pulsations seen in the lubricating gap.

2.2 Axial Piston Pump Apparatus

A test apparatus was designed and developed to incorporate an axial piston pump with a floating valve plate. Figure 2.1 illustrates the hydraulic circuit that was designed to measure and control the flows and pressures created at the inlet, outlet, and case lines of the pump. The hydraulic circuit is based on a general design for steady state testing of axial piston pumps commonly used in industry. The axial piston pump used in this investigation required a charge

pressure; therefore a charge pump was added in series to provide the initial pressure to the axial pump.

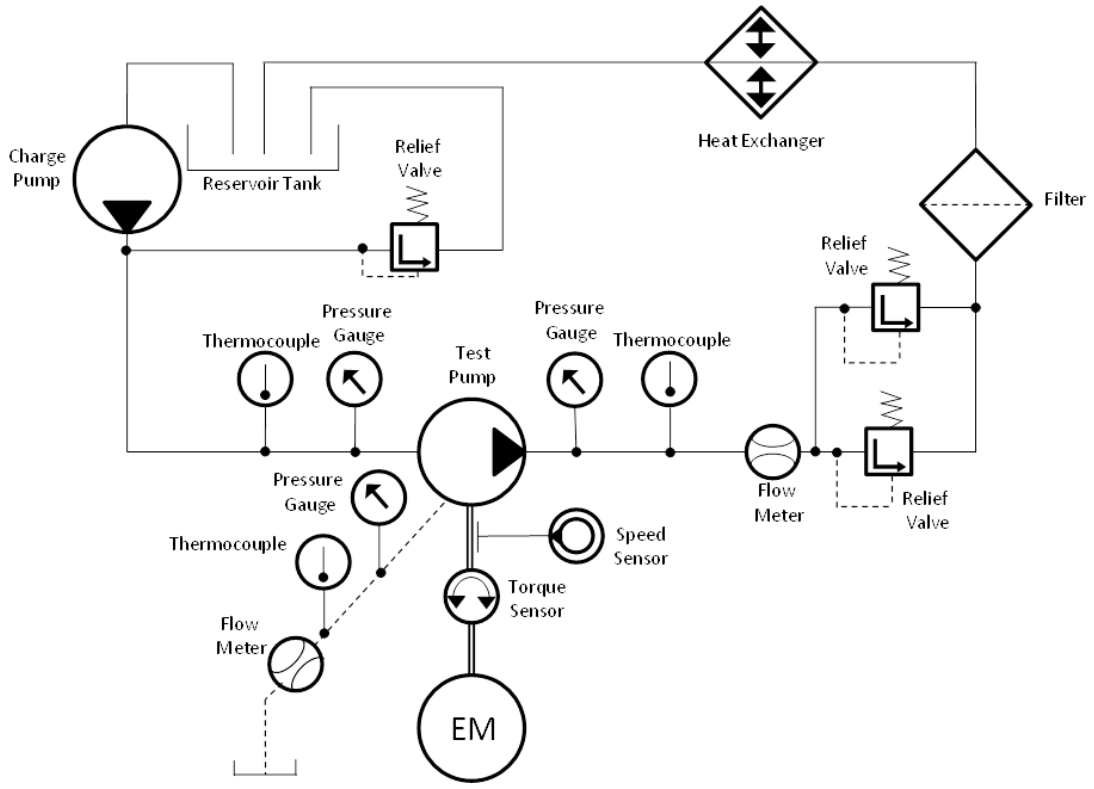

Figure 2.1: Hydraulic circuit of Axial Piston Pump Apparatus

Figure 2.2 illustrates the axial piston pump apparatus (APPA) designed and developed for this investigation. The APPA was instrumented with flow meters accurate to within 0.5% of full scale, pressure transducers accurate to within 0.25% of full scale, and thermocouples to monitor the APPA conditions and ensure that the pump was operating within the desired steady state conditions. The axial piston pump was coupled to a variable speed 15 hp electric motor using a rigid coupling. The motor speed was adjusted between 600 and1800 RPMs using a Baldor controller. K type probe thermocouples were used to monitor the temperature of oil flow, to ensure that the viscosity of the oil is within the desired specific operating conditions. Pressure transducers along the inlet, outlet and case lines were used to monitor and help control the oil pressures to the desired operating conditions. Also turbine type flow meters were mounted along the case drain and outlet lines of the pump to monitor the steady state oil flow. Sensors were placed in the circuit according to ISO 4409. Two relief valves in parallel were used to control

the outlet pressure between 800 psi(5.51Mpa) and 1200 psi(11.02Mpa) . In order to keep the oil at a constant operating temperature of 35°C, a heat exchanger was incorporated at the inlet to the oil reservoir. A 3µm filter was mounted just before the oil flows into the heat exchanger to remove debris contaminants from the oil.

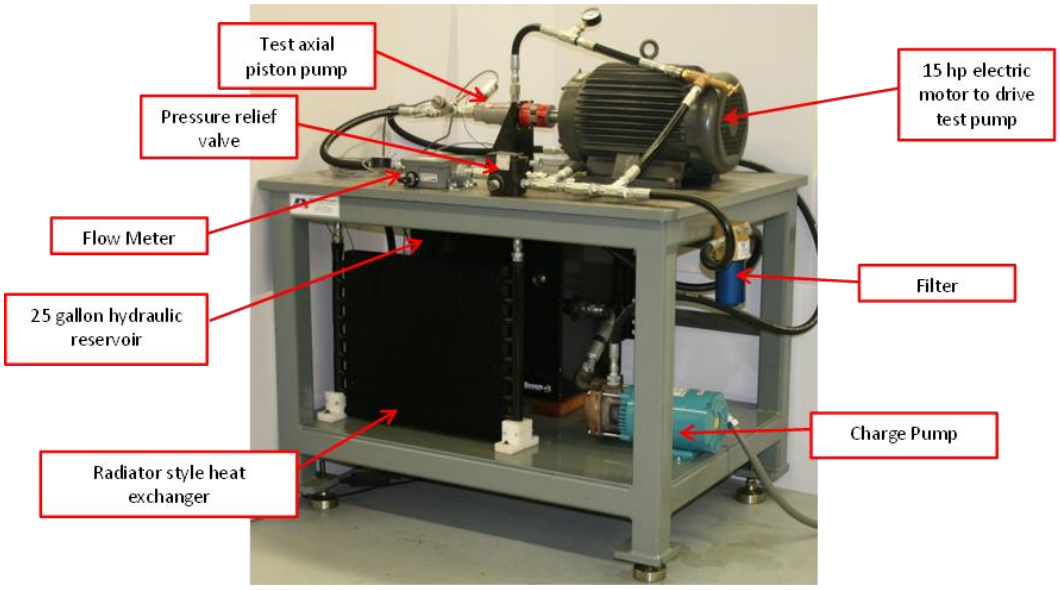

Figure 2.2: Constructed Axial Piston Pump Apparatus

The lubricating gap between the floating valve plate and cylinder block was measured through the use of 3 high precision non-contacting proximity probes, which have an accuracy of ±1µm of the measured data. It is important to note that due to the small size and geometry of the axial piston pump, only three proximity probes could be accommodated without interfering with the fluid flow in and out of the valve plate and operation of the pump. To determine the placement of the probes the valve plate geometry was considered so as to not interfere with the fluid flow. Figures 2.3 and 2.4 depict the front and back view of the valve plate. Figure 2.3 illustrates that the valve plate has a suction and a discharge port where the fluid flows in and out of the pump. Located at both the top and bottom dead centers are two auxiliary balance pistons that provide a reservoir of fluid such that when the piston is transitioning from the discharge to suction, the risk of a large drop in lubricating pressure is reduced.

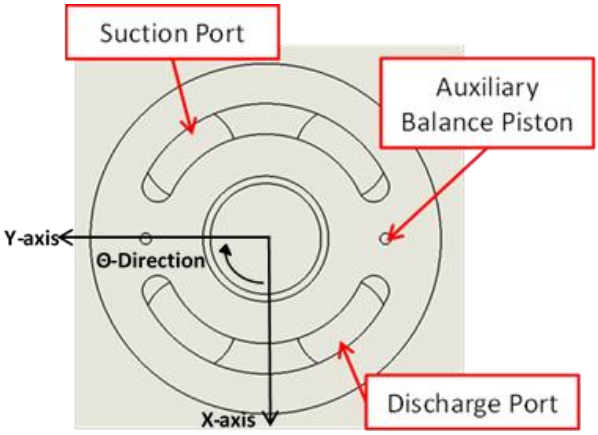

Figure 2.3: Valve Plate Geometry (front view)

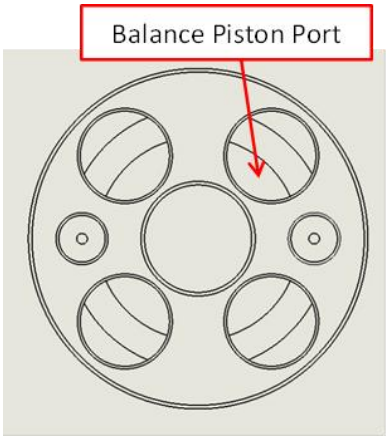

Figure 2.4: Valve Plate Geometry (back view)

Figure 2.4 shows that on the backside of the valve plate there are four ports for the main balance pistons which connect the valve plate to the housing and prevent the valve plate from rotating with the cylinder block while still allowing it to move in the axial direction of the pump to create the lubricating gap (film thickness). The proximity probes, as shown in Figure 2.5, were mounted in the pump housing and located near the top and bottom dead center so as to not interfere with the suction and discharge ports. The exact locations of the proximity probes are listed below.

Proximity Probe 1: X1 = 6.61 mm Y1 = 19.8 mm

Proximity Probe 2: X2 = 6.61 mm Y2 = -19.8 mm

Proximity Probe 3: X3 = -6.61mm Y3 = 19.8 mm

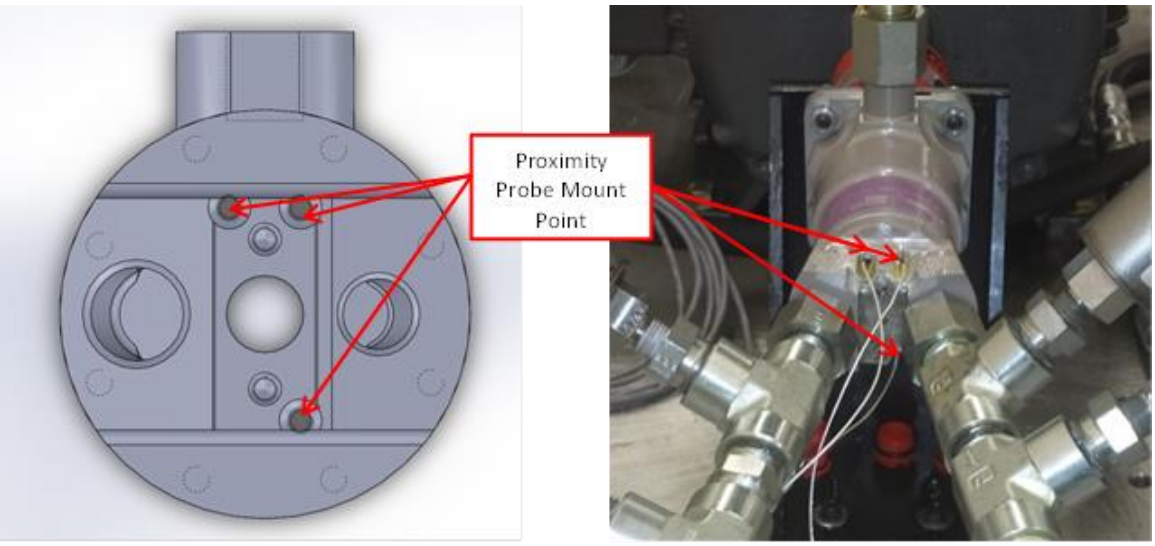

Figure 2.5: Proximity probe mount points

Figure 2.6 illustrates that while the pump is not operational, the valve plate and cylinder block are in contact with one another. This is due to the fact that during pump assembly the valve plate and cylinder block are pressed towards one another by springs. The springs are located on the top of the housing and push down on the valve plate, this helps to resist abrupt changes in the valve plate motion which could cause damage to the valve plate and ensures contact between the valve plate and cylinder block while not in operation. In the floating valve plate axial piston pump used in this investigation, the cylinder block cannot move in the axial direction because it is connected to the motor shaft by a pin joint which prevents any axial motions. The valve plate cannot rotate, however because it is a floating valve plate it is allowed to move axially along the pump. Therefore the proximity probes measure the distance from the housing to the valve plate. It is the change in the distance between the initial distance from the housing to the valve plate and the distance from the housing to the valve plate measured during operation is the film thickness that separates the valve plate and cylinder block.

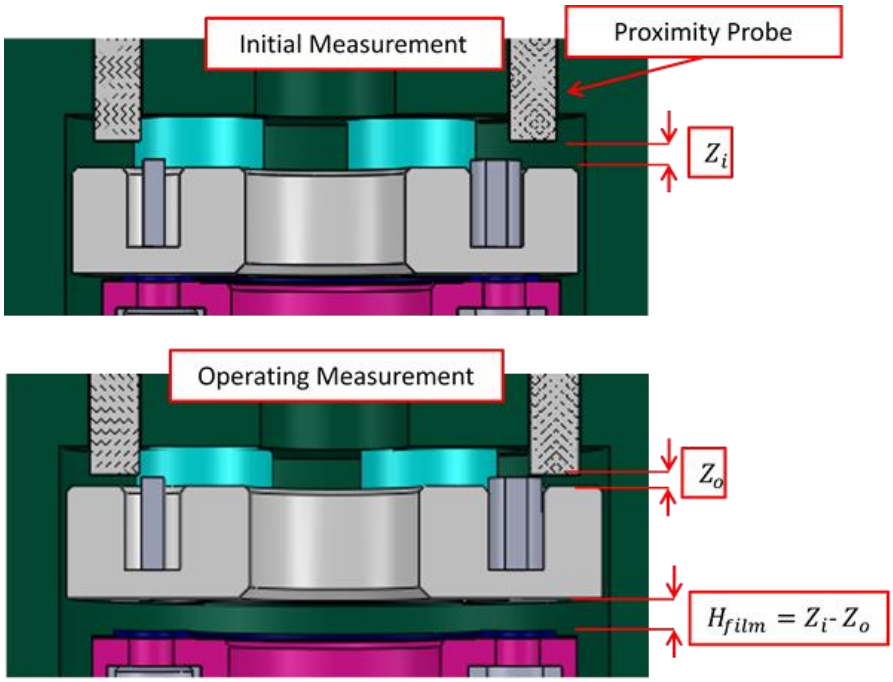

Figure 2.6: Method of film measurement

Figure 2.7 illustrates a sectioned view of the pump with the proximity probes mounted in the housing. Once the measurement system was completely developed and the test rig constructed, experiments were performed at a wide range of speeds and discharge pressures to determine how they affected motion of the valve plate. Table 1 contains the test parameters used in this investigation.

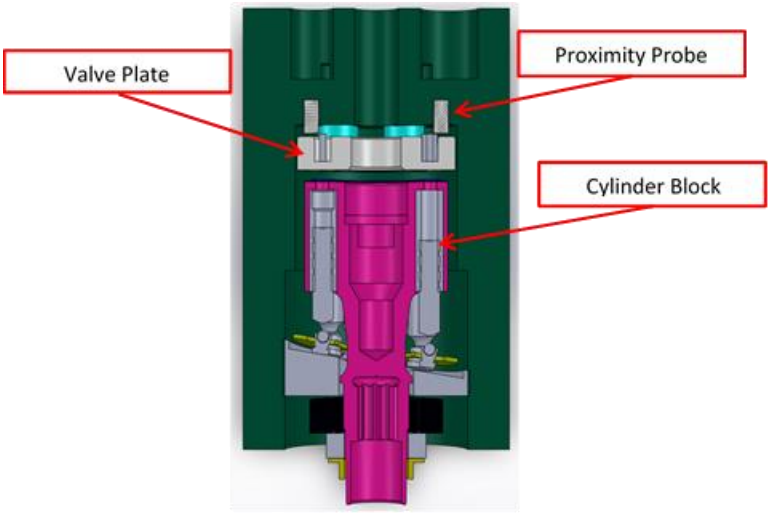

Figure 2.7: Section view of pump with proximity probes

Table 2.1 Test Parameters for APPA

Test Parameters	
Pump size(cc/rev)	6
Speed (RPM)	600,900,1200,1500,1800
Discharge Pressure (psi)	800,1000,1200
Discharge Pressure (MPa)	5.51,6.89,8.27
Oil used	0W-20
Oil Temp	35° ± 2° C
Oil Viscosity (Pa·s)	0.043

2.3 Experimental Results

Figure 2.8 depicts the displacements between the floating valve plate and the housing measured using the three precision proximity probes during a typical test at 1000psi(6.89MPa) and 1200 RPM. The distance from the proximity probes is measured as negative as made evident in Figure 2.8. A close examination of the results indicates that there are fluctuations in the measured signal. In order to determine the origins of these fluctuations, a Fast Fourier Transform analysis was performed on the data to determine the frequencies that make up the signal.

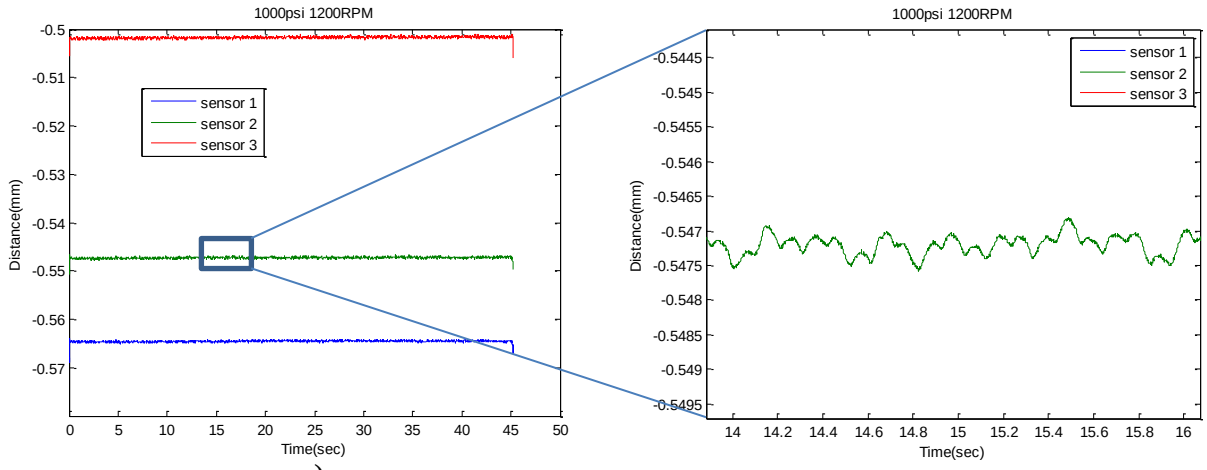

a) b)

Figure 2.8: Experimental Data a) Raw data taken from experiments at 1000psi and 1200 RPM b) Zoomed in view of data illustrating fluctuations seen in signal

Figure 2.9 shows the FFT analysis performed on the data while the pump was operating at a pressure of 1000 psi(6.89MPa) and speeds of both 600 and 1200 RPM. Figure 2.9 demonstrates that the observed signal fluctuations can be traced back directly to the operating conditions of the pump and are not a result of electrical or ambient noise. For the case of the pump operating at 600 RPM or a frequency of 10Hz, the FFT shows the largest frequency occurring at 10 Hz, implying that the oscillations in the displacement frequencies is directly related to the speed of operation. It is also important to note that because there are nine pistons there should be another frequency spike at nine times the operating frequency. This is because for one revolution, all nine pistons should pass a given point on the valve plate resulting in a vibration at nine times the frequency of the operating condition. The FFT analysis supports this ascertain showing another frequency spike at 90Hz. The observed trends are typical for all operating speeds of the pump. For the case of the pump operating at 1200 RPM or 20 Hz, there is a spike at 20 Hz as well as at 180Hz. Therefore, as described earlier the FFT demonstrates that the vibrations seen in the displacement results are a direct consequence of the discrete number of pistons and the forces they apply on the valve plate.

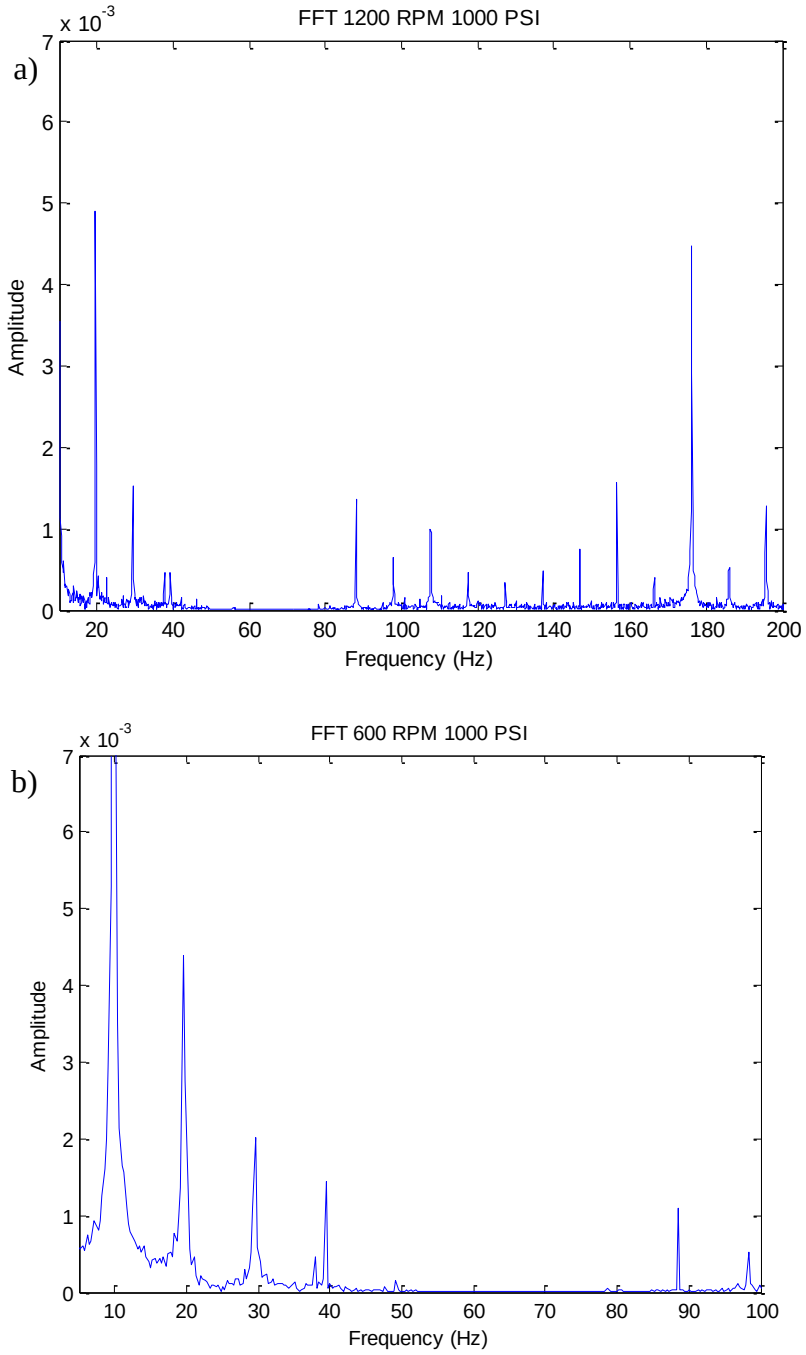

Figure 2.9: Fourier analysis of raw data a) FFT analysis of data at 1000psi and 1200 RPM b) FFT analysis of data at 1000psi and 600 RPM

Using the displacements at three distinct points a complete film thickness profile for the valve plate can be developed which describes the film thickness across the entire lubricating gap. This is achieved by creating a plane that intersects the three measured points. The plane then

represents the position of the valve plate relative to the cylinder block. The ground or origin of the plane representing the film thickness is located at the center of the top of the cylinder block. Figure 2.10 shows a table of height profiles generated for the operating conditions of 800 psi(5.51MPa) to1200 psi(11.02MPa) and 600 to1200 RPM.

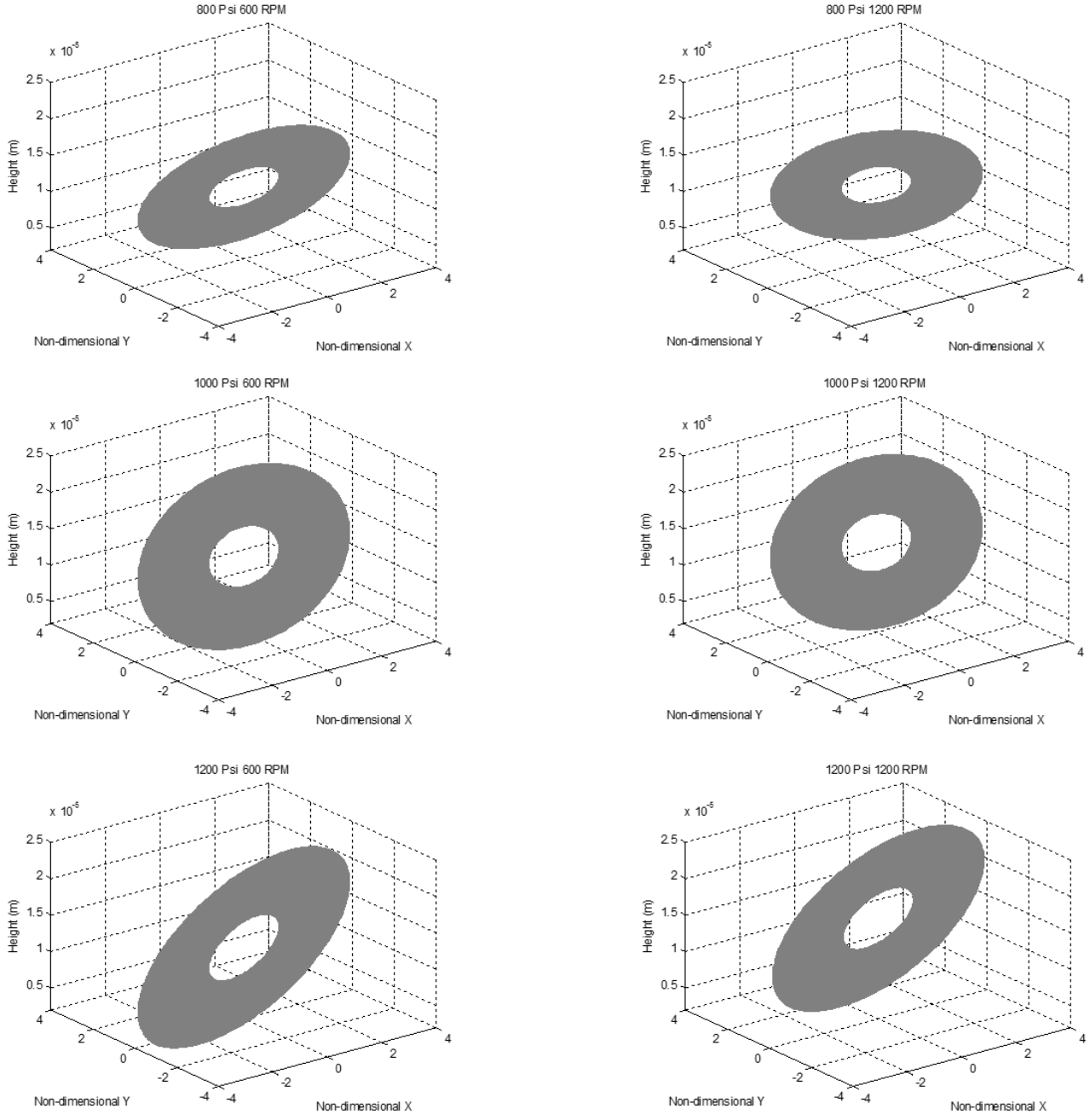

Figure 2.10: Measured film thicknesses for different operating conditions

Using the planes that were generated from the measured data the angles of operation and minimum film thickness values were obtained to characterize the changes that occurred across the operating conditions of the piston pump. The minimum film thickness for all conditions tested during steady state operation ranged between 3 to 10µm, specific comparisons between the operating conditions and the minimum film thickness are illustrated in Figure 2.11. Kim et al. [2012] found that the minimum thickness for a fixed valve plate pump to be between 10 to 15 µm. Thus, on the average the pump used in this investigation yielded smaller minimum film thicknesses. It is to be noted that Kim et al. [2012] had incorporated bearing pads in their pump which enhanced the lubrication condition and thus the lubricant film thickness. The pump in the current study did not have such bearing pads.

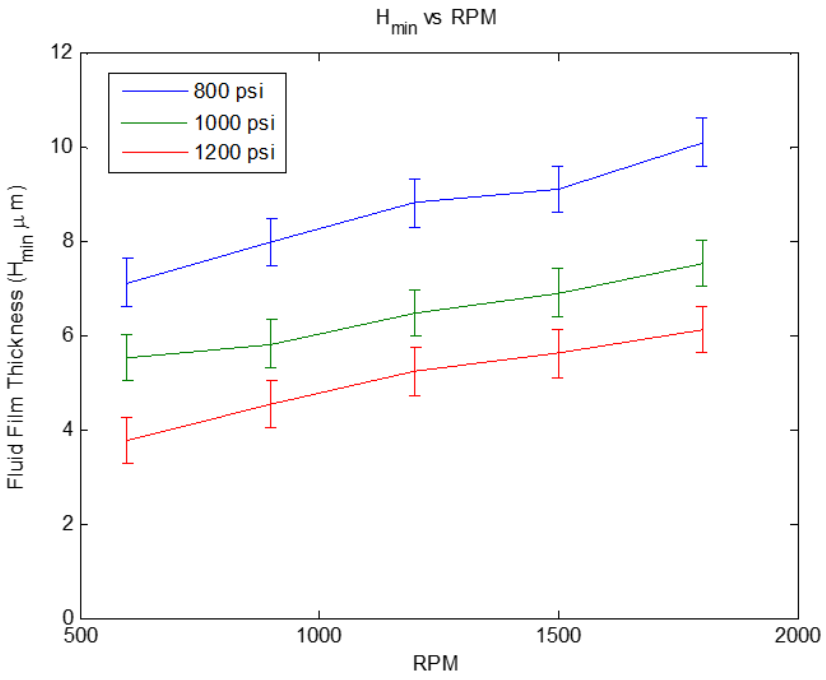

Figure 2.11: Minimum film thickness vs RPM and pressure

The location of minimum film thickness is also important because it is at this point that there is a possibility of a large spike in lubricating pressure. This is due to the fact that at the point of minimum film thickness there is a geometric wedge that according to the Reynolds equation is the pressure generating mechanism. For all of the experiments performed, the minimum film thickness occurred around the middle of the suction side of the valve plate, or at

an angular location between 170 to 190°. When comparing these results to a fixed valve plate design, Kim et al. [2012] found that the minimum film thickness location to be in the middle of the discharge side of the valve plate or at an angular location of 70 to 90°. Kim et al. [2012] showed that what caused this location of minimum film thickness were the fluid forces applied by the piston on the cylinder block. They showed that the viscous friction forces applied by the pistons on the cylinder block is sufficient enough to move the cylinder block as close to the valve plate as possible on the discharge side of the pump. In the current investigation, because of the use of a floating valve plate and a fixed cylinder block, the viscous forces applied by the pistons on the cylinder block do not affect the film thickness. Instead the high discharge pressures cause the valve plate to separate from the cylinder block commencing the valve plate to be angled toward the suction side of the pump, which result in the location of the minimum film thickness to be on the suction side of the pump. In this investigation, the minimum film thickness consistently occurred on the suction side of the valve plate for all operating conditions.

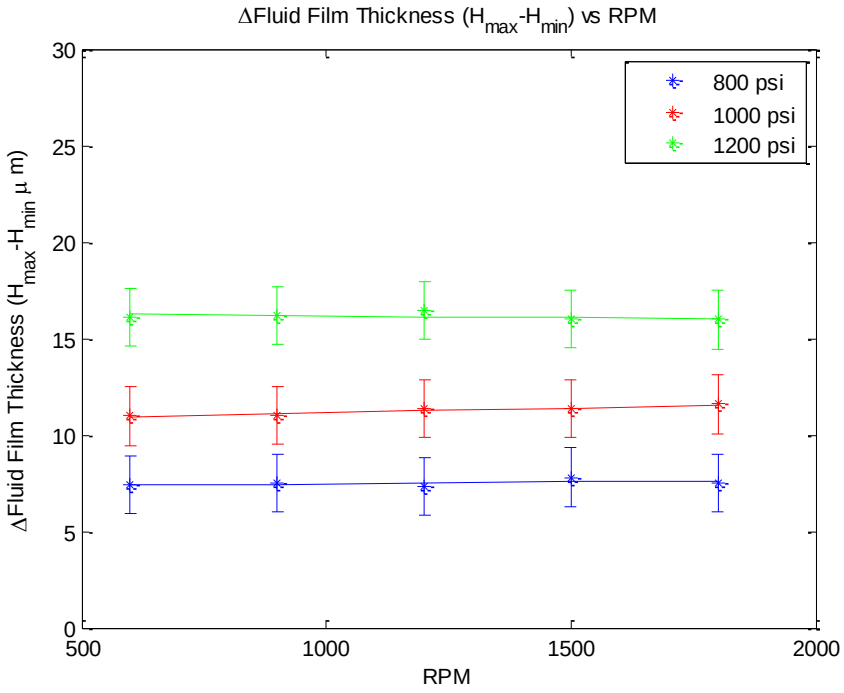

Figure 2.12: Change in film thickness vs RPM and pressure

Figures 2.11 and 2.12 provide further demonstrate how operating conditions affect the film thickness profile. Film thickness parameters, such as the magnitude of the minimum film

thickness and the difference between the maximum and minimum film thicknesses, are compared against operating parameters such as speed and discharge pressure. In this investigation, at each operating condition 10 tests were performed, Figures 11 and 12 show the averages of the results obtained, with the according error associated with the proximity probes.

The results shown in Figure 2.11 illustrate that with a small increase in discharge pressure, the minimum film thickness greatly decreases. For the case of the pump operating at 600 RPM and 800 psi(5.51MPa) the minimum film thickness is 7.2μm, whereas at 600 RPM and 1200 psi(11.02MPa), the minimum film thickness is 3.8μm. This demonstrates that for a 50% increase in pressure the minimum film thickness also reduced by 50%. While analyzing the effects of the speed on minimum film thickness, it was found that they are much less significant than that of pressure. At 1000 psi(6.89MPa) and 600 RPM the film thickness is 5.4 μm, but when the speed is increased to 1800 RPM the film thickness increases to 7.3 μm, which is a 35% increase. Thus for a large increase speed only a slight increase in minimum film thickness is observed. The trends found in this investigation are similar to those observed by Kim et al. [2012]; the sharp decrease in minimum film thickness due to an increase in discharge pressure was a common trend throughout their testing. They also found that speed has a small influence on minimum film thickness. However, similar to our investigation and as expected, they also observed an increase in minimum film thickness due to an increase in speed.

The purpose of calculating the difference between the minimum and maximum film thickness is to illustrate how the angle of operation of the valve plate is affected by the operating conditions. When comparing the different discharge pressures to the height difference, a steady increase in height difference was observed as the discharge pressure was increased. For the case of 800 psi(5.51MPa) and 1200 RPM the difference in height is 6.5 μm, whereas at 1200 psi(8.27MPa) and at the same speed the height difference is 16.2 μm. In this case, by increasing the discharge pressure by 400 psi(2.75MPa) resulted in an increase of 9.7 μm in the height difference, which demonstrates that the effect of discharge pressure on the film thickness is significant.

Rotational speed has little effect on the height difference of the film thickness when compared to pressure. At 1000 psi(6.89MPa) and 600 RPM the change in film thickness is 10.9 μm. When the speed is increased to 1800 RPM the height difference becomes 11.5 μm. This increase of 0.6 μm is negligible and on the order of the error of the sensor thus the effects of

speed can be neglected. Kim et al. [2012] observed similar trends while comparing effects of operating conditions on height difference. In their experiments, similar to our investigation, they observed a small increase in height difference as the speed was increased. They also found a significant effect between the discharge pressure and height difference that as the pressure was increased there was a sharp increase in the height difference.

As was shown in Figures 2.11 and 2.12, the discharge pressure can greatly affect both the height difference and the minimum film thickness. The effects of speed were much less significant when compared to that of pressure. For both the minimum film thickness and the height difference there needed to be a large increase in speed to observe changes in the film thickness parameters.

2.4 Analytical Investigation

The experimental measured film thickness profiles were used as the input in a time dependent lubrication model to determine how the lubricant pressure changed as function of time. The time dependent Reynolds equation is:

$$\frac{\partial}{\partial \bar{r}}\left(\frac{\bar{r}\bar{h}^3}{12\bar{\eta}}\frac{\partial \bar{P}}{\partial \bar{r}}\right)+\frac{1}{\bar{r}}\frac{\partial}{\partial \theta}\left(\frac{\bar{h}^3}{12\bar{\eta}}\frac{\partial \bar{P}}{\partial \theta}\right)=\frac{\omega}{2}\frac{\partial \bar{h}}{\partial \theta}+\frac{\partial \bar{h}}{\partial t} \tag{2.1}$$

Equation 2.1 was discretized using the control volume finite difference approach and was numerically solved using the height profiles from the experimental results.

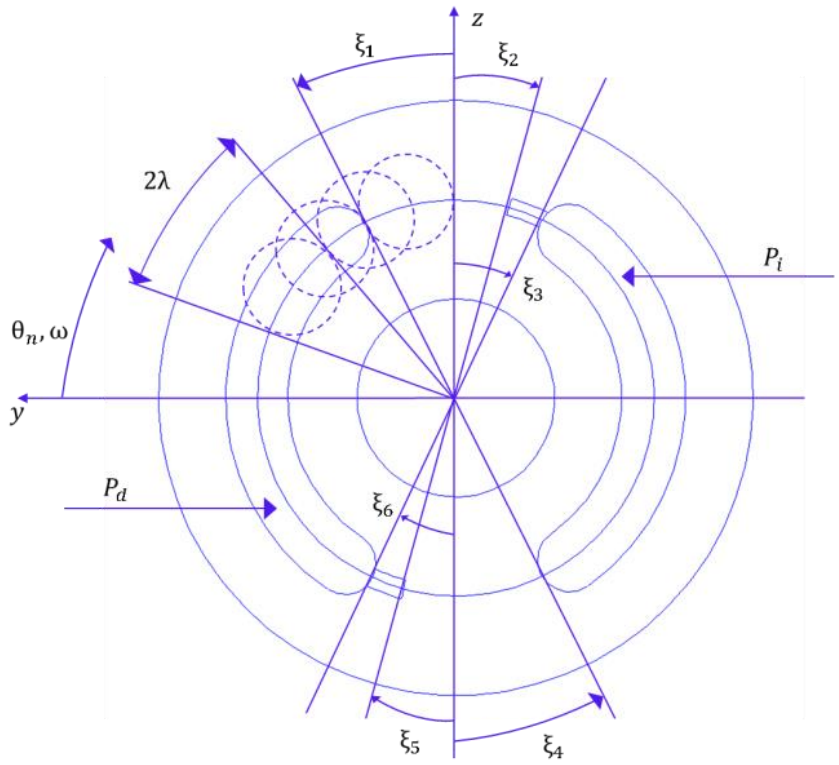

Figure 2.13: Valve plate geometry for calculating instantaneous piston pressure

The purpose of the lubrication model was to solve for the lubricating pressures around the different boundary conditions allowing for a complete understanding of the pressure that occurs between the valve plate and cylinder block. Appropriate pressure boundary conditions for this lubrication model include, suction and discharge pressures, instantaneous piston pressure, and case pressure. The inner and outer radii of the valve plate were fixed at the case pressure of 100 psi(0.689MPa). The suction and discharge boundary conditions are modeled as regions of fixed pressure with the same dimensions as the ports on the valve plate, and are set to the pressures of the operating conditions. To model the instantaneous piston pressure Zhang et al. [2008] developed a piecewise function to describe the piston pressure as a function of its angular position. Equation 2.2 and Figure 2.13 show a diagram of how the piston pressure boundary conditions are applied as well as the piecewise function used to describe the pressure as a function of its angular position.

$$Pn(\theta n) \approx \begin{cases} P_d & 0 \le \theta_n < \frac{\pi}{2} - \lambda - \xi_1 \\ P_d & \frac{\pi}{2} - \lambda - \xi_1 \le \theta_n < \frac{\pi}{2} - \lambda + \xi_2 \\ P_d - m\left(\theta_n - \frac{\pi}{2}\right) & \frac{\pi}{2} - \lambda + \xi_2 \le \theta_n < \frac{\pi}{2} + \lambda + \gamma_0 \\ P_i & \frac{\pi}{2} + \lambda + \gamma_0 \le \theta_n < \frac{3\pi}{2} - \lambda - \xi_4 \\ P_i & \frac{3\pi}{2} - \lambda - \xi_4 \le \theta_n < \frac{3\pi}{2} - \lambda + \xi_5 \\ P_i + m\left(\theta_n - \frac{3\pi}{2}\right) & \frac{3\pi}{2} - \lambda + \xi_5 \le \theta_n < \frac{3\pi}{2} + \lambda + \gamma_0 \\ P_d & \frac{3\pi}{2} + \lambda + \gamma_0 \le \theta_n < 2\pi \end{cases} \quad (2.2)$$

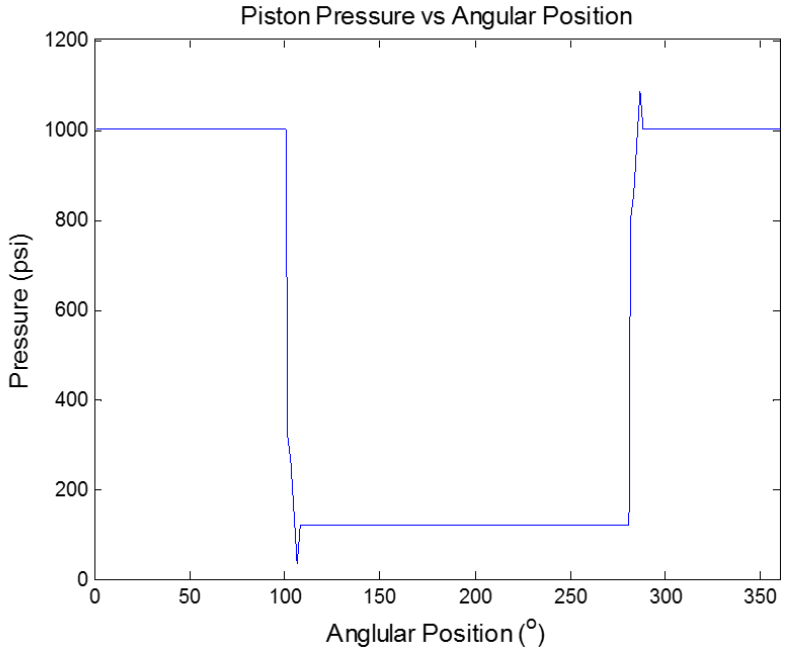

Figure 2.14: Piston Pressure as a function of angular position

The piecewise function provides a good approximation to the pressure exhibited by the pistons. Applying the specific geometry of the valve plate and the size of the pistons as the input to the piecewise function allowed for an accurate representation of the instantaneous piston pressure for the floating valve plate pump used in the experiments. Figure2.14 demonstrates how the piston pressure changes as a function of angular position given the geometry of the valve plate. There are two significant spikes that occur in the piston pressures just after the pistons crosses over the bottom and top dead centers of the pump. When the pistons move across

top and bottom dead centers, because of the dramatic change in motion, either a large drop in pressure or a large spike in pressure can occur depending on whether the piston is moving from the discharge to the suction or suction to discharge respectively. Since the pump has nine pistons, nine piston pressures were evenly spaced in the lubrication model along with the static pressure from the suction and discharge ports to create the final lubrication model for the lubricating gap between the valve plate and cylinder block. The data from the experiments conducted was collected at 0.1 milliseconds increments. Thus the time dependent model was also run at the same time step. The model was run for a total time of 0.3 seconds or 3000 time steps because this allowed for multiple rotations of the cylinder block and the ability to observe multiple vibrations of the valve plate during steady state operation.

Figures 2.15 and 2.16 show the pressure profile in the lubricating gap for the pump operating at a speed of 600 RPM and a discharge pressure of 1200 psi(8.27MPa). Two regions representing the suction pressure of 120 psi(0.827MPa) and a discharge pressure of 1200 psi(8.27MPa) clearly dominate the pressures between the valve plate and cylinder block. Also seen in Figure 2.15 is a circular region that represents a piston pressure moving from the discharge to the suction ports. Because the majority of the pistons are located inside of the discharge and suction regions the pistons maintain the suction or discharge pressure and thus they are unable to be differentiated from the inlet and outlet regions. Only when the pistons are located between the suction and discharge regions can their pressures be differentiated inside of the lubricating gap.

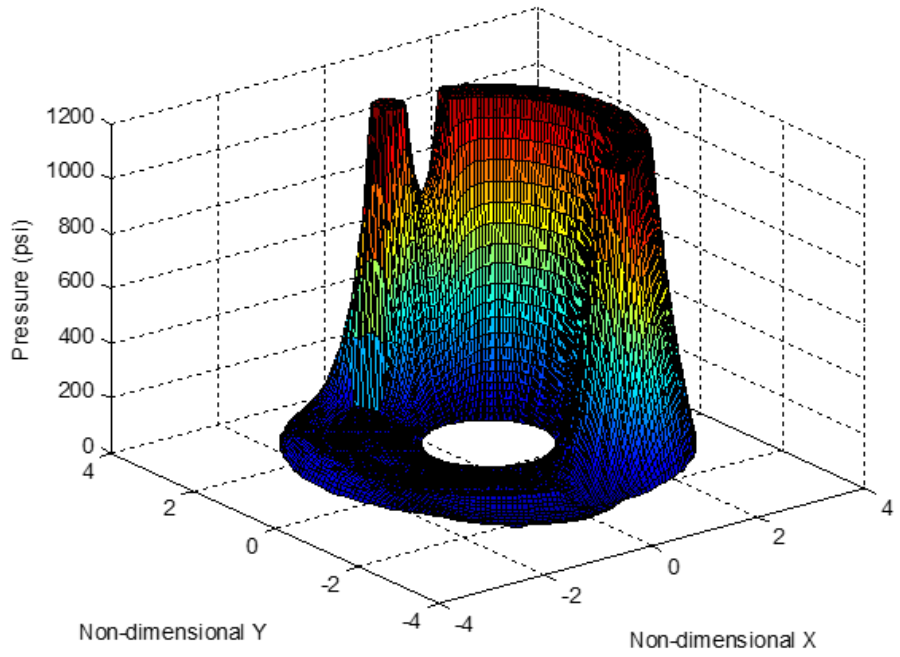

Figure 2.15: Lubricating pressure in valve plate interface at 1200 psi and 600 RPM

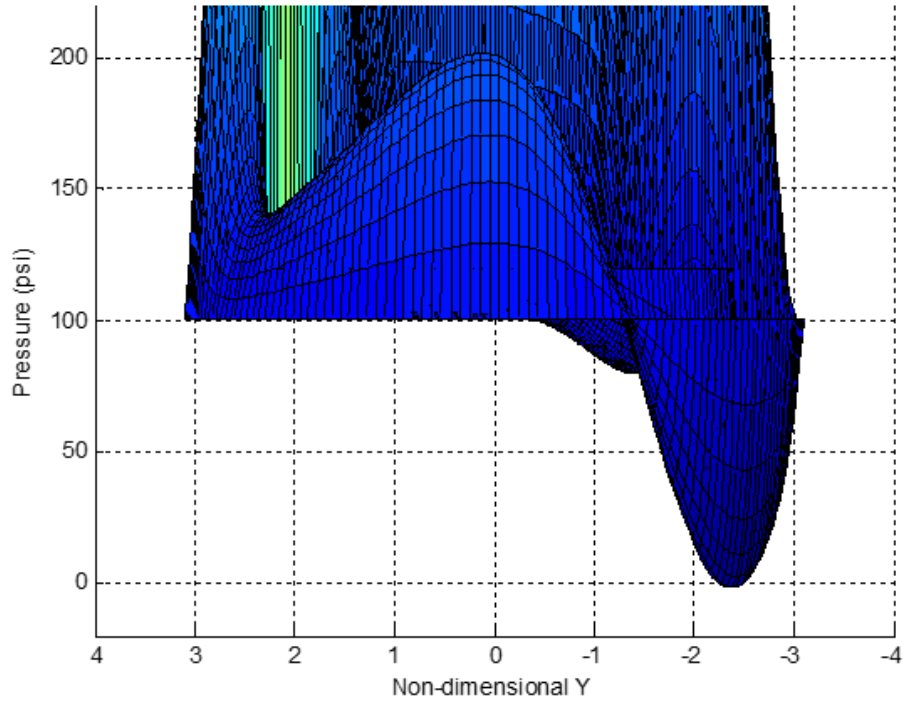

Figure 2.16: Zoomed view of Lubricating pressure in the valve plate interface at 1200 psi and 600 RPM

The experimental results as illustrated in Figure 2.10 demonstrated that the minimum film thickness is located in the middle of the suction side of the valve plate, which is made evident in the pressure profile by a large change in pressure. The change in pressure at this point is due to the fact that the height profile is converging followed immediately by a diverging geometry. In Figure 2.16 a zoomed in view at the location of minimum film thickness, shows a sudden spike followed by an immediate drop in pressure. This is a point of interest in the pressure profile, because this location can potentially cause a large enough drop in pressure that could induce cavitation.

The vibrations of the valve plate measured in the experiments resulted in pressure pulsations. The time dependent squeeze term in the Reynolds equation allowed for the pressure to be affected by the change in height from the vibrations, because as the height decreased the lubricating fluid is compressed causing the pressure to rise. Conversely, if the height at a point is increased the motion is trying to expand the fluid causing a pressure decrease. Although the pressure pulsations were small, usually on the order of about 10 psi(0.068MPa), this phenomenon could still be observed as the film thickness profiles moved through time. The frequency of the pressure pulsations varied between the different operating speeds because the vibrations of the valve plate, which caused the pulsations, directly correlate to the speed of the pump. The main difference observed between the different pressure profiles was the magnitude of the spike and drop in pressure at the minimum film thickness location. Figures 2.17 and 2.18 illustrate how the pressure spike and drop at the location of minimum film thickness can change depending on the operating conditions by showing the pressure profile of the pump operating at 800 psi(5.51MPa) and 900 rpm.

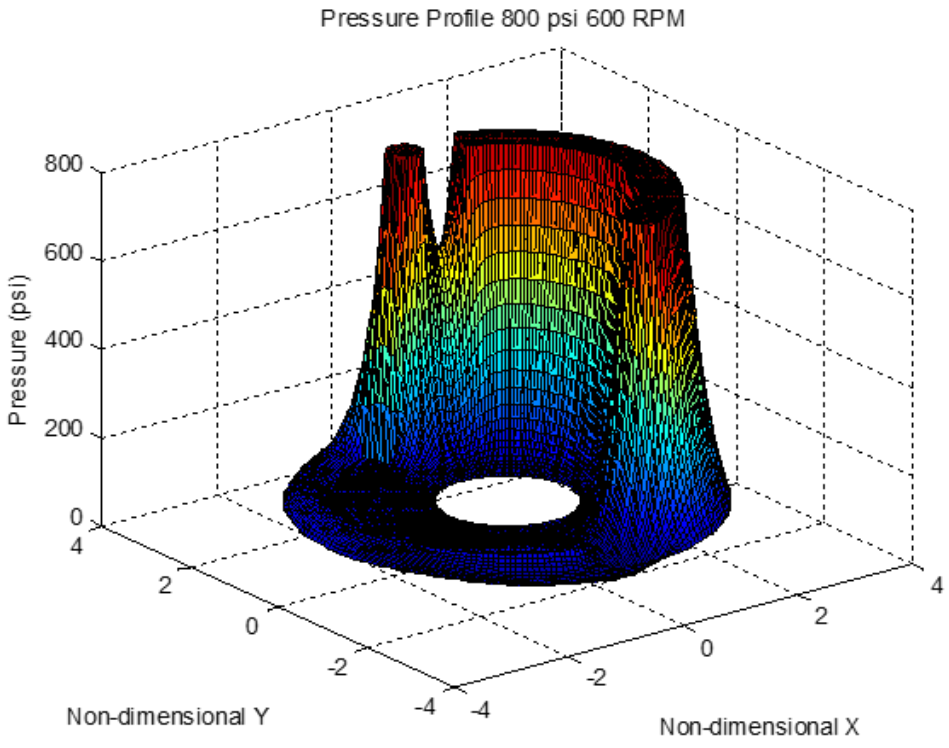

Figure 2.17: Lubricating pressure in valve plate interface at 800 psi and 900 RPM

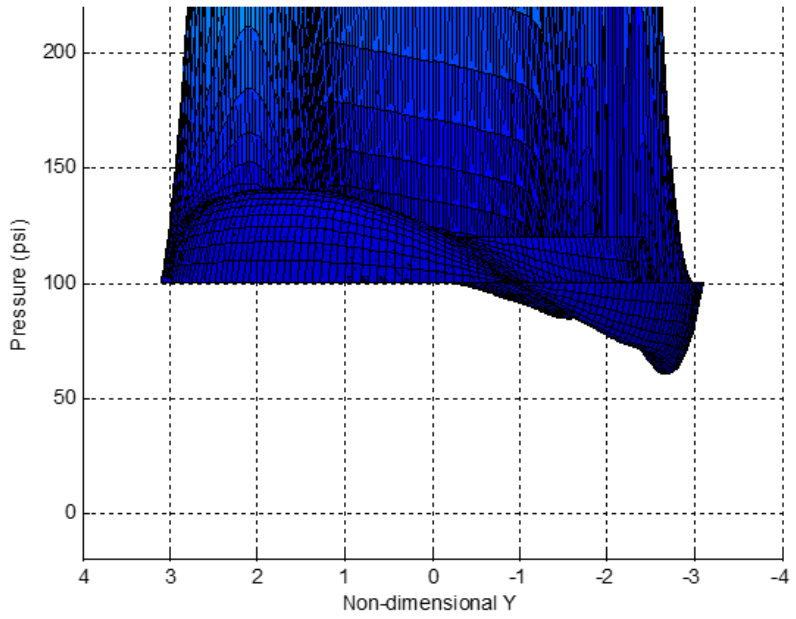

Figure 2.18: Zoomed view of the lubricating pressure in valve plate interface at 800 psi and 900 RPM

As pointed out in the experimental results section, an increase in discharge pressure significantly decreased the minimum film thickness. By decreasing the film thickness the lubricating pressure greatly increases at that location. For example, at 800 psi(5.51MPa) discharge pressure the pressure spike at the minimum film thickness is 160 psi(1.10MPa), whereas in the previous case at 1200 psi(8.27MPa) discharge pressure the pressure spike is 200 psi(1.37MPa). Also the pressure drop after the minimum film thickness is much more severe at higher discharge pressures. At 1200 psi(8.27) the pressure drop reaches a pressure of 0 psi, which is significant because even though the boundary conditions are defined at 100 psi(0.689MPa) case pressure on the inner and outer radii, the lubricating pressure is able to drop to atmospheric pressure due to the movement of the port plate. At a lower discharge pressure of 800 psi(5.51MPa) the pressure at the location of minimum film thickness drops to 60 psi(0.41MPa), which is well above atmospheric pressure but still a significant drop when compared to the case pressure. As made evident in the analytical results, the floating valve plate motion directly affected the pressures seen in the lubricating gap. The vibrations caused pressure pulsations and the overall angle of the plate caused a pressure spike and drop due to the converging and diverging geometries created.

2.5 Conclusions

The film thickness between the floating valve plate and cylinder block in an axial piston pump was measured experimentally through the use of three proximity probes in real time during steady state operation of the pump. An FFT analysis was performed to show that the vibrations in the signal directly correlate to the operating speeds of the pump. The data from the three proximity probes was then used to create film thickness profiles by using the equation of a plane and assuming rigid body dynamics. By comparing this data to the operating conditions it could be seen that as the discharge pressure increased there was a large decrease in minimum film thickness and an increase in the angle of operation. As the operating speed increased there was only a slight increase in minimum film thickness and virtually no effect on the angle of operation. Also for every set of operating conditions tested the minimum film thickness occurred on the suction side of the port. The observed trends illustrate the dynamics of a floating valve plate and its ability to change depending on the operating conditions.

The experimental film thicknesses results were then used in a time dependent lubrication model to visualize how the changes in height affected the lubricating pressures. Appropriate boundary conditions such as the instantaneous piston, suction, and discharge pressures were also included in the analytical model. With all of the boundary conditions defined, the analytical model was simulated at a time step of 0.1 milliseconds and for a total time of 0.3 seconds. The data from the model showed that there were pressure pulsations as a direct result of the oscillating motion of the valve plate. It was also observed at the location of minimum film thickness occurred a large pressure spike followed by a pressure drop due to the converging and diverging geometries at that point. As the discharge pressure increased, the minimum film thickness decreased, causing a larger spike and drop in pressure at that point. Thus the lubricating pressures generated are a direct result of the motion and angle of the valve plate.

3. DYNAMIC MODELING OF FLOATING VALVE PLATE MOTION IN AN AXIAL PISTON PUMP

3.1 Introduction

This chapter presents an analytical and experimental investigation of the motion of the floating valve plate in an axial piston pump under various operating conditions. To achieve the objectives of the analytical investigation, the equations of motion for the valve plate were coupled with a time dependent lubrication model. The balance pistons which support the floating valve plate were represented by equivalent spring & dashpot systems. The system of equations was then solved using the Runge-Kutta and the control volume finite difference methods to determine the pressure, film thickness and motion of the valve plate for various operating conditions. To achieve the experimental objectives, a previously developed axial piston pump test rig was instrumented with proximity probes to measure the motion of the valve plate. The stiffness and damping of the balance pistons supporting the floating valve plate were determined using the impact and frequency response methods. Using the experimentally determined stiffness and damping coefficients in the coupled dynamic lubrication model, the analytical and experimental results of the valve plate motions were compared. The model was then used to conduct a parametric study to determine the overall system stiffness and damping coefficients during pump operation. Using the stiffness and damping coefficients from the parametric study in the dynamic lubrication model the pressure, film thickness and the motion of valve plate was calculated for various operating conditions. The experimental and analytical displacements of the valve plate were then corroborated and found to be in good agreement.

3.2 Dynamic Modeling

The axial piston pump apparatus as previously described was modified and instrumented with three proximity probes to measure the VP motion under various operating conditions ranging between 800 psi (5.51 MPa) to 1200 psi (8.27 MPa) outlet pressure and for a speed ranging from 600 to 1800 RPM. It is important to note that the inlet pressure was kept constant at 120 psi (0.83 MPa) and the case pressure was kept at 100 psi (0.69 MPa) throughout all of the

tests. Figure 3.1 illustrates the three proximity probe set up used to measure the relative VP motion.

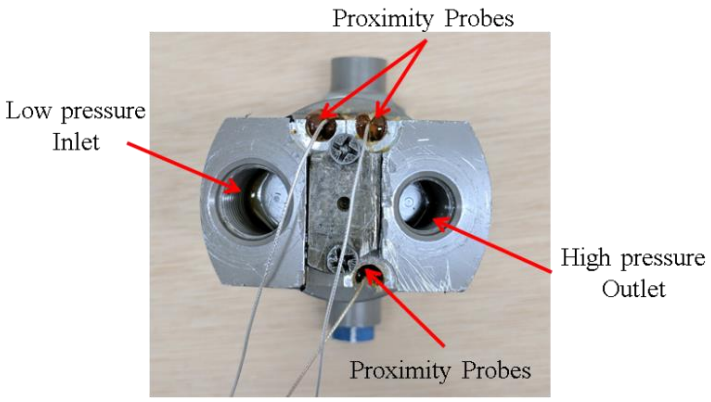

Figure 3.1: Experimental Proximity probe setup for measuring valve plate motion

Ten film thickness measurement tests were performed at each operating condition using the previously described approach The pump used in this investigation could only accommodate three proximity probes; therefore the motion of only three points on the floating VP could be measured. The results from the three proximity probes were assumed to represent the motion of a rigid floating VP and thus represent the film thickness between the VP and cylinder block. It is to be noted that our dynamic modeling of the floating VP demonstrates that this is a good assumption. As previously described, the two main metrics used to assess the film thicknesses are minimum film thickness and Δfilm thickness, which is the difference between the minimum and maximum heights. Figures 3.2 and 3.3 illustrate the average minimum and Δfilm thicknesses for 15 tests at the different operating conditions as described by Table 2.1. The results elucidate that as the discharge pressure is increased the minimum film thickness decreases whereas the Δfilm thickness increases. The results also demonstrate that as the speed is increased there is a slight increase in minimum film thickness however, no change in the Δfilm thickness.

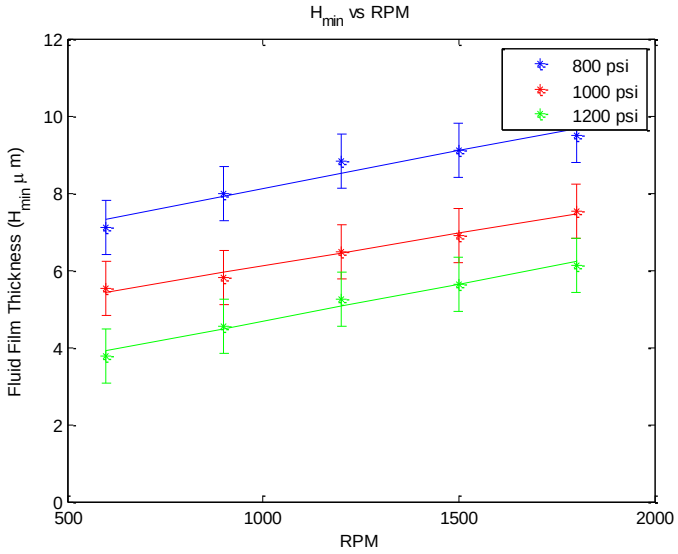

Figure 3.2: Measured Minimum film thickness vs RPM and pressure

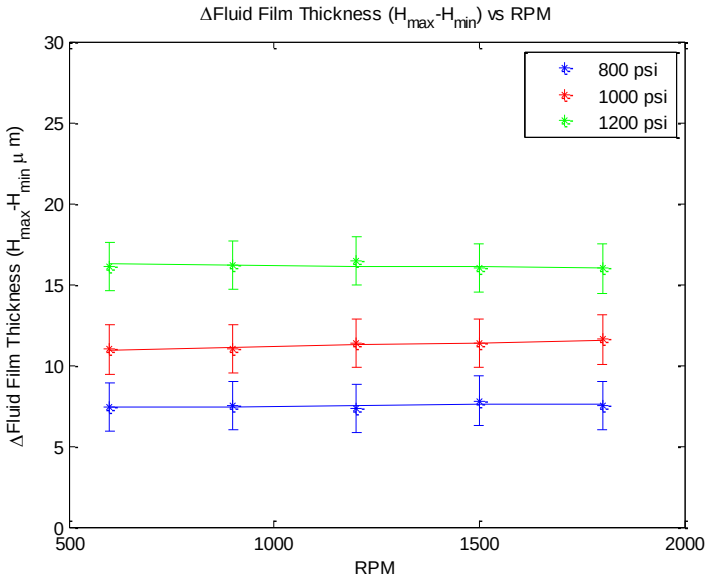

Figure 3.3: Measured Δfilm thickness vs RPM and pressure

In order to model the pressure distribution that can occur between the VP and cylinder block, the time dependent Reynolds equation accounting for cavitation as described by Elrod[1981] was used in this investigation;

$$\frac{\partial}{\partial r}\left(\frac{r\beta h^3 g}{12\mu}\frac{\partial \varphi}{\partial r}\right)+\frac{1}{r}\frac{\partial}{\partial \theta}\left(\frac{\beta h^3 g}{12\mu}\frac{\partial \varphi}{\partial \theta}\right)=\frac{\rho_c r\omega}{2}\frac{\partial h\varphi}{\partial \theta}+\rho_c\frac{\partial h\varphi}{\partial t} \quad (3.1)$$

The purpose for the cavitation algorithm was to observe whether any of the operating condition could induce cavitation and identify locations of potential pitting wear. Using a control volume finite difference approach the Reynolds equation was numerically discretized and then solved for a given film thickness and appropriate pressure boundary conditions. The pressure boundary conditions at the inlet and outlet regions of the VP are described as regions of constant pressure given by the desired operating conditions. A piecewise function developed by Zhang et al. [2008] was used to determine the piston pressure as a function of angular position. As illustrated in Figure 2.14 the instantaneous piston pressure shows the two spikes in pressure that occur near top and bottom dead center. Combining the inlet, outlet, and instantaneous piston pressure boundary conditions with the Reynolds equation allows for a full description of the pressures that occur in the lubricating gap between the VP and cylinder block.

The pressures predicted by the lubrication model are then coupled to the dynamic model which predicts VP motion. This is achieved by integrating the pressure distributions to obtain equivalent force and center of pressure. The center of pressure provides the x and y locations where the equivalent force acts. Equations 3.3 through 3.5 were used to determine the coordinates of the center of pressure and the corresponding force occurring on the VP:

$$X_{cp}=\frac{1}{F_{eq}}\iint_{area} x*P*dA \quad (3.3)$$

$$Y_{cp}=\frac{1}{F_{eq}}\iint_{area} y*P*dA \quad (3.4)$$

$$F_{eq}=\iint_{area} P*dA \quad (3.5)$$

The force and the location of center of pressure are then used in the equations of motion to predict the motion of the VP. As previously described a floating VP is restricted from rotation, however, it is allowed to move and tilt along the cylinder block axis in order to balance the fluid forces generated between the VP and cylinder block. Therefore, the VP was allowed to have only three degrees of freedom Z_{cm}, θ, and φ. Z_{cm} is the vertical motion of the VP from the center of mass, θ is the tilt angle from the x-axis and φ is the tilt angle from the y-axis. Figure 3.4

illustrates the degrees of freedom of a floating VP, showing how Z_{cm}, θ, and φ can affect the orientation and motion of the VP.

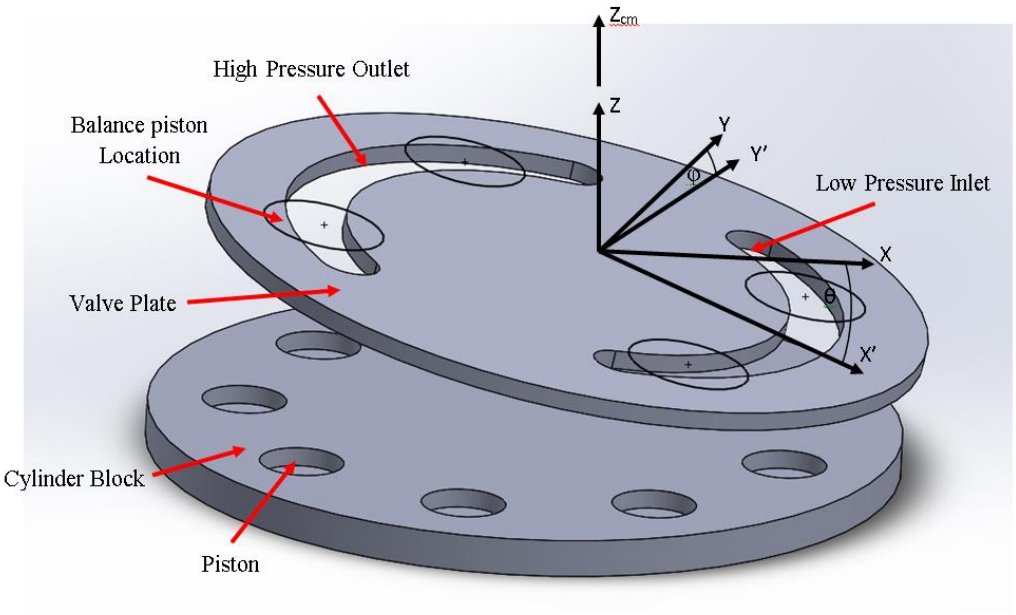

Figure 3.4: Degrees of freedom of valve plate

As previously described, the balance pistons allow the VP to move vertically while restricting the VP from rotating or tilting excessively. To approximate the restriction that the balance pistons induce on the VP, the balance pistons were assumed to behave as spring & dashpot systems. It should be noted that the cylinder block is rigidly connected to the motor shaft therefore, the cylinder block is unable to move and considered grounded. Figure 3.5 illustrates the locations of the four balance pistons along the circumference of the floating VP. Figure 3.5 also depicts the locations of the auxiliary balance pistons. The auxiliary balance pistons are used to mitigate cavitation when the pistons cross over from the suction to discharge or vice versa. This is achieved by providing a small reservoir of fluid so that as the piston crosses over top or bottom dead center the additional fluid can be drawn from the reservoir to prevent cavitation in the piston chamber. The auxiliary balance pistons do not support the VP and thus they were not accounted for in the dynamic model. In addition, the floating VP was assumed to have rigid motion. Using the equivalent force and its location obtained from the lubrication model, the equations of motion were obtained by summing the forces and moments about the center of mass of the VP as shown below:

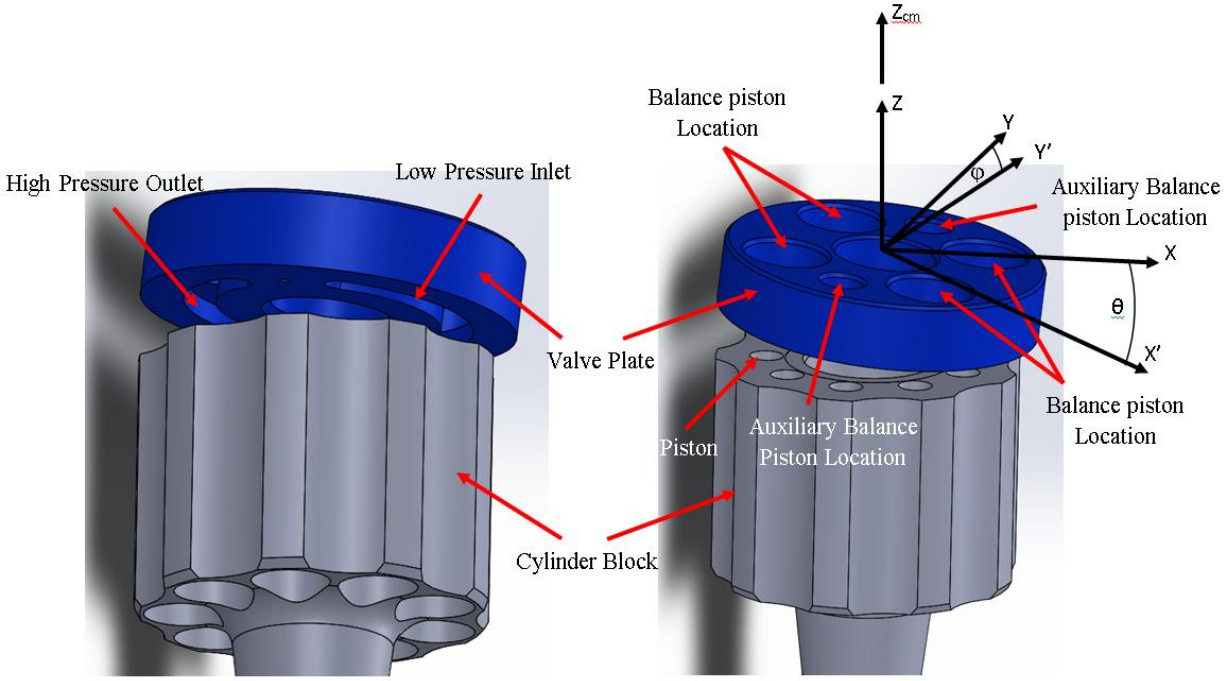

Figure 3.5: Floating Valve plate geometry with balance piston locations

$$
\begin{aligned}
M\ddot{z}_{cm} = \; & -k(x_1\tan(\theta) + y_1\tan(\varphi) + z_{cm}) - k(x_2\tan(\theta) + y_2\tan(\varphi) + z_{cm}) \\
& - k(x_3\tan(\theta) + y_3\tan(\varphi) + z_{cm}) - k(x_4\tan(\theta) + y_4\tan(\varphi) + z_{cm}) \\
& - c\left(x_1\frac{1}{cos^2(\theta)}\dot{\theta} + y_1\frac{1}{cos^2(\varphi)}\dot{\varphi} + \dot{z_{cm}}\right) - c\left(x_2\frac{1}{cos^2(\theta)}\dot{\theta}\right. \\
& \left. + y_2\frac{1}{cos^2(\varphi)}\dot{\varphi} + \dot{z_{cm}}\right) - c\left(x_3\frac{1}{cos^2(\theta)}\dot{\theta} + y_3\frac{1}{cos^2(\varphi)}\dot{\varphi} + \dot{z_{cm}}\right) \\
& - c\left(x_4\frac{1}{cos^2(\theta)}\dot{\theta} + y_4\frac{1}{cos^2(\varphi)}\dot{\varphi} + \dot{z_{cm}}\right) + F_{eq}
\end{aligned}
\tag{3.6}
$$

$$
\begin{aligned}
I_{yy}\ddot{\theta} = \; & -kx_1(x_1\tan(\theta) + y_1\tan(\varphi) + z_{cm}) - kx_2(x_2\tan(\theta) + y_2\tan(\varphi) + z_{cm}) \\
& - kx_3(x_3\tan(\theta) + y_3\tan(\varphi) + z_{cm}) \\
& - kx_4(x_4\tan(\theta) + y_4\tan(\varphi) + z_{cm}) \\
& - cx_1\left(x_1\frac{1}{cos^2(\theta)}\dot{\theta} + y_1\frac{1}{cos^2(\varphi)}\dot{\varphi} + \dot{z_{cm}}\right) \\
& - cx_2\left(x_2\frac{1}{cos^2(\theta)}\dot{\theta} + y_2\frac{1}{cos^2(\varphi)}\dot{\varphi} + \dot{z_{cm}}\right) \\
& - cx_3\left(x_3\frac{1}{cos^2(\theta)}\dot{\theta} + y_3\frac{1}{cos^2(\varphi)}\dot{\varphi} + \dot{z_{cm}}\right) \\
& - cx_4\left(x_4\frac{1}{cos^2(\theta)}\dot{\theta} + y_4\frac{1}{cos^2(\varphi)}\dot{\varphi} + \dot{z_{cm}}\right) + X_{cp}F_{eq}
\end{aligned}
\tag{3.7}
$$

$$
\begin{aligned}
I_{xx}\ddot{\varphi} = \; & -ky_1(x_1\tan(\theta) + y_1\tan(\varphi) + z_{cm}) - ky_2(x_2\tan(\theta) + y_2\tan(\varphi) + z_{cm}) \\
& - ky_3(x_3\tan(\theta) + y_3\tan(\varphi) + z_{cm}) \\
& - ky_4(x_4\tan(\theta) + y_4\tan(\varphi) + z_{cm}) \\
& - cy_1\left(x_1\frac{1}{cos^2(\theta)}\dot{\theta} + y_1\frac{1}{cos^2(\varphi)}\dot{\varphi} + \dot{z_{cm}}\right) \\
& - cy_2\left(x_2\frac{1}{cos^2(\theta)}\dot{\theta} + y_2\frac{1}{cos^2(\varphi)}\dot{\varphi} + \dot{z_{cm}}\right) \\
& - cy_3\left(x_3\frac{1}{cos^2(\theta)}\dot{\theta} + y_3\frac{1}{cos^2(\varphi)}\dot{\varphi} + \dot{z_{cm}}\right) \\
& - cy_4\left(x_4\frac{1}{cos^2(\theta)}\dot{\theta} + y_4\frac{1}{cos^2(\varphi)}\dot{\varphi} + \dot{z_{cm}}\right) + Y_{cp}F_{eq}
\end{aligned}
\tag{3.8}
$$

The equations of motion were integrated using the fourth order Runge-Kutta method to determine the VP motion as a function of operating conditions. In order to corroborate experimental and analytical results, the lubrication model was simulated for the same operating conditions (i.e. outlet pressure ranging between 800 psi (5.51 MPa) to 1200 psi (8.27 MPa) and speed ranging between 600-1800 RPM). The time step was set to 1 millisecond and for every operating condition the model was simulated for a total of 1000 steps or 1 second. The initial height profile given to the VP was set to a constant 25μm.

3.3 Stiffness and Damping Measurements

The stiffness and damping coefficients of the balance pistons which support the floating VP were determined experimentally using the logarithmic decrement method. The logarithmic decrement method involves measuring the vibrational response of the VP in the axial direction subject to an impact load. From the amplitude of the vibrations, the resulting stiffness and damping of the system can be determined. The experimental setup entailed placing the top of the housing in a vice, which ensures that the housing is grounded and unable to move. By placing the VP system in a housing that is grounded, the tilt of the VP system is reduced ensuring axial motion and accurate results. The balance pistons along with the VP were then assembled in the housing and an accelerometer was mounted on top of the VP near the top dead center location as shown in Figure 3.6.

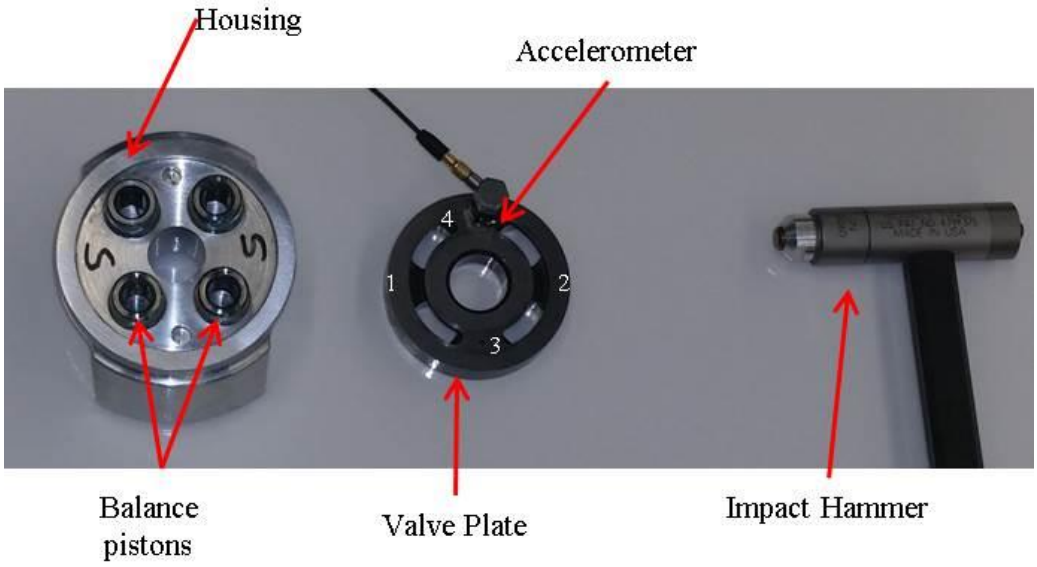

Figure 3.6: Experimental setup for measuring spring and damping coefficients

A total of 80 impact tests were performed and the vibration was sampled of 12 kHz. An impact hammer was used to perform the tests and the VP was impacted 20 times in four different locations as shown in Figure 3.6. Figure 3.7 shows the results from multiple impacts tests, showing the force with which the VP was impacted and the vibrational response in G's. Figure 3.7 depicts the vibrational response from a single impact at two different locations. The resulting amplitudes are extremely close even though the VP was impacted at different locations. In both

cases the VP was hit with about 17 lbf (75.62 N) and the maximum G's measured in either location is 27.3 g and 27.8 g respectively. The small difference between the two measurements illustrates that the vibrational output is independent of impact location. By calculating the logarithmic decay of the measured vibrational response seen in Figure 3.7, the natural frequencies and stiffness and damping coefficients could then be calculated using the following equations:

$$\delta = \frac{1}{n}\, ln\left(\frac{x(t)}{x(t+nT)}\right) \tag{3.9}$$

$$\varsigma = \frac{1}{\sqrt{1+\left(\frac{2\pi}{\delta}\right)^2}} = \frac{C_{sys}}{2\sqrt{K_{sys}M_{sys}}} \tag{3.10}$$

$$\omega_n = \frac{\omega_d}{\sqrt{1-\varsigma^2}} = \sqrt{\frac{K_{sys}}{M_{sys}}} \tag{3.11}$$

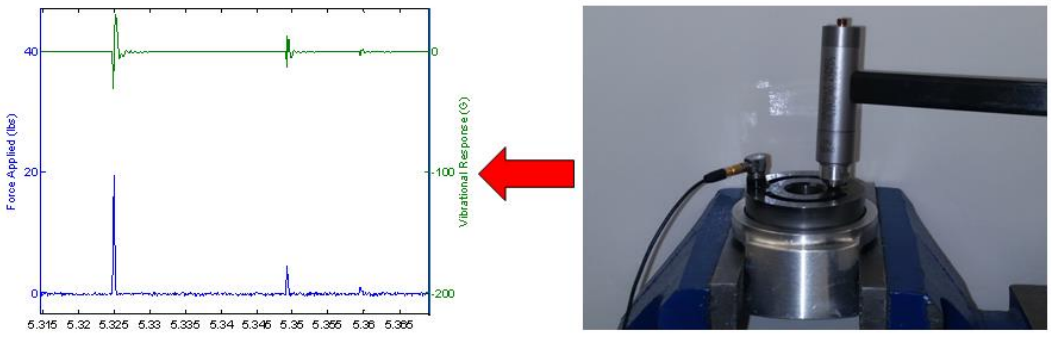

Figure 3.7: Impacted Valve plate with resulting data from accelerometer and impact hammer

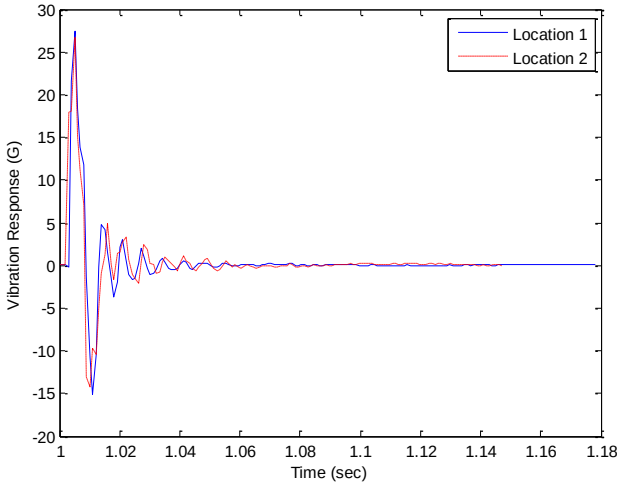

Figure 3.8: Vibration response from impacted valve plate at locations

The resulting spring and damping coefficients from the impact experiments were 5.10×10^7 N/m and 3.34×10^4 Ns/m, respectively. The standard deviations for the spring and damping coefficients are 0.24×10^7 N/m and 0.171×10^4 Ns/m, respectively. This illustrates good consistency across all test locations. It is important to note that the stiffness and damping coefficients obtained from our impact tests for a floating VP axial piston pump differ from those obtained by Chen et al. [2006] and Latas et al. [2011]. Chen et al. [2006] and Latas et al. [2011] obtained stiffness and damping coefficients of 1.2×10^7 N/m and 3.4×10^5 Ns/m, respectively for a fixed VP axial piston pump. The stiffness coefficient obtained in our study is about four times greater than the value used by Chen et al., whereas the damping coefficient obtained is ten times less than Chen et al. The difference between the two values suggests that that the stiffness and damping coefficients for a fixed VP system cannot be used to describe a floating VP system. The values determined from the impact test for the floating VP were then used in the dynamic lubrication model to compare with the experimental film thicknesses results. Figures 3.9 and 3.10 depict the comparison of the minimum and Δfilm thickness obtained from the experiments and the dynamic model developed for this investigation.

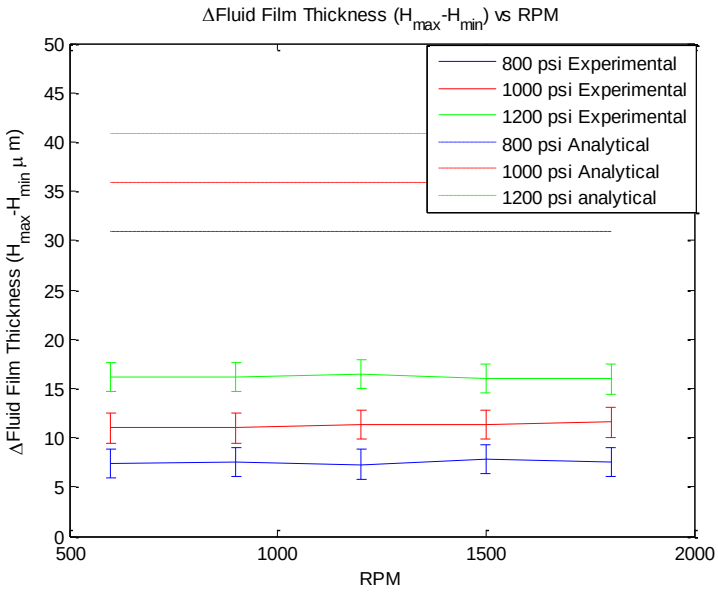

Figure 3.9: Comparison between Δfilm thickness vs RPM and pressure using measured spring and damping coefficients

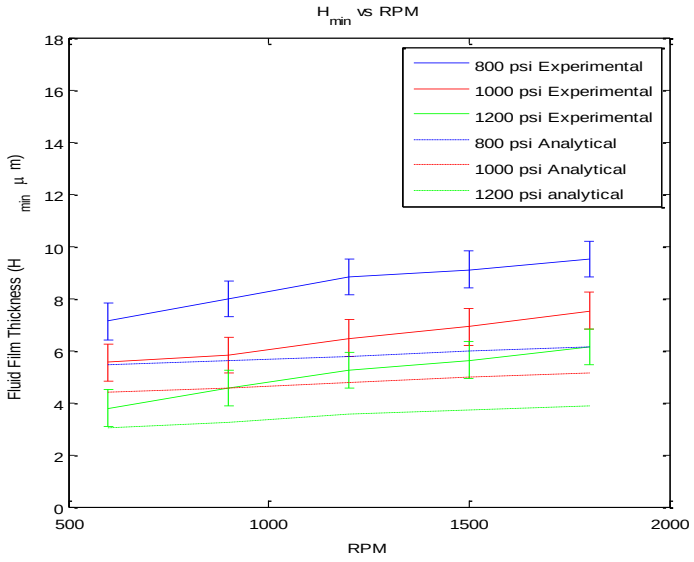

Figure 3.10: Comparison between minimum film thickness vs RPM and pressure using measured spring and damping coefficients

Figure 3.9 demonstrates that the dynamic lubrication model predicted higher Δfilm thicknesses when compared to the experiments. For the case of 1200 psi (8.27 MPa) and 1800 RPM the dynamic model predicted a Δfilm thickness of 40.86 μm whereas the average value obtained from the experiments was 15.97 μm. The difference between the analytical and the experimental results was typical across all operating conditions and indicated that the measured

stiffness coefficients from the impact tests are lower than the actual stiffness and damping of the balance pistons during pump operation. If the stiffness and damping coefficients of the balance pistons were lower than the actual values, the VP would be forced further away from the cylinder block on the outlet side of the pump due to the high discharge pressures, causing an increase in Δfilm thickness.

Figure 3.10 illustrates that the experimentally determined stiffness and damping coefficients led to the dynamic lubrication model predicting lower minimum film thicknesses when compared to the measured values. For example at 800 psi (5.51 MPa) the average decrease in the predicted and experimental film thickness was 51% at 1200 psi (8.27MPa). The reason for this decrease in minimum film thickness is the moment created by the difference in pressures at the outlet and inlet regions. The moment causes the VP to rotate downwards toward the cylinder block at the low pressure inlet and away from the cylinder block at the high pressure outlet. The rotation caused by the moment will decrease the minimum film thickness and therefore, suggests that the stiffness coefficients calculated by the impact tests are too low.

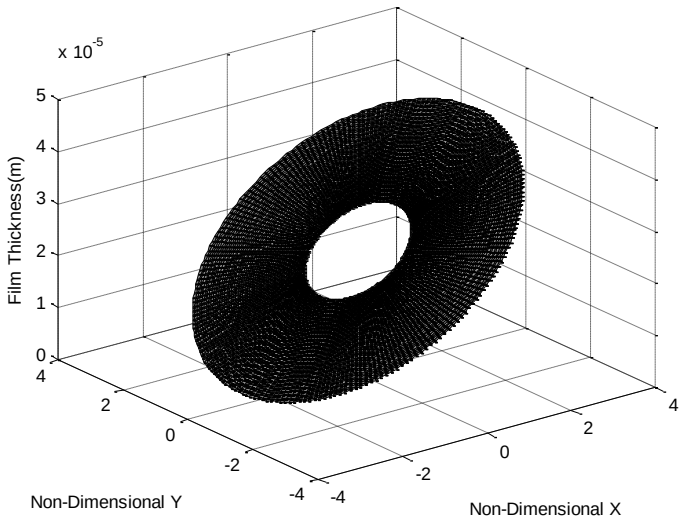

Figure 3.11: Film thickness from dynamic code at 1200psi and 600RPM using measured spring and damping coefficients

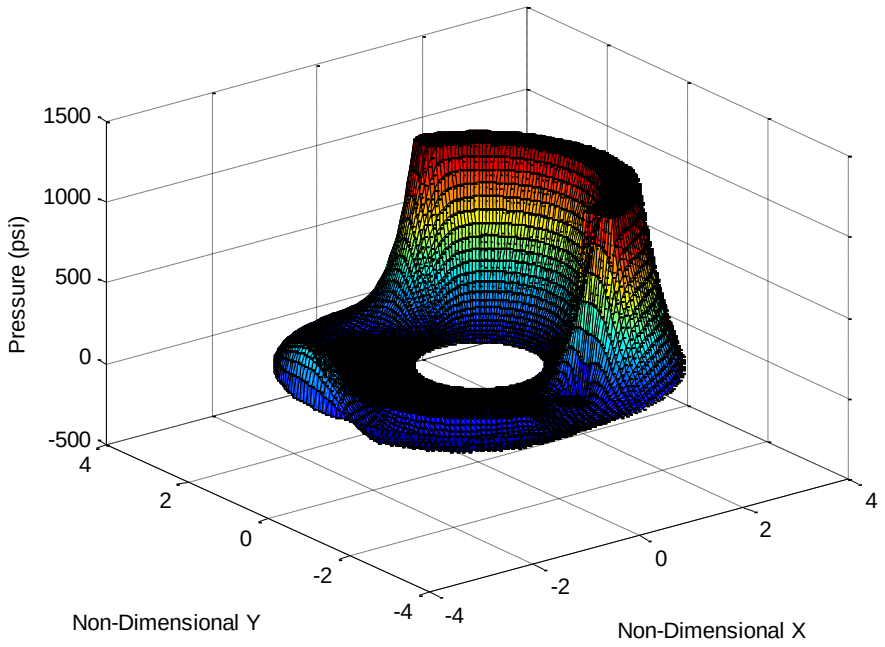

Figure 3.12: Pressure profile from dynamic code at 1200psi and 600RPM using measured spring and damping coefficients

Using the stiffness and damping coefficients from the impact tests, the dynamic lubrication model predicted cavitation. Figures 3.11 and 3.12 depict the film thickness and corresponding pressure profile determined from the lubrication model for the case of 1200 psi (8.27 MPa) and 600 RPM. Figure 3.13 shows the pressure distribution at the location of minimum film thickness. It demonstrates that a large pressure increase precedes the location of minimum film thickness followed by a sharp drop in pressure and a cavitated region. Similar cavitated regions were predicted at the location of minimum film thickness at a discharge pressure of 1200 psi (8.27 MPa) and all operational speeds. At 1200 psi (8.27 MPa) and speeds ≤1200 RPM, the cavitation occurred due to the converging and diverging geometries at the location minimum film thickness. At speeds >1200 RPM even though the average minimum film thickness had increased, cavitation was still predicted due to the motion of the VP.

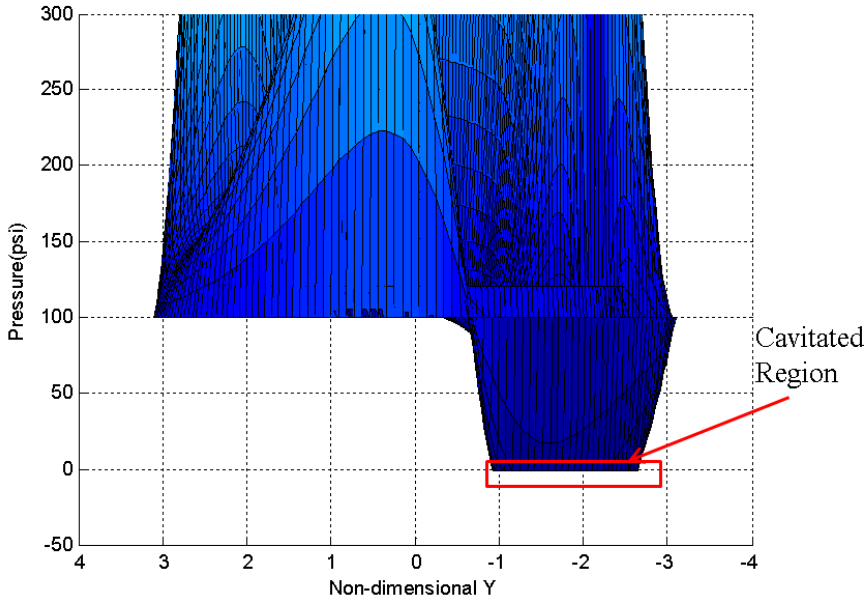

Figure 3.13: Pressure profile at location of minimum film thickness from dynamic code at 1200psi and 600RPM using measured spring and damping coefficients

As described earlier when using the calculated stiffness and damping coefficients obtained from the impact test in the dynamic model, the experimental and model film thickness results did not match. This is primarily due to the fact that the axial piston pump used for this investigation operates in a fully flooded environment and at 100 psi (0.69 MPa) oil pressure. The fluid pressure increases the effective stiffness and damping coefficients for the floating VP system. Please note that the effects of the fluid/oil pressure cannot be accounted for when using an impact test. Therefore, this resulted in predicting a lower spring and damping coefficients of the VP system and thus the discrepancies between the experimental and analytical film thicknesses results.

In order to determine the stiffness and damping coefficients that represent the floating VP system, the most extreme experimental case of 1200 psi (8.27 MPa) and 1800 RPM was used as the baseline for a parametric study. The spring coefficients in the dynamic model were then varied until the average minimum and Δfilm thicknesses were within 1% of the experimental results. To match the damping coefficients appropriately, the measured vibration at the location of minimum film thickness seen in Figure 3.14 was averaged across 10 tests at 1200 psi (8.27 MPa) and 1800 RPM. The average amplitude of the vibration was found to be 0.4 μm. The

damping coefficient was then adjusted such that the vibration amplitude at the minimum film thickness was within 1% of experimentally determined vibration. Figure 3.14 shows excellent correlation between the calculated and measured vibration at 1200 psi (8.27 MPa) and 1800 RPM. The stiffness and damping coefficient that resulted from matching the most extreme experimental condition are 8.72×10^7 N/m and 6.51×10^5 Ns/m respectively. It is to be noted that these coefficients are of a similar order of magnitude as the impact test thus suggesting that these coefficients are reasonable for operating floating VP axial piston pump. The additional fluid forces during pump operation as previously described can account for the increase in spring and damping coefficients. Using the calculated spring and damping coefficients, the dynamic lubrication model was used to determine the pressure and film thickness for all other operating conditions and compared to the experimental film thicknesses.

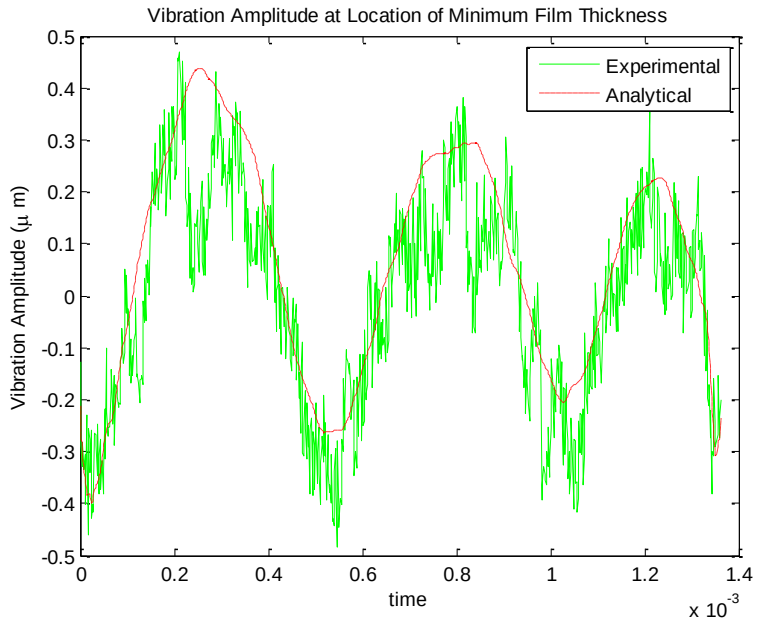

Figure 3.14: : Valve plate vibration at location of minimum film thickness

Figures 3.15 and 3.16 depict the film thicknesses for both the experimental and the dynamic model at 1200 psi (8.27 Mpa) and 1200 RPM. The similarity between the two film thicknesses illustrates that the dynamic model and the experimental results corroborate well. When comparing minimum and Δfilm thickness across all operating conditions as shown in Figures 3.17 and 3.18, there is good agreement between the model and the experiments. For

almost all of the cases the dynamic model prediction falls within the error bounds of the experiments. Also as noted in Figures 3.17 and 3.18, the dynamic lubrication model predicts the minimum and Δfilm thicknesses closer to the experimental results at higher speeds and pressures. At both 1200 psi (8.27 MPa) and 1000 psi (6.89 MPa) and speeds greater than 1200 RPM the dynamic lubrication model compares well with the average minimum film thickness data obtained from the experiments. At lower speeds and pressures the dynamic model deviates more from the average experimental data. The minimum film thickness obtained from the dynamic lubrication model varies from the experiments the most at 1200 psi (8.27 MPa) and 600 RPM. The minimum film thickness predicted by the model at this operating condition is 8.2% outside of the error bounds of the experimental data.

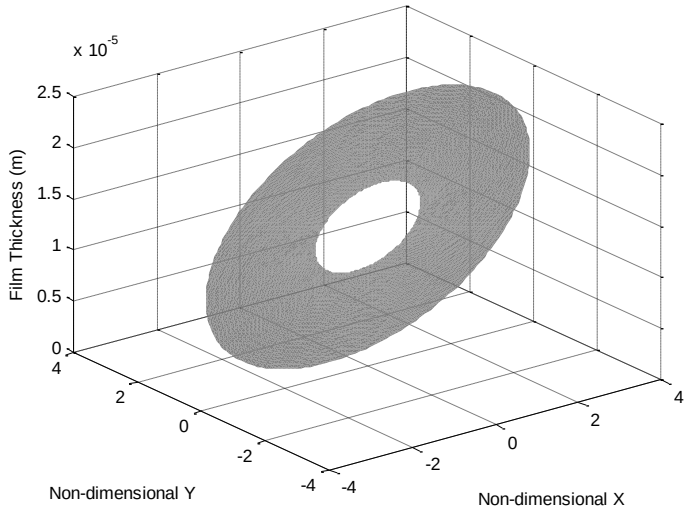

Figure 3.15: Film thickness from experiments at 1200 psi and 1200 RPM

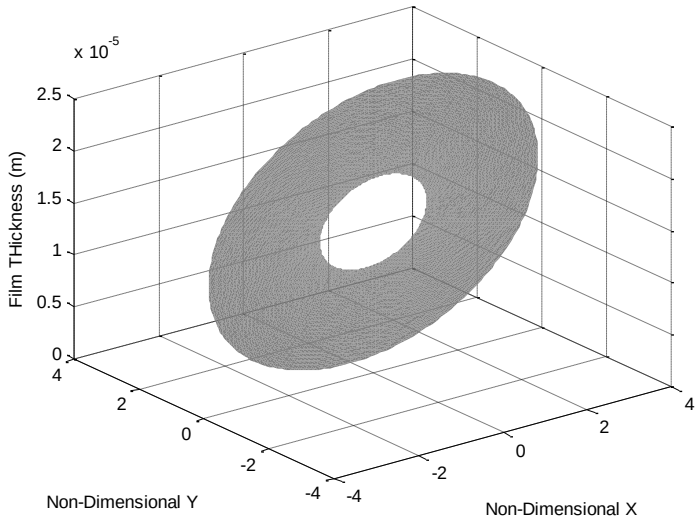

Figure 3.16: Film thickness dynamic model at 1200 psi and 1200 RPM using matched spring and damping coefficients

When comparing the Δfilm thicknesses between the dynamic model and experiments, as seen in Figure 3.18, there is excellent correlation across all operating conditions. The dynamic model predicts results which are well within the error bounds of the experiments at every speed and pressure. In addition, similar trends in the experiments were noticed in the dynamic model such as, if the speed increases the minimum film thickness increases, but has little effect on the Δfilm thicknesses. Another general trend observed in both the model and experiments was that the location of minimum film thickness always occurred on the low pressure side of the VP.

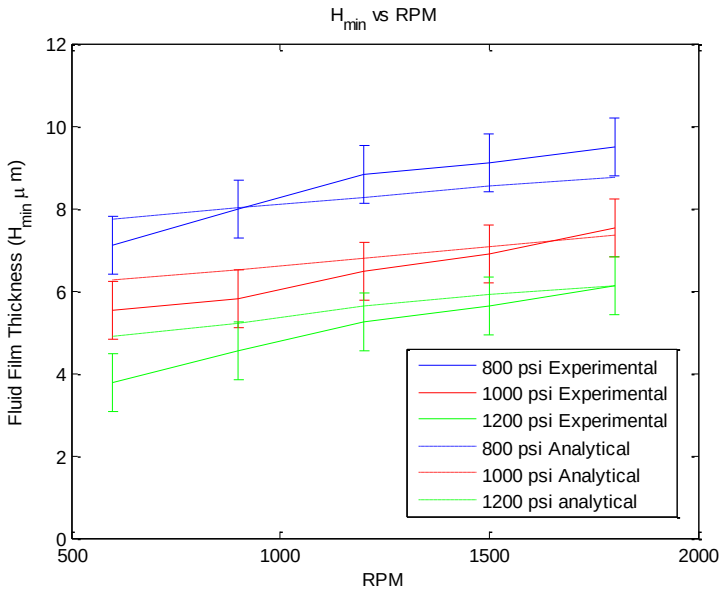

Figure 3.17: Comparison between minimum film thickness vs RPM and pressure using matched spring and damping coefficients

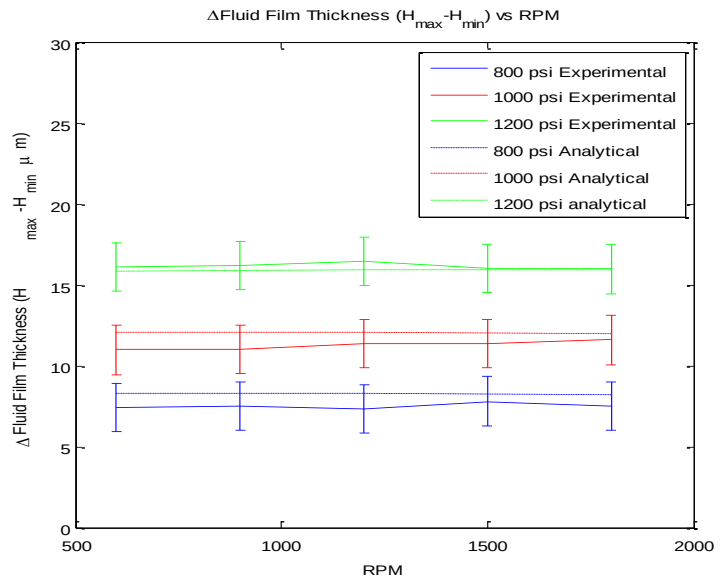

Figure 3.18: Comparison between Δfilm thickness vs RPM and pressure using matched spring and damping coefficients

A typical pressure distribution obtained from the dynamic lubrication model is shown in Figure 3.19. Figure 3.19 illustrates that the inlet and outlet pressures primarily dominate the system however, that there is some variation in the pressure at the location of minimum film

thickness. Figure 3.20 shows a close up view of the pressure at the location of minimum film thickness. Because of the converging and diverging geometry there is a pressure rise followed by an immediate pressure drop. For the case of 1200 psi (8.27 MPa) and 1200 RPM, the model predicts an average minimum pressure of 21.73 psi (0.15 MPa) at the location of minimum film thickness. The pressure drop predicted by the model using the stiffness and damping coefficients from the parametric study is significantly different from the pressure drop predicted using the stiffness and damping coefficients calculated from the impact test. Using the coefficients calculated from the impact test, the model predicted cavitation at 1200 psi (8.27 MPa) discharge pressure and all operational speeds. When the stiffness and damping coefficients calculated from the parametric study, cavitation was never observed at any of the operating conditions.

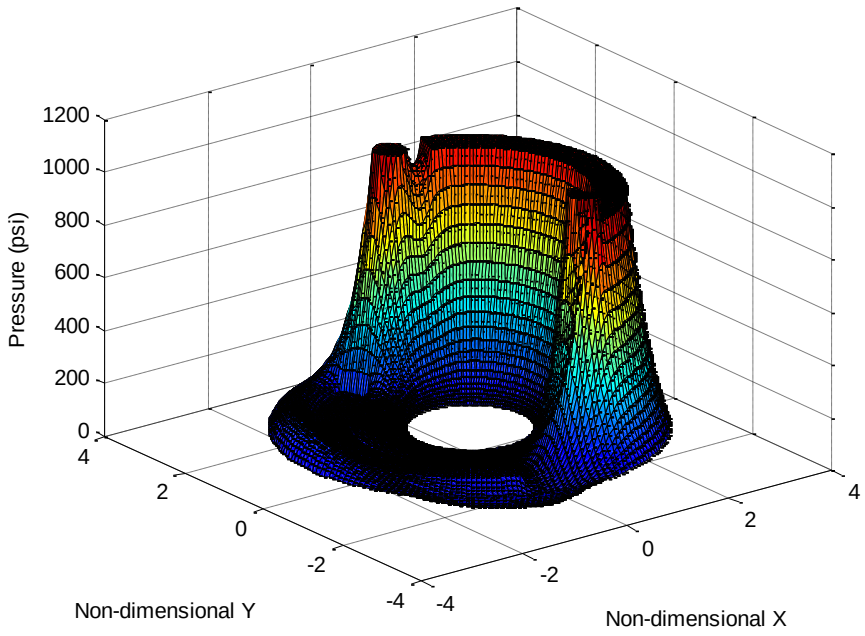

Figure 3.19: Pressure profile from dynamic model at 1200 psi and 1200 RPM using matched spring and damping coefficients

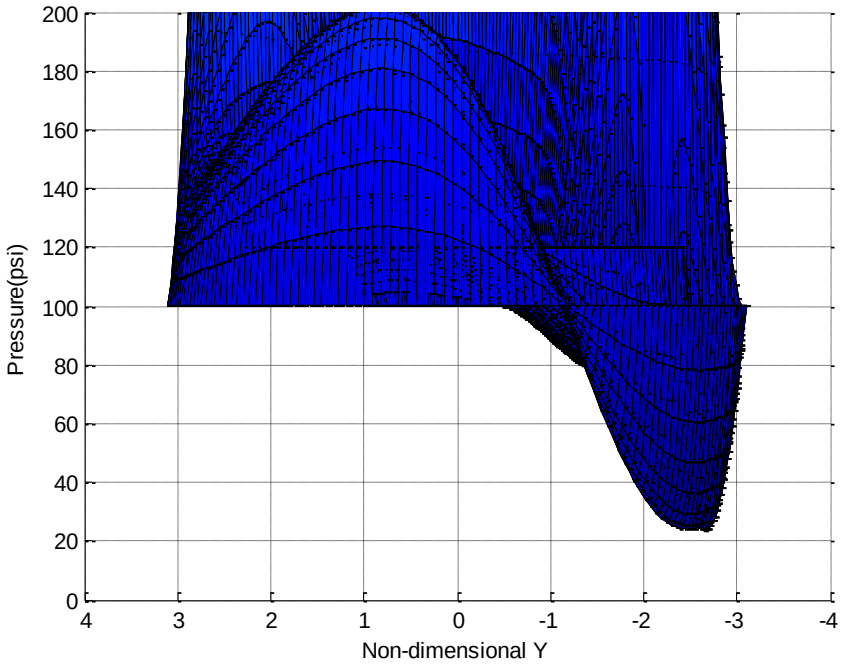

Figure 3.20: Close up view of pressure profile at location of minimum film thickness from dynamic model using matched spring and damping coefficients

3.4 Conclusions

In this investigation an axial piston pump with floating valve plate was instrumented with three proximity probes to measure the displacement (film thickness) of the floating valve plate under various operating conditions. A dynamic model was also developed to determine the VP motion in order to compare with experimental results. In the dynamic model, the balance pistons which support the valve plate were replaced by equivalent spring dashpot systems. The stiffness and damping of the spring dashpot system was determined using the logarithmic decrement method. The equations of motion for the dynamic model were then coupled with a time dependent lubrication equation to determine the pressure and film thickness between the floating VP and cylinder block.

A key finding from the results of the dynamic model was that the calculated spring and dashpot system from the impact tests did not accurately represent the behavior of the floating VP during pump operation. This is primarily due to the fact that the pump operates at 100 psi (0.69 MPa), which can significantly affect the stiffness and damping of the floating valve plate system. Therefore, it can be concluded from the results of this investigation that in order to properly

determine the stiffness, and damping of a floating VP system, it is essential to measure the floating VP motion and then develop a dynamic lubrication model and corroborate experimental and analytical results.

The spring and damping coefficients of the valve plate system were then varied to match the dynamic lubrication model within 1% of the experimental film thickness at the most severe operating condition. Based on this comparison, it was concluded that the spring and damping coefficients for the floating VP system in this investigation are 8.72×10^7 N/m and 6.51×10^5 Ns/m respectively. Using the calculated spring and damping coefficients in the dynamic lubrication model, an analysis was performed across all operating conditions and excellent correlation was observed between the measured and calculated film thicknesses. The exact knowledge of spring and dashpot coefficients will allow for critical examination of various operating conditions and design of axial piston pumps.

4. USING MICRO-PIV TO INVESTIGATE FLUID FLOW IN A THRUST WASHER BEARING

4.1 Introduction

This investigation presents the results of an experimental and analytical investigation of the fluid flow in a pocketed thrust bearing. An experimental test rig was designed, developed and used to visualize fluid flow in pocketed thrust bearings. Micro-particle image velocimetry (μPIV) was used to measure fluid flow inside the pocket of a thrust bearing. The thrust bearings were constructed by gluing precision shim stocks to a flat BK7 glass disk in contact with a polished steel disk. The precision shim stock provides the desired depth of pocket for the bearing. A polished steel disk in contact with the thrust bearing was driven by a motor in order to induce fluid flow within the pockets. μPIV was then employed to measure the shear-driven cavity flow and generate the quiver plots of the flow field. Three different lubricants were used at various speeds and a constant load to measure the effects of speed and viscosity on the flow out of the pocketed thrust bearing. In order to achieve the analytical aspect of this research, a model was developed to predict the film thickness, cavitation area and pressure distribution generated within the bearing. The cavitation areas obtained from the model were compared with the experimental results. The results corroborate well. The calculated pressure and film thickness were then used to determine the 3D velocity profiles within the pocketed thrust bearing. The measured velocities obtained from the experimental images were compared to the analytical velocity fields. Comparing the measured velocities with the analytical model, the depth of the micro-particles in the bearing pocket were determined. Using this approach, the μPIV measured 2D velocity field was converted into a 3D velocity field, which illustrates the fluid motion inside a pocketed thrust bearing at various speeds and viscosities.

4.2 Experimental Setup

In order to achieve the objectives of the experimental aspects of this investigation a test rig was designed and developed to visually inspect the flow and cavitation inside of pocketed thrust bearings. Figure 4.1 depicts the bearings developed for this investigation. Thrust bearings were made of both BK7 glass and acrylic to allow for flow visualization inside of the bearing pocket.

The glass bearings were prepared by machining steel shim stock using an engraving tool on a CNC mill and then gluing it onto a BK7 glass disk using M-Bond 610 strain gage adhesive. This approach resulted in uniform pocket depths equal to the thickness of the shim stock. The use of a fine engraving tool in the machining process ensured that the thin shim stock did not crimp or deform during the machining process. After the bearings were assembled, the steel shim was polished using 2000 grit sand paper to guarantee flatness across the bearing surface. The acrylic bearings were also manufactured using a 3-axis CNC mill and then flame polished and buffed for optical transparency. Both types of bearings were produced with 4 and 8 pocks. All of the pockets were evenly spaced in the circumferential direction, at a radial position of 35 mm from the center. The diameters of the bearing pockets were held constant at 10 mm and were originally machined with a pocket depth of 50 μm. Because both of the bearings were polished and due to variations in the machining processes, the actual pocket depths were found to be 45 ± 4 μm. The pocket depths were measured with and confirmed through an optical surface profilometer.

Figure 4.1: Various Pocket Thrust washer designs

Figure 4.2 illustrates the CAD model and the test rig designed and developed for this investigation. A servomotor was used to drive the runner (steel disk) atop the pocketed thrust bearing. It should be noted that the surface of the runner was polished to a mirror finish in order to provide the best visualization conditions. An encoder was used to measure and control the

servo motor speed. The runner was coupled to a ball and socket joint and attached to the servomotor. The ball joint configuration allowed the runner surface to adjust and remain parallel to the bearing surface. The pocketed thrust bearing was placed in the lubricant reservoir ensuring fully flooded lubrication condition throughout the tests. Load was applied to the bearing by a 10:1 lever arm, with which a constant load of 98 N was used in all of the testing.

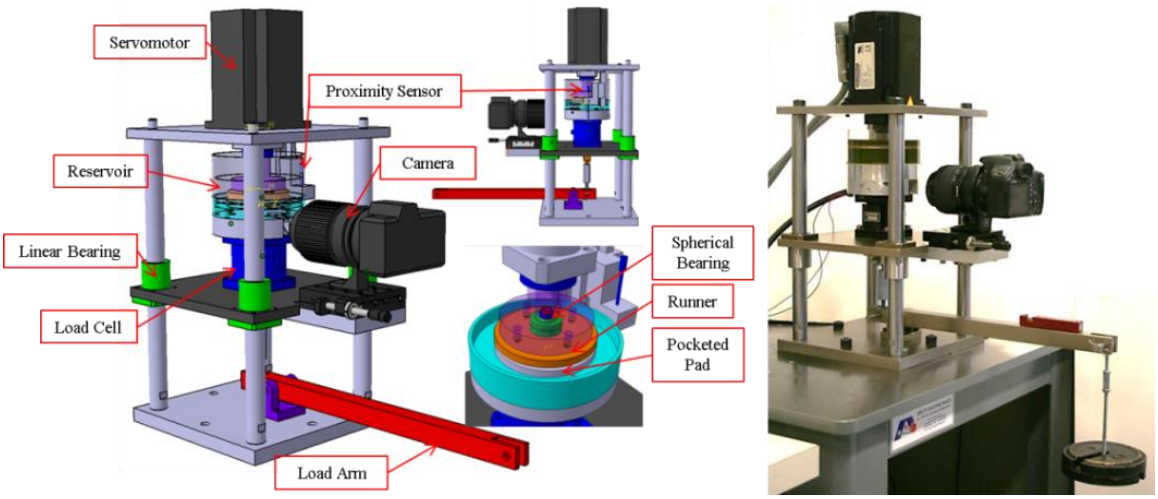

Figure 4.2: Experimental test rig for pocketed thrust Washer

An optical setup similar to that of Cross et al. [2013] was used in this investigation. A window located at the base of the reservoir allowed for visualization of lubricant flow in the bearing pocket. To capture the image, a prism was placed below the window to reflect the image to the camera. Two different cameras were used in this investigation, a digital SLR camera which allowed for high-definition video capture at 60 frames per second (fps) and a high speed video camera that allowed for video capture at a rate of up to 20000 fps with a resolution of 576x624 pixels. A fiber optic white light source was channeled into a block of white plastic to diffuse the light and provide an even intensity across the entire viewing window. Due to the settings of the lens and camera used, the focal depth, or thickness of the focal plane, was able to encompass the entire lubricant film thickness.

A clear colorless PFPE lubricant with a refractive index close to glass and acrylic was used in this investigation. It is also to be noted that the μPIV particles used do not dissolve in the

lubricant. Table 4.1 contains the properties of the three lubricants. Fluorescent dyed particles with a density of 1.11 kgm^{-3} and a diameter of 10 to 15 μm were selected as the seeding particles. These particles were chosen because they are the smallest particles that could be scene in the images captured by the high speed camera. Once the particles were seeded in the lubricant, the mixture was placed in a sonic bath to ensure that the particles were evenly distributed in the fluid, allowing for complete visualization throughout the bearing surface.

Table 4.1 Lubricant Properties

Density	1.85 g/ml
Dynamic viscosity	0.088, 0.755, 3.630 Pa-s
Refractive index	1.31

Using the thrust washer test rig (TWTR), both cavitation ratios and flow velocities were measured as a function of speed, load and viscosity. The cavitation ratio is defined as the area of cavitation inside the pocket divided by the total pocket area. The fluid flow was measured using the μPIV method. Table 4. 2 contains the various conditions for the experiments conducted in this investigation.

Table 4.2 Testing Parameters

Speed (rpm)	20, 50, 100, 150, 200, 250, 300, 350
Load (N)	98
Viscosity (Pa-s)	0.088, 0.755, 3.630
Number of bearing pockets	4, 8
Pocket depth (μm)	45±4
Pocket Diameter (cm)	1

In order to have clear view of the particle flow through the bearing pocket, the captured images used in this investigation were filtered to increase the visibility of the particles. A gradient filter was used in this investigation, which takes the gradient of the grayscale values in a given direction and changes the pixel intensities to represent the gradient values. Utilizing the

gradient filter allowed for ideal visualization of the particles while removing any potential background imperfections

4.3 Experimental Results

The diverging leading edge of the pocket causes the lubricant pressure to drop below the cavitation pressure resulting in a cavitation bubble. Figure 4.3 shows the gaseous cavitation bubble occurring at the leading edge of the pocket. Also shown in Figure 4.3 is the reformation boundary, which is the point where the cavitation stops and the lubricant begins to build pressure due to the converging trailing edge. The cavitation ratios were calculated using the experimental images by measuring the distance from the reformation boundary to the trailing edge of the pocket. Using Equation 4.1 given by Cross et al. [2013], the cavitation ratios were determined for all operating conditions.

$$C.R. = \frac{1}{\pi R^2}\left[R^2 arccos\frac{X-R}{R} - (X-R)\sqrt{R^2-(X-R)^2}\right] \quad (4.1)$$

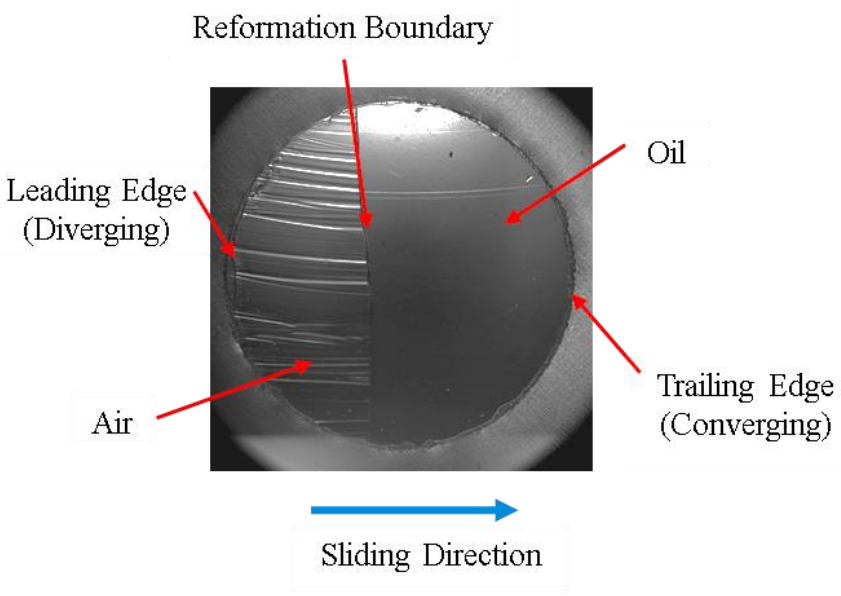

Figure 4.3: Experimental cavitation region for 8 pocket glass bearing η = 0.088 Pa-s at 20RPM

Where *X* is the distance from the reformation boundary to the trailing pocket edge and *R* is the radius of the bearing pocket. It is important to note that when calculating the cavitation

ratios, the reformation boundary is assumed to be a straight and tangent to the flow at all times, some boundaries demonstrated a slightly concave or convex curve. The observed variations in the reformation boundary along the diameter of the pocket are believed to be due to the surface roughness and minor imperfections in the thrust washer. At higher operational speeds it was observed that the reformation boundary became altogether unstable, due to recirculation effects. Other researchers such as Cross et al. [2013] also noticed unstable reformation boundaries due to a reentrant flow of lubricant entering the cavitation region. In this study, the unstable reformation boundaries occurred at speeds greater than 200 RPM. Figure 4.4 shows the average cavitation ratio for the 10 tests performed at each operating condition.

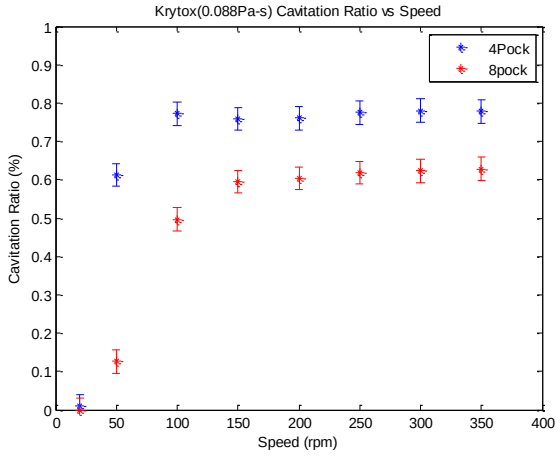

a) η = 0.088Pa-s

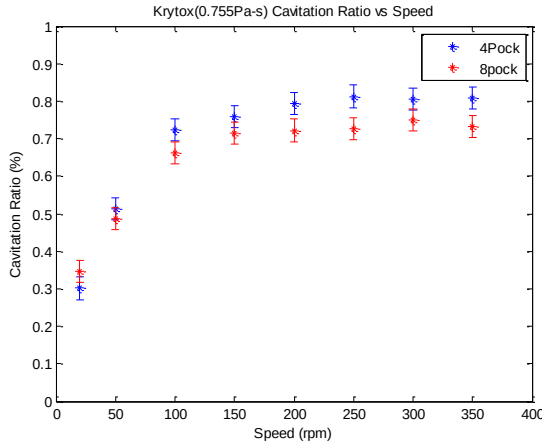

b) η = 0.755Pa-s

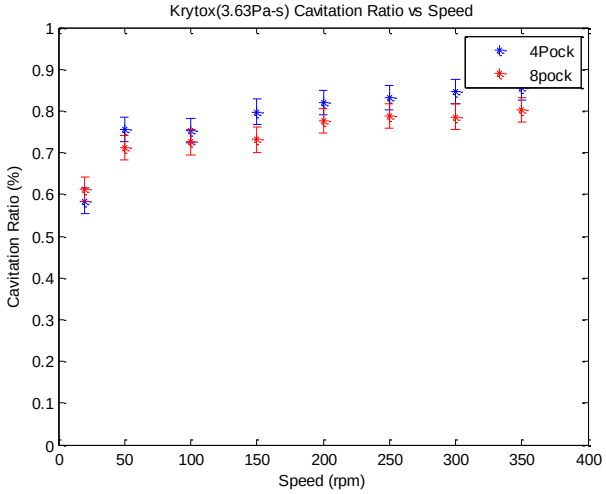

c) η = 3.63Pa-s

Figure 4.4: Measured cavitation ratios

As demonstrated in Figure 4.4, speed had the greatest effect on the cavitation area. At lower speeds (20 to 150 rpm), the cavitation ratio increased rapidly. The rapid change occurs due to the fact that as the speed of the runner is increased the pressure drop on the leading edge also increased, expanding the cavitation area. Once the runner was sufficiently fast to fully support the applied load (>150 rpm), the cavitation area began to be less effected by speed. A slight increase in cavitation area with an increase in viscosity was also observed. On average, the cavitation ratio increased by 0.043 and 0.032 when increasing the viscosity from 0.088 Pa-s

to 0.755 Pa-s and from 0.755 Pa-s to 3.63 Pa-s respectively. Cross et al. [2012] also measured cavitation areas of pocketed thrust bearings and noticed the same trends observed in this investigation.

In order to perform μPIV sequential images taken from the experiments were divided into an equally spaced grid, with small square interrogation windows of 24x24 pixels with 50% overlap. Cross-correlation method was implemented between the images to determine the particle displacement in each interrogation window. The correlation function is given in Equation 4.2 .

$$\Phi_k(m,n) = \sum_{j=1}^{Q}\sum_{i=1}^{P} f_k(i,j) * g_k(i+m, j+n) \tag{4.2}$$

f_k and g_k are the grayscale value distributions of the first and the second exposure, respectively, in the kth image pair. The interrogation window has a size of P × Q pixels. For μPIV, strong background noises can occur causing the signal-to-noise (SNR) to be low. To mitigate this average correlation μPIV (ACμPIV) was implemented. ACμPIV uses an ensemble-averaged correlation function .This method is preferred when laminar and steady-state flow is involved. The average correlation function is given by Equation 4.3.

$$\Phi_{avg}(m,n) = \frac{1}{N}\sum_{k=1}^{N} \Phi_k(m,n) \tag{4.3}$$

Where N is defined as the number of the image pairs. The signal-to-noise ratio can significantly increase as more image pairs are averaged. When using ACμPIV in this investigation, 100 image pairs were used to determine the displacement of the particles. The velocity of the particles can be derived from dividing the displacement by the time interval t.

Evaluating Recordings of Digital Particle Image Velocimetry (EDPIV) software was used for evaluating the recorded images. EDPIV uses the correlation algorithm to calculate the displacements and velocities of the particles in the images. The details of EDPIV can be found in Gui and Wereley [2002] and Wereley and Gui [2003]. Table 4.3 contains the parameters used in EDPIV for the case of η = 3.63Pa-s at 50 rpm with an 8 pocket design. Figures 4.5 and 4.6 show the uniform grid used by EDPIV and the resulting velocity field for the case of η = 3.63Pa-s at 50 rpm with an 8 pocket design.

Table 4.3: EDPIV Settings

Exposure Type	Single
Interrogation window size	24x24
Grid size	12x12
Pix/m	91200

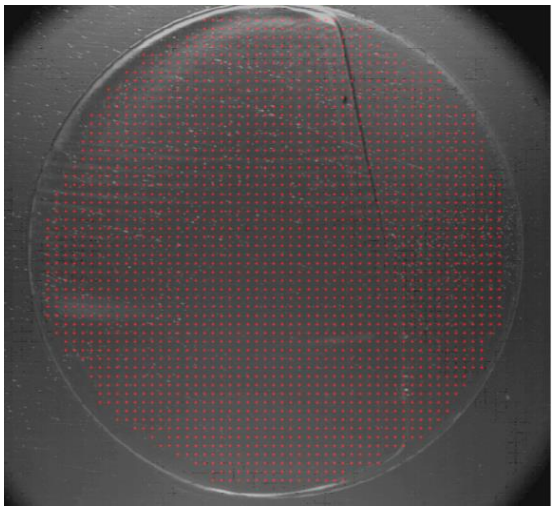

Figure 4.5: Grid used for average correlation PIV

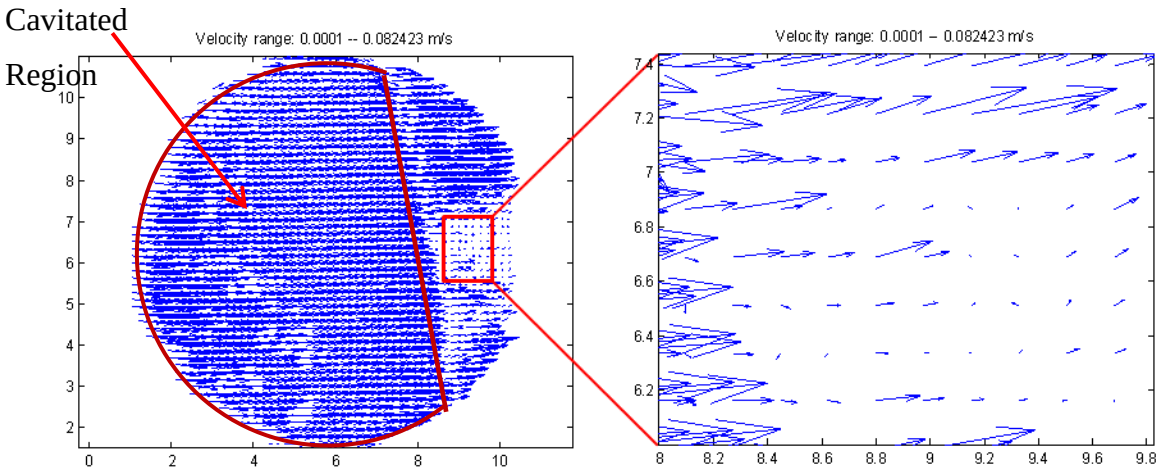

Figure 4.6: Quiver Plots of lubricant flow using average correlation PIV

During the μPIV experiments while recording particles motions, the particles were observed to recirculate after the reformation boundary, however, the velocity field shown in

Figure 4.6 does not explicitly exhibit the recirculation phenomenon. The velocities calculated using ACμPIV indicated that the particles are moving in direction of the runner. Although certain particles in the pocket were experiencing recirculation, other nearby particles at different pocket depths were flowing along the direction of rotation. Due to the averaging that occurs between the particles velocities using the ACμPIV method, the recirculation effects could not be captured from the data. In order to accurately capture the recirculation phenomenon, a different type of μPIV approach called Low Particle Density Particle Image Velocimetry (LDPIV) was implemented.

The main difference between ACμPIV and LDPIV is that while ACμPIV uses a uniformly spaced grid to perform image correlation, LDPIV uses a non-uniform grid. In this approach, the non-uniform grid points are at the location of the particles. Figure 4.7 illustrates the non-uniform grid created from the particle locations used in LDPIV. The interrogation windows placed at each grid point were also decreased in size to 12x12, so as to ensure that only a few particles would be contained in each window. Ensuring a smaller number of particles in each window allows for EDPIV to more accurately capture the flow reversal velocities without being affected by faster moving particles nearby. While this method seems better equipped to measure recirculation, there are drawbacks to LDPIV. Only one pair of images can be used at a time due to the interrogation windows being located on a unique grid. The inability to average the correlation across multiple image pairs will decrease the signal-to-noise ratio, but because of the gradient filtering used in this investigation, good consistent results were able to be obtained.

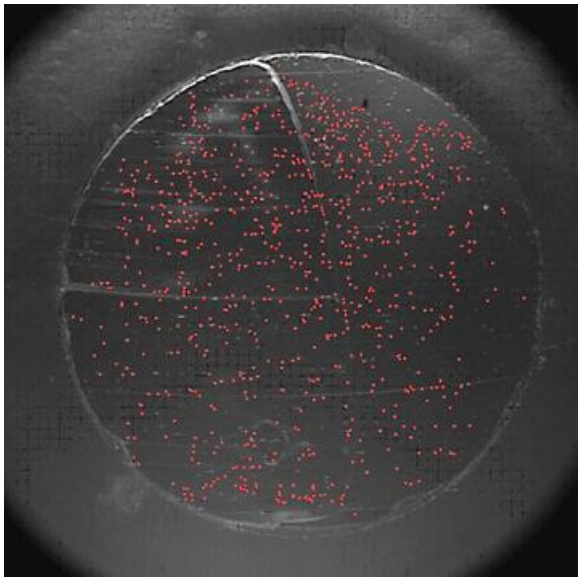

Figure 4.7: Grid Points based on Particle Locations

Figure 4.8 demonstrates the flow velocities measured using LDPIV for $\eta = 0.755$Pa-s at 50 rpm with an 4.8 pocket thrust bearing design. Before the reformation boundary there are a significant number of particles with velocities close to that of the rotating runner. After the reformation boundary, flow reversal is clearly observed, illustrating the recirculation inside the pocket. In the bearing pocket there are a few particles that have velocities that are very close to zero. These particles are assumed to be adhered to the glass surface. Figure 4.9 shows the μPIV measured flows using the different lubricants, for both 4 and 8 pocket designs at 250 RPM. Recirculation is consistently observed in each of the quiver plots as depicted in Figure 4.9. The maximum measured velocity shown in Figure 4.9 is 0.99m/s which is close to the surface velocity of the runner at 1.02m/s.

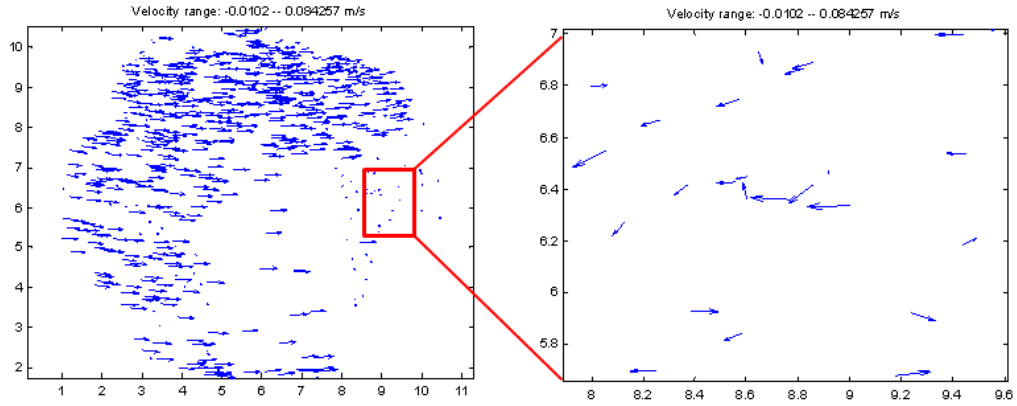

Figure 4.8: Quiver Plots of lubricant flow using LDPIV

The measured velocities demonstrated recirculation across all operating conditions after the reformation boundary. Wang et al. [2011] also measured recirculation in their wide micro channels. In their investigation, the flow inside of the channel was measured from the side of the channel, whereas in this investigation a top view is utilized to measure flow inside of a pocket. Wang et al. [2011] indicated that recirculation inhibited lubricant flow out of bearing pocket (channel).

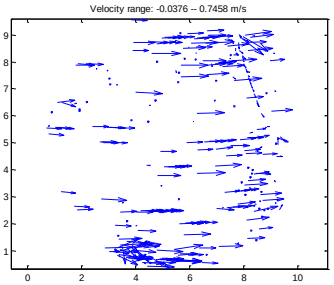

a) 4 pocket η =3.63 Pa-s

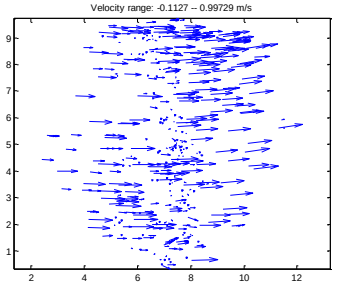

b) 4 pocket η = 0.755 Pa-s

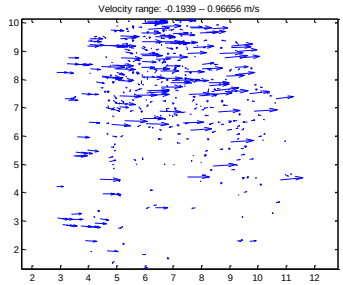

c) 4 pocket η = 0.088

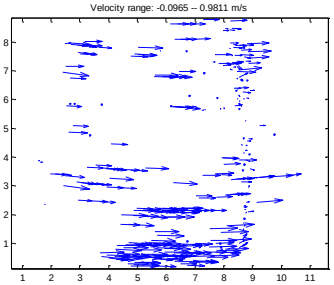

d) 8 pocket η = 3.63

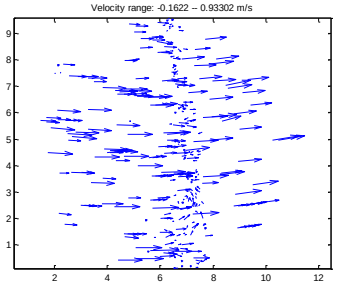

e) 8 pocket η = 0.755 Pa-s

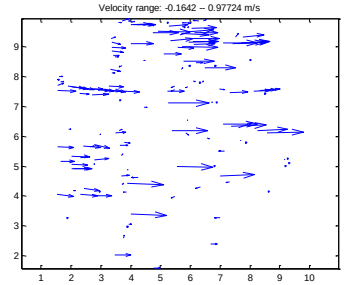

f) 8 pocket η = 0.088 Pa-s

Figure 4.9: Quiver Plots flow comparison at 250 RPM

4.4 Analytical Modeling and Results

A numerical model was developed to determine the pressure, film thickness, cavitation region and velocities in a pocketed thrust bearing for different operating conditions. The results from the numerical model were then used to corroborate with the experimental μPIV. The Reynolds equation modified with the Jacobson-Floberg-Olson boundary condition and film thickness equation were solved simultaneously to determine the pressure, film thickness, and cavitation area for the circular pocketed thrust bearing. A control volume, finite difference numerical scheme similar to Vaijayaraghavan and Keith [1989] was used to solve the Reynolds Equation 4.4 in polar coordinates.

$$\frac{\partial}{\partial r}\left(\frac{r\beta h^3 F}{12\eta}\frac{\partial \phi}{\partial r}\right)+\frac{1}{r}\frac{\partial}{\partial \theta}\left(\frac{\beta h^3 F}{12\eta}\frac{\partial \phi}{\partial \theta}\right)=\frac{r\omega}{2}\frac{\partial}{\partial \theta}(\rho_c h\phi) \tag{4.4}$$

$$h=\begin{cases} h_{min}+h_{step} & for \quad {R_p}^2 > (x-R_{loc}*\cos(t_{loc}))^2+(y-R_{loc}*\sin(t_{loc}))^2 \\ h_{\min} & otherwise \end{cases} \tag{4.5}$$

Equation 4.4 utilizes a switching function (F), to account for both the lubricant film and gaseous cavitation. The switching function is set to zero when the pressure falls below the cavitation pressure which defines the cavitation area. The dimensional pressure is then calculated using Equation 4.6.

$$P=\begin{cases} P=P_c+\beta\ln\phi-P_a & for\ \phi>1 \\ P=P_c-P_a & for\ \phi\le 1 \end{cases} \tag{4.6}$$

To decrease the computational effort and due to symmetry, Equations 4.4 through 4.6 were numerically solved using only one pocket of the thrust bearing. The following is a list of boundary conditions used to simultaneously solve Equations 4.4 through 4.6: i) periodic boundary condition in the theta-direction, ii) atmospheric pressure at the inner and outer radii of the thrust bearing. The numerical model was then used to simulate the same operating conditions as the experiments. Figure 4.10 illustrates the calculated pressure and film thickness generated for a lubricant with η = 0.088 Pa-s operating at 200 RPM with an 8 pocket thrust bearing design.

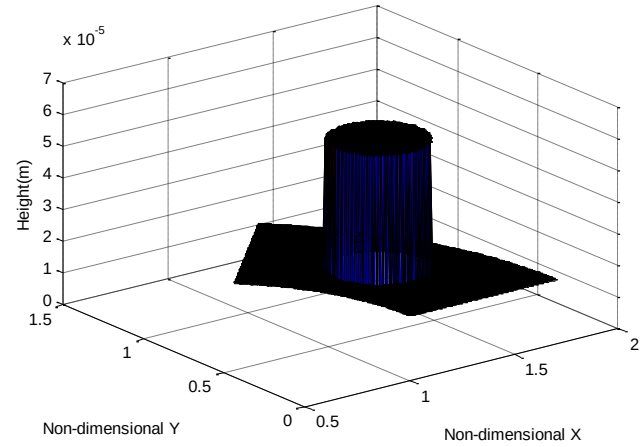

a) Film Thickness

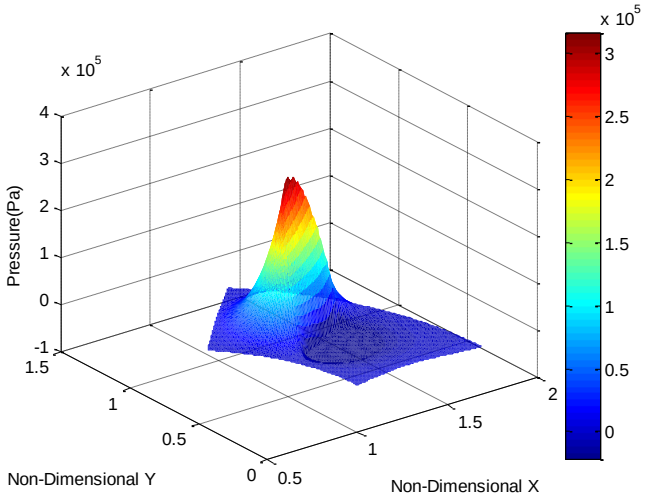

b) Pressure Profile

Figure 4.10: Film thickness and Pressure profiles for η = 0.088 Pa-s at 200 RPM with 8 pocket design

Figure 4.11 illustrates the cavitation ratios obtained from the experiments and analytical model for the case of the oil with η = 0.088 Pa-s at 200 RPM. The experimental and analytical cavitation ratios are 0.60 and 0.64 respectively. Figure 4.12 illustrates a comparison of the results between the experimental and analytical cavitation ratios for all operating conditions considered in this investigation. Higher cavitation ratios with higher speeds and viscosities were observed in the model, which are the same trends noticed in the experimental data. The average

deviation between the experimental and analytical results at speeds of 100 RPM and greater was 5.81%.

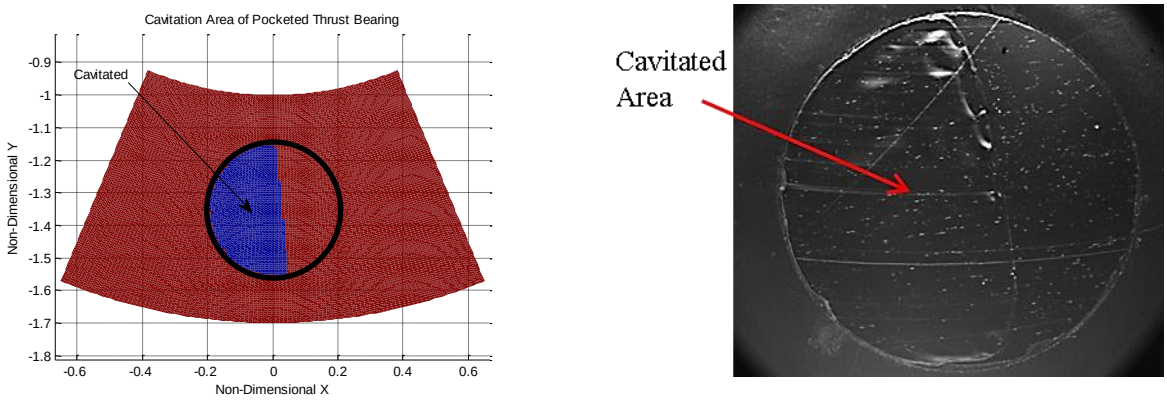

Figure 4.11: Analytic and Experimental cavitation area for η = 0.088 Pa-s at 200 RPM with 8 pocket design

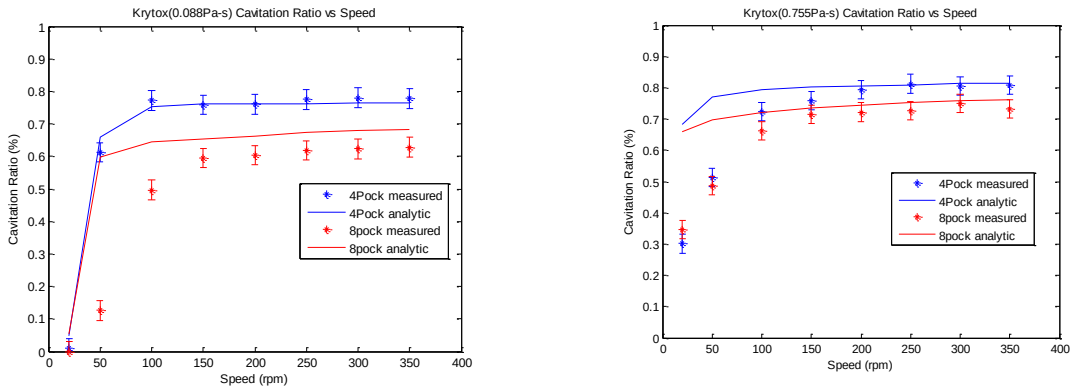

a) η = 0.088Pa-s b) η = 0.755Pa-s

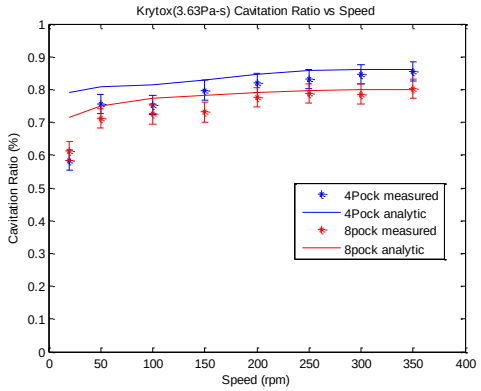

c) η = 3.63Pa-s

Figure 4.12: Cavitation ratio comparison between experiments

In order to calculate lubricant flow within the pocket of the thrust bearing, a similar approach as to Yu and Sadeghi [2002] was implemented in this investigation. The velocities in the radial and tangential directions are given as:

$$V_\theta = \frac{z(z-h)}{2r\eta}\frac{\partial P}{\partial \theta} + \frac{r\omega(h-z)}{h} \tag{4.7}$$

$$V_r = \frac{z(z-h)}{2\eta}\frac{\partial P}{\partial r} \tag{4.8}$$

where $V_\theta = V_r = 0\ at\ z = h$ and $V_\theta = r\omega, V_r = 0\ at\ z = 0$.

The velocity across the film V_z, can be obtained from the continuity equation:

$$\frac{1}{r}\frac{\partial}{\partial r}(rV_r) + \frac{1}{r}\frac{\partial V_\theta}{\partial \theta} + \frac{\partial V_z}{\partial z} = 0 \tag{4.9}$$

where $V_z = 0\ at\ z = 0, h$.

At z = h, which represents the stationary glass disk, the velocities are all equal to zero due to the no-slip boundary condition. Figure 4.13 illustrates V_θ, V_r, and V_z velocities at z = 0.5h for the case of η = 0.755Pa-s at 50 RPM with an 8 pocket design. The negative V_θ values after the reformation boundary demonstrate the recirculation phenomenon in the bearing pocket. The analytical negative V_θ values agree with the negative velocities observed from the experiments. V_z as expected is quite small and negligible, except for at the reformation boundary and at the trailing edge of the pockets. The fluid at the trailing edge flows upward in the pocket, whereas the fluid at the reformation boundary flows downward and out of the pocket.

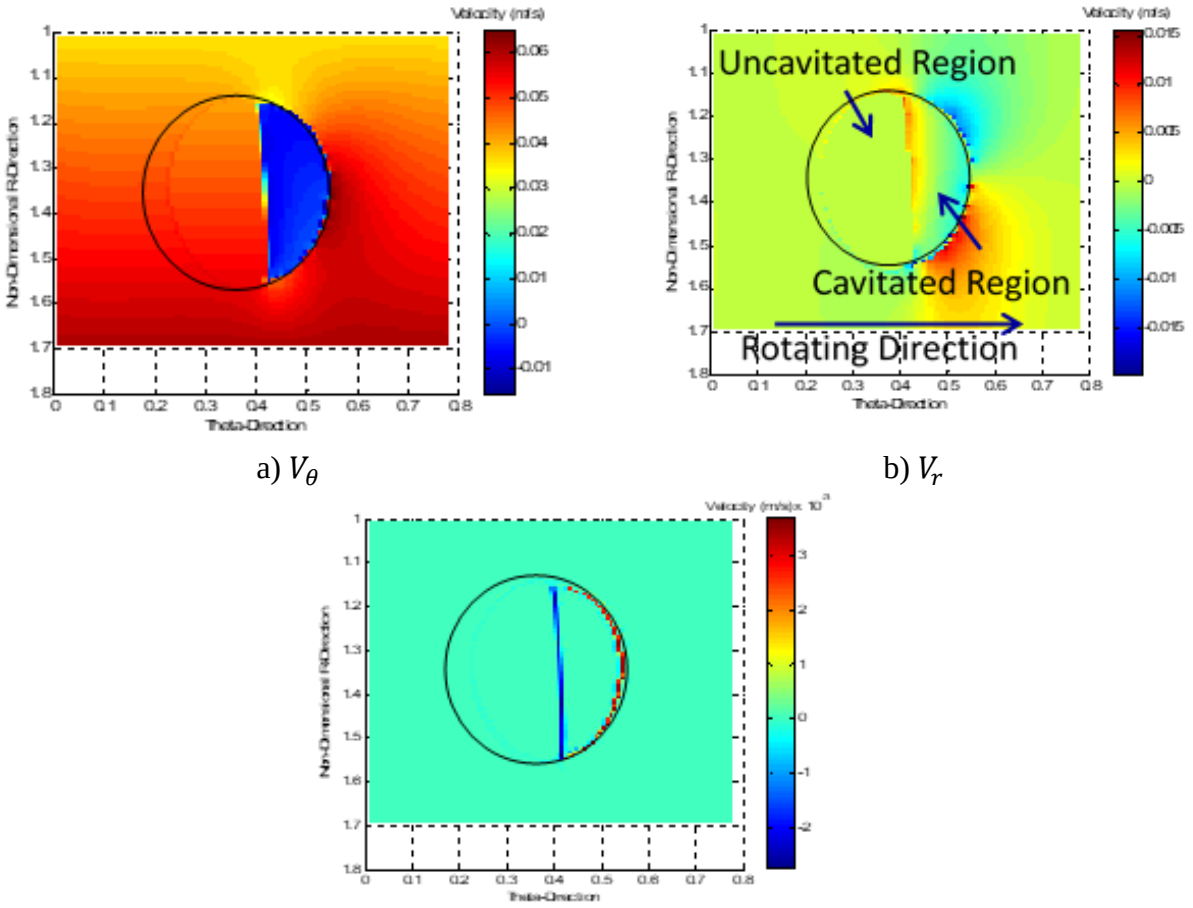

a) V_θ b) V_r

c) V_z

Figure 4.13: Velocities for η = 0.755 Pa-s at 50 RPM, z = 0.5h, 8 pocket design

Figure 4.14 illustrates the velocity vectors along the bearing centerline in the θ-Z plane for η = 0.088 Pa-s at 250RPM. A large recirculation vortex is observed after the reformation boundary. Also shown in Figure 4.14 is that the lubricant velocities in the cavitated region are represented by a Couette flow. Previous investigations, such as Yu and Sadeghi [2000] have also shown in their analytical investigation that flow in the cavitated region is Couette flow.

The analytical and experimental velocities were corroborated and used to convert the 2D measured velocity fields into 3D velocity fields using an interpolation scheme. To achieve this, the x and y locations of the velocities from the experiments and the model were adjusted such that the origin was located at the center of the bearing pocket. At every particle location the corresponding analytical velocity was calculated at 50 equally spaced xy-planes throughout the pocket depth along the z-direction. The analytical velocities along the pocket depth were then

used to interpolate the z-location of the measured velocities. Figure 4.15 illustrates both the 2D and interpolated 3D velocity fields for η= 3.63 Pa-s at 20 RPM and an 8 pocket thrust bearing design.

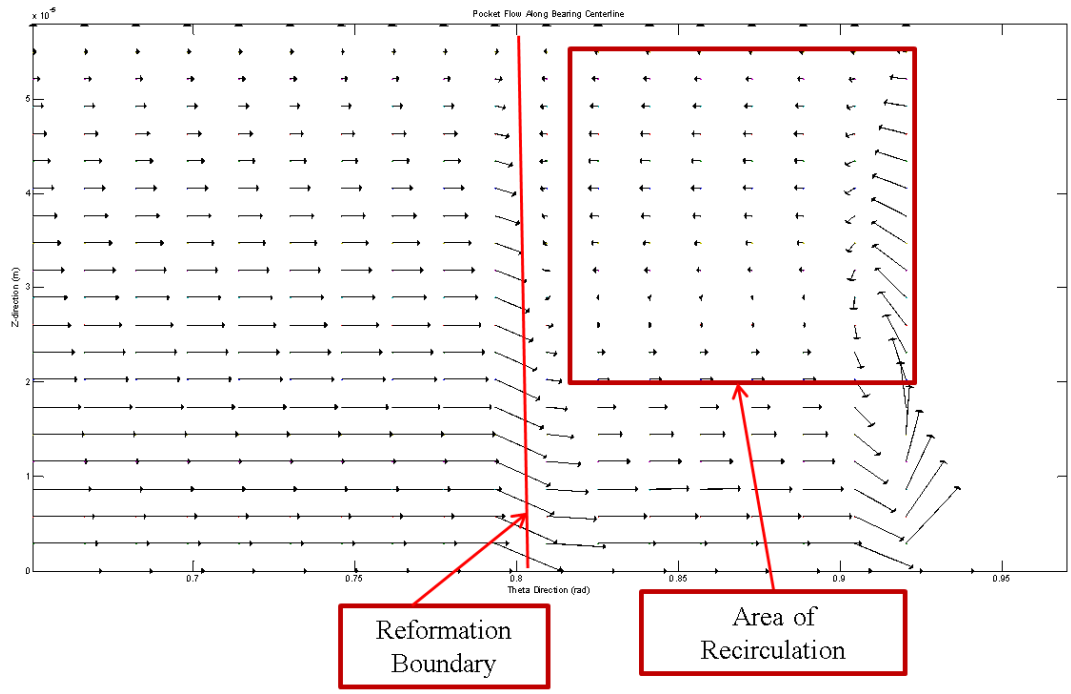

Figure 4.14: Bearing centerline velocities θ-Z plane η = 0.088, Pa-s 250RPM

The 3D and 2D velocity fields look nearly identical when observing the 3D velocities on the z-plane. Along the xz-plane, velocities are shown to be dispersed throughout the pocket depth. Many of the particles have velocities close to that of the runner and are therefore assumed to be located close to the runner surface. After the reformation boundary there are a significant amount of particles with negative V_θ velocities trapped in the recirculation vortex predicted by the numerical model. Other particles with a near zero velocity are observed to be very close to the glass surface due to the no-slip condition. For every LDPIV measured velocity field, at least 91% of the measured velocities matched with the analytical velocity field. Figure 4.16 depicts the 3D velocity fields for η = 0.755 Pa-s at 50, 150, 350 RPM with a 4 pocket design.

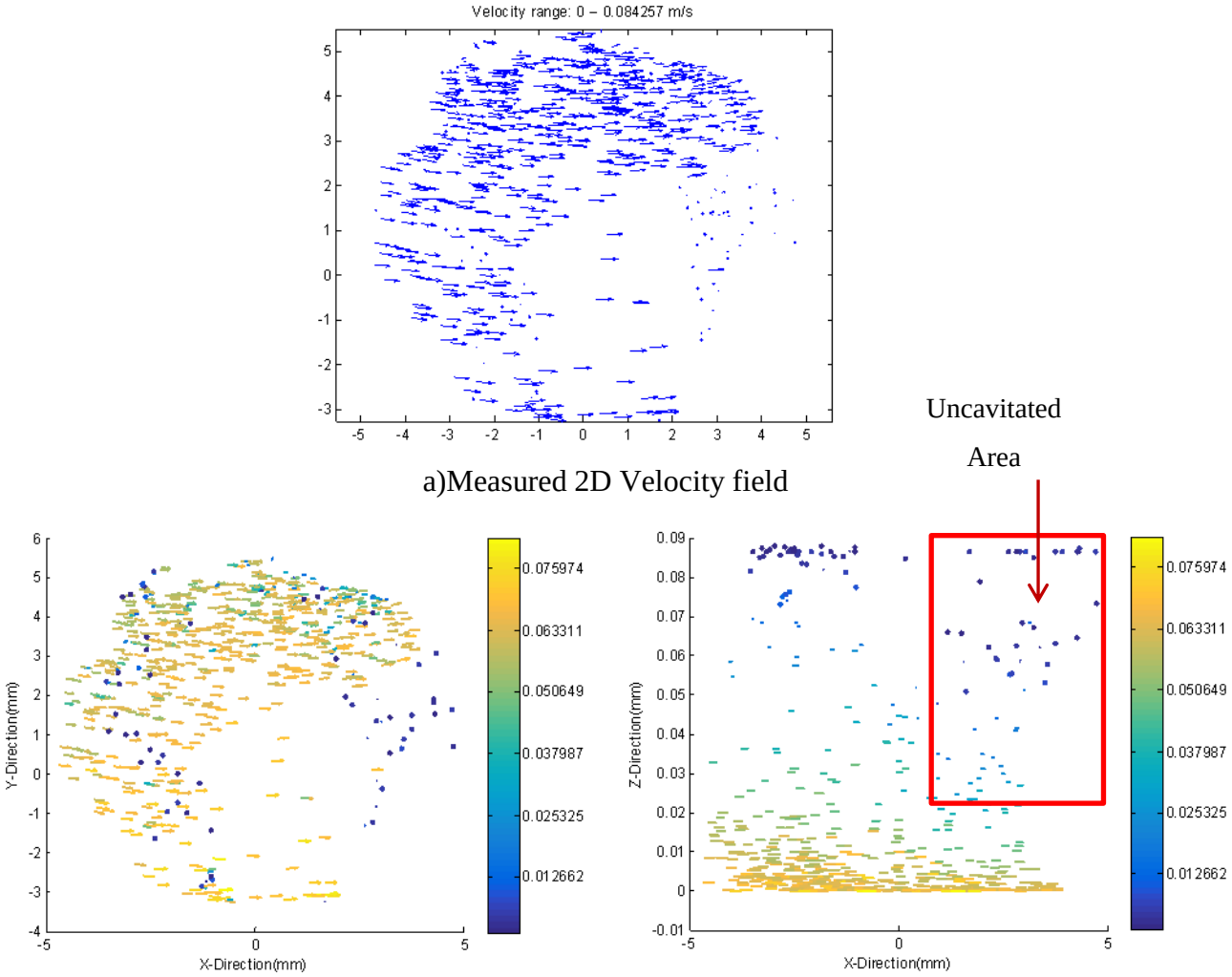

a)Measured 2D Velocity field

b) 3D Interpolated Velocities z-plane

c) 3D Interpolated Velocities y-plane

Figure 4.15: Velocity field from LDPIV η = 3.63 Pa-s, 20 RPM, 8 pocket

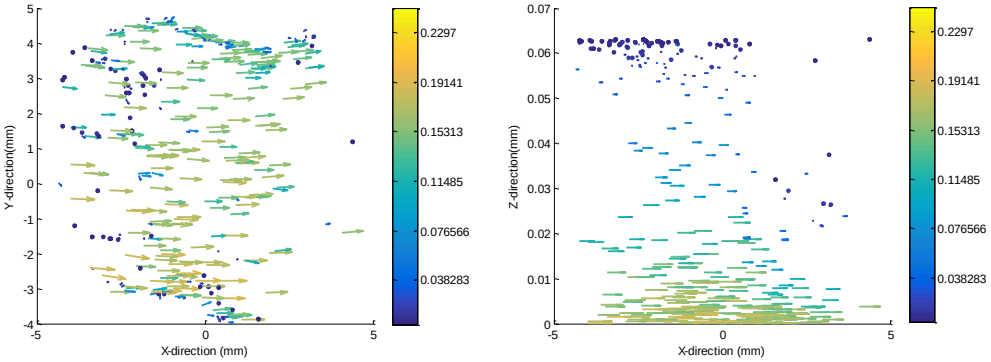

a) 50 RPM

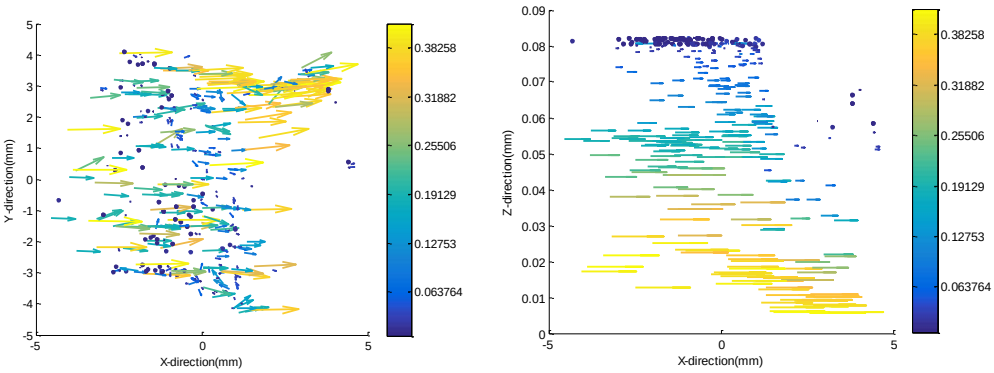

b) 150 RPM

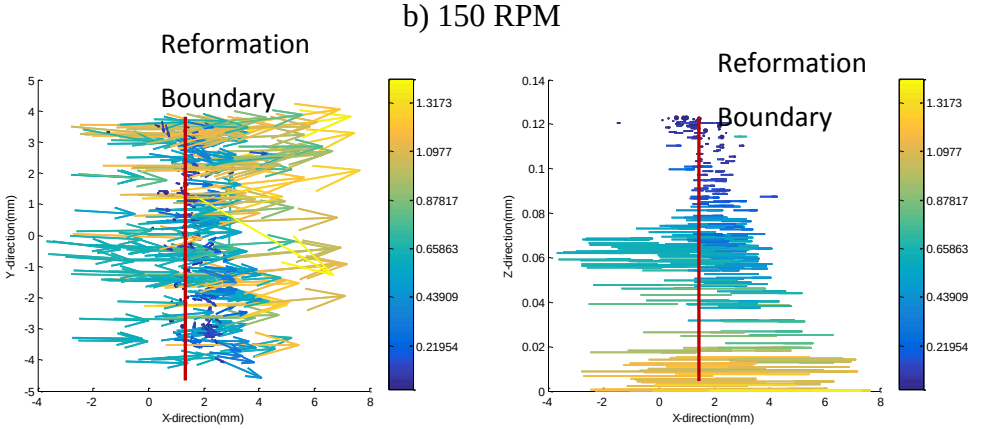

c) 350RPM

Figure 4.16: 3D interpolated Velocity fields at different speeds η = 0.755 Pa-s and 4 pocket

Figure 4.16 illustrates a comparison of the velocity fields at the different speeds. The results demonstrate that as the speed increased many of the particles agglomerate near the reformation boundary. This is due to the stronger recirculation effects that occur at higher operational speeds causing the particles move towards the reformation boundary more quickly. The 3D velocity fields also showed a significant number of particles very close to the rotating runner, demonstrating that much of the lubricant is passing over the pocket, while the lubricant inside of the pocket is trapped in a recirculation vortex

4.5 Conclusions

Pocketed thrust washers have been used in various applications as an effective way to support load, reduce wear between sliding conformal surfaces. In this study, an experimental test rig was designed and developed to investigate the effects of fluid flow inside of a pocketed thrust washer as a function of speed, lubricant viscosity, and load. BK7 glass and acrylic pocketed thrust washers were used to measure lubricant flow inside of a pocketed thrust bearing using μPIV. A high speed camera was used to capture video of the flow inside of a pocket. 10 to 15μm particles were introduced in three lubricants with viscosities of 3.63, 0.755, and 0.088 Pa-s. Flow visualization techniques such as μPIV were then employed to measure lubricant flow and cavitation areas at different operating conditions.

The experimentally measured cavitation areas showed a significant increase with an increase in speed. A slight increase in cavitation ratio was also observed with an increase in viscosity of the lubricant. The flow fields were measured using a non-uniform grid with an LDPIV method to allow for better tracking of the particle motion in the lubricant. The results showed that after the reformation boundary a recirculation flow occurred.

A numerical model was also developed to determine the pressure, film thickness, cavitation, and 3D fluid velocities with the thrust bearing. The cavitation areas obtained from the model were compared with the experimental results across all operating conditions. The results are within 5.81% of each other at speeds of 100 RPM and greater. Using the calculated velocities, the z-locations of the particles were determined through an interpolation method. With the interpreted z-locations, 3D velocity fields were generated using the experimental data. The 3D

velocities clearly show that the particles and in turn the lubricant, was trapped in a recirculation vortex after the reformation boundary inhibiting lubricant from leaving the pocket.

5. SURFACE MODIFICATION EFFECTS ON LUBRICANT TEMPERATURE AND FLOATING VALVE PLATE MOTION IN AN AXIAL PISTON PUMP

5.1 Introduction

The sliding tribological interfaces between pump components have been investigated to reduce wear and increase the overall life of axial piston pumps. Koc et al. [1992] presented the experimental and theoretical investigation of the geometric design of slippers as they slide along the swash plate in an axial piston pump. They showed that in order for the slippers to move smoothly, the slippers require a slightly convex surface on the slipper running surface. Mizell [2014] experimentally measured the friction force between the piston and cylinder block and compare the results with a numerical model. He illustrated that during the high pressure stroke of the piston the friction remains relatively stable and much lower than during the low pressure stroke of the piston.

The pressures at the interface between the cylinder block and valve plate can be subject to cavitation and wear. If the valve plate fails it can lead to complete failure of the axial piston pump. Ivantysynova et al.[2004], Invantysynova and Christiansen [2005], and Franco [1961] have studied the interface between the valve plate and cylinder block and how to reduce pressure pulsations and vibrations. These investigators focused on designing valve plate inlet and outlet ports based on a given optimized pressure profile at the cylinder block/valve plate interface which would reduce the vibration of the valve plate. Franco [1961] studied how to design feed grooves on the valve plate to reduce pressure pulsations of the pump using a force balance technique which accounts for the centrifugal force produced by rotary motion of the fluid.

It is important to note that two different types of valve plates are used in axial piston pumps, a fixed or floating valve plate. A floating valve plate is fixed in its rotation; however, it is free to move along the axial direction of the pump to develop a lubricating gap between the cylinder block, which is free to rotate but it is fixed in the axial direction. Balance pistons located behind the floating valve plate allow for axial motion to occur. A fixed valve plate is fixed in all directions of motion and affixed to the housing of the pump. The cylinder block for a fixed valve plate is free to rotate and move axially along the pump to create a lubricating gap. In

a fixed valve plate axial piston pump it is the motion of the cylinder block that creates a lubricating gap, whereas for a floating valve plate axial piston pump, the motion of the valve plate creates the lubricating gap. The aforementioned investigations have been performed with fixed valve plate axial piston pumps; this study has focused on the performance of a floating valve plate.

Many investigators have focused on measuring the lubricating gap between the cylinder block and valve plate. Kim et al. [2003] experimentally measured the film thickness of a fixed valve plate type axial piston pump during operation. The approach utilized non-contact proximity probes mounted on the cylinder block to measure the lubricant gap between the valve plate and the cylinder block. Richardson et al. [2017] experimentally measured the film thickness of a floating valve plate axial piston pump and explored how varying the operating conditions affected the film thickness. They observed similar trends to those of Kim et al. [2003], such as; if the speed increased so did the minimum film thickness. They also predicted floating valve plate motion by solving the equations of motion of a floating valve plate, which corroborated well with the experimental results. Bergada et al. [2011] also measured the lubricating gap of a fixed valve plate and explored the effects of temperature on the film thickness, showing that at higher temperatures there was a decrease in film thickness as well.

Wang et al. [2009], Etsion et al. [1999] and Ryk et al. [2002] have illustrated the efficacy of surface modifications, such as dimples and micro-channels to increase a bearings load carrying capacity and provide additional lubricant under starved conditions. In axial piston pumps, Chacon et al. [2014] developed a numerical model to investigate the effects of adding a wavy surface texture to the valve plate. An overall increase in the lubricant film was observed due to the surface modifications, as well as a significant reduction in temperature due to an increase in leakage flow at low pressure and low speed.

The objectives of this study were to experimentally measure the motion of the floating valve plate and analytically investigate the effects of surface modifications on film thickness and lubricant temperature. In order to achieve the experimental aspects of the investigation an axial piston pump test rig (APPTR) was used to measure the valve plate motion at various operating conditions. To achieve the analytical objectives a dynamic lubrication model described by Richardson et al. [2017] was augmented to account for temperature effects and elastic

deformation of the valve plate. Using a parametric study, the system stiffness and damping coefficients were determined. The overall system stiffness and damping coefficients were coupled with the dynamic lubrication model to predict lubricant temperature, pressure, film thickness and valve plate deformation at various operating conditions. The experimental and analytical motion of the valve plate were then corroborated and found to be in good agreement. Surface modifications, which utilized a 4 and 8-pocket design were then added to the floating valve plate in the dynamic lubrication model and the results were compared to the experimental measurements. This novel approach of adding surface modifications on a floating valve plate demonstrates effectiveness of the pockets on improving lubricant film thicknesses and decreasing lubricant temperatures.

5.2 Experimental Setup

The APPTR (which contains a 6 cc/rev pump) developed by Richardson et al. [2017] was instrumented with three proximity probes to measure the valve plate motion and lubricant film thickness. Tests were performed at operating conditions ranging between 800 psi (5.51 MPa) to 1200 psi (8.27 MPa) outlet pressure and a speed ranging from 600 to 1800 RPM. In order to ensure consistency across all experiments, a series of pressure transducers, thermocouples and heat exchangers were used to control the inlet pressure at a constant 120 psi (0.83 MPa), a constant case pressure of 100 psi (0.69Mpa) and an oil temperature at 35° C. Table 1 lists the test parameters used in this investigation. Figure 5.1 illustrates the assembled APPTR with various sensors and instrumentation.

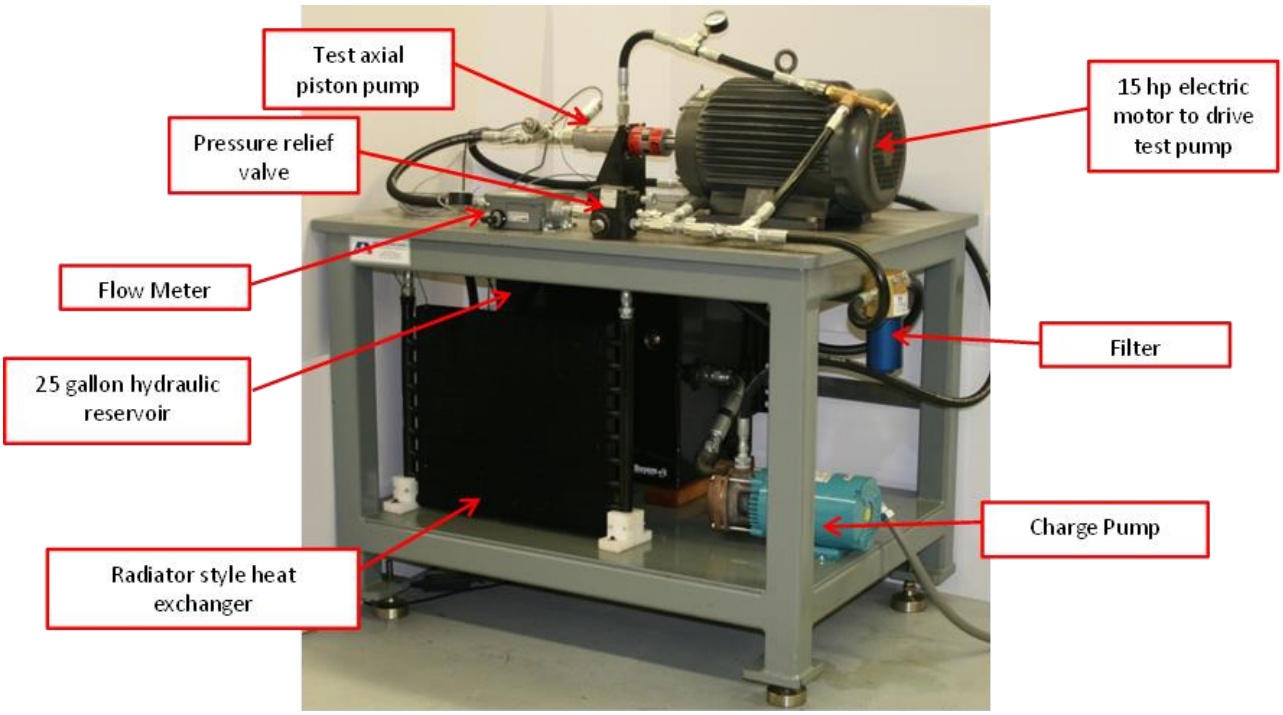

Figure 5.1: Constructed Axial Piston Pump Test Rig

Table 5.1: Test Parameters

Pump size(cc/rev)	6
Speed (RPM)	600,900,1200,1500,1800
Discharge Pressure (psi)	800,1000,1200
Discharge Pressure (MPa)	5.51,6.89,8.27
Oil used	0W-20
Oil Temp	35° ± 2° C
Oil Viscosity (Pa·s)	0.043

Ten film thickness measurements were performed at each operating condition. Due to the small size of the axial piston pump only three proximity probes could be accommodated. Richardson et al. [2017] describe how the results from three proximity probes are used to construct the motion and film thickness between the valve plate and cylinder block. The two main metrics used to assess the film thicknesses are minimum film thickness and Δfilm thickness, which is the difference between the minimum and maximum heights. The average minimum and Δfilm thicknesses for different operating conditions are shown in Figures 5.2 and 5.3. The results demonstrate that the minimum film thickness decreases and the Δfilm thickness increases

as the discharge pressure is increased. In addition, there is a slight increase in minimum film thickness as the speed is increased; however, speed has little effect on the Δfilm thickness. At every operating condition the location of minimum film thickness occurred on the inlet side of the valve plate at an angular position of 175-190°.

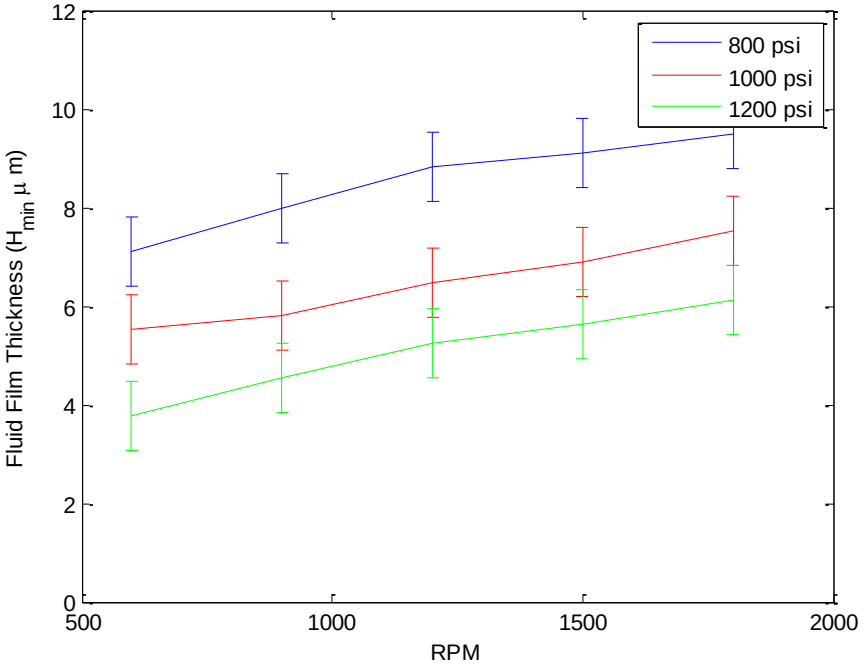

Figure 5.2: Average Minimum film thickness vs RPM and pressure

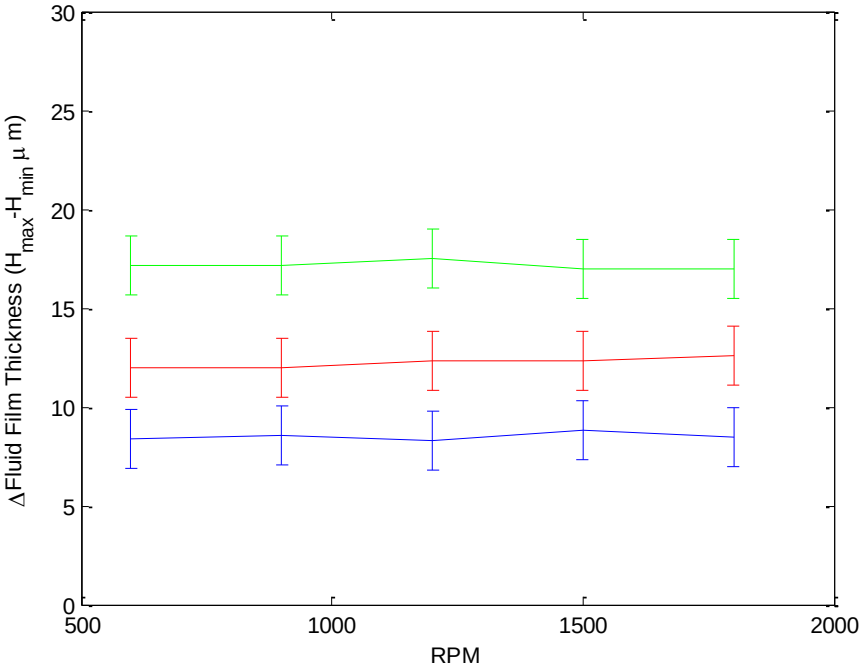

Figure 5.3: Average Δfilm thickness vs RPM and pressure

5.3 Dynamic Modeling

The numerical model developed in this investigation simulates the valve plate motion. The motion of the valve plate is what defines the lubricating gap and is defined with Zcm, θ, and φ. Zcm is the vertical motion of the valve plate from the center of mass, θ is the tilt angle from the x-axis, and φ is the tilt angle from the y-axis as shown in Figure 5.4. The balance pistons which support the valve plate are modeled as spring and dashpot systems. Summing forces about the valve plate center of mass will yield the equations of motion for a floating valve plate. Richardson et al. [10] defined the equations of motion for a floating valve plate and found that the balance pistons had a stiffness and damping of 8.72x107 N/m and 6.51x105 Ns/m respectively.

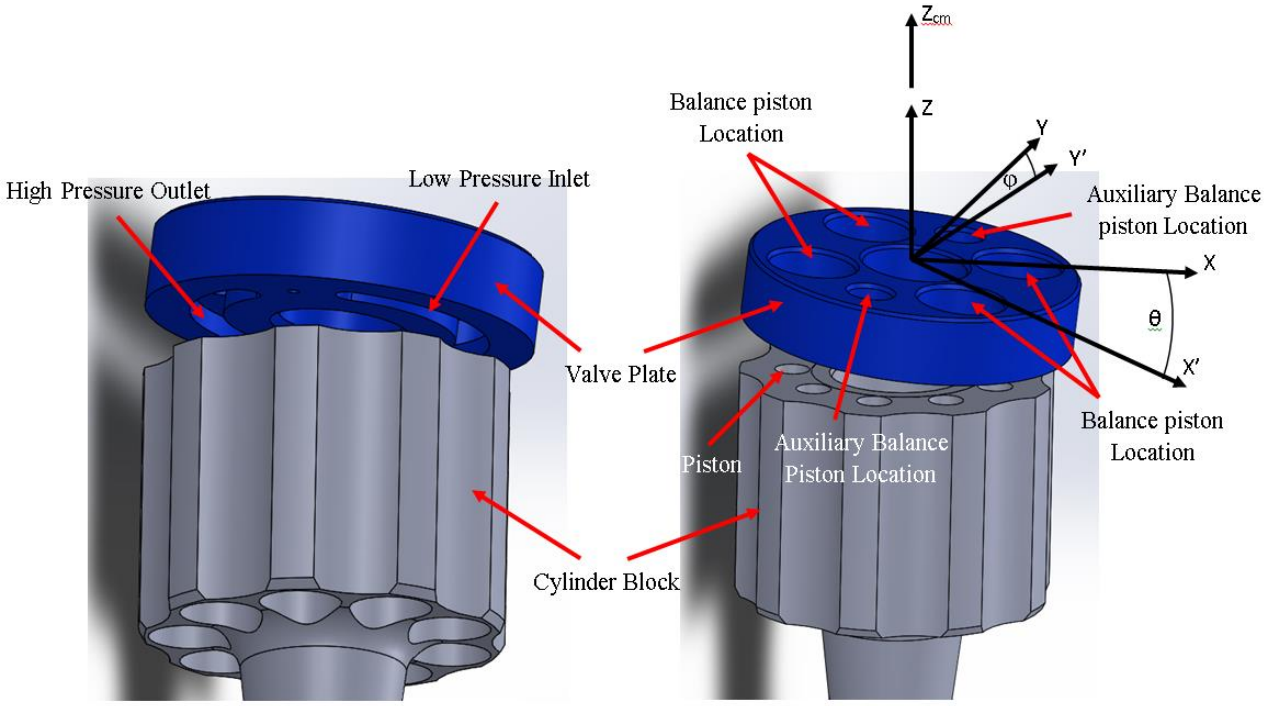

Figure 5.4: Floating Valve plate geometry with balance piston locations

The lubricant pressure is calculated using the Reynolds equation including the Elrod Cavitation algorithm and the JFO boundary condition [1981]. The numerical scheme developed by Vijayaraghavan and Keith [1989] was implemented in polar coordinates (Equation 5.1):

$$\frac{\partial}{\partial \bar{r}}\left(\frac{\bar{r}\beta\bar{h}^3F}{12\bar{\eta}}\frac{\partial\phi}{\partial\bar{r}}\right)+\frac{1}{\bar{r}}\frac{\partial}{\partial\theta}\left(\frac{\beta\bar{h}^3F}{12\bar{\eta}}\frac{\partial\phi}{\partial\theta}\right)=\frac{\bar{r}\omega}{2}\frac{\partial}{\partial\theta}\left(\bar{h}\phi\right)+\frac{\partial\bar{h}\phi}{\partial t} \tag{5.1}$$

$$\beta=\rho\frac{\partial\bar{P}}{\partial\rho}\therefore\bar{P}=P_c+\beta\ln\phi\quad where\quad\phi=\frac{\rho}{\rho_c} \tag{5.2}$$

F is the switching function used in Elrod's Cavitation Algorithm which deactivates parts of the Reynolds equation when the lubricant drops below the cavitation pressure.

$$F=\begin{cases}1\ for\ \phi>1\\0\ for\ \phi\le 1\end{cases} \tag{5.3}$$

Solving Equation 5.1 for F and ϕ the pressure of the lubricant is then given by Equation 5.4:

$$\bar{P} = \begin{cases} \bar{P} = P_c + \beta \ln \phi - P_a & for\ \phi > 1 \\ \bar{P} = P_c - P_a & for\ \phi \leq 1 \end{cases} \tag{5.4}$$

The inlet, outlet and instantaneous piston pressures, which occur at the valve plate/cylinder block interface are added as pressure boundary conditions to the Reynolds equation. Richardson et al. [2017] demonstrated how to calculate and implement the pressure boundary conditions.

Previous investigations of the floating valve plate performed by Richardson et al. [2017] have assumed isothermal conditions. However, investigations by Zecchi and Ivantysynova [2012] have shown that the lubricant temperature for a fixed valve plate can increase significantly at extreme operating conditions. For this reason, the lubricant temperature was calculated using a similar method described by Yu and Sadeghi [2002]. The temperatures are calculated in Equation 5.5 as a function of the flow velocities.

$$\rho C_f \left(\frac{\partial \bar{T}}{\partial \bar{t}} + V_r \frac{\partial \bar{T}}{\partial \bar{r}} + \frac{V_\theta}{\bar{r}} \frac{\partial \bar{T}}{\partial \theta} + V_z \frac{\partial \bar{T}}{\partial \bar{z}} \right) = k_f \left(\frac{1}{\bar{r}} \frac{\partial}{\partial \bar{r}} \left(\bar{r} \frac{\partial \bar{T}}{\partial \bar{r}} \right) + \frac{1}{\bar{r}^2} \frac{\partial^2 \bar{T}}{\partial \theta^2} + \frac{\partial^2 \bar{T}}{\partial \bar{z}^2} \right) + \eta \left[\left(\frac{\partial \bar{V_r}}{\partial \bar{z}} \right)^2 + \left(\frac{\partial \bar{V_\theta}}{\partial \bar{z}} \right)^2 \right] \tag{5.5}$$

The flow velocities are calculated using the pressure values from the Reynolds equation.

$$\bar{V}_\theta = \frac{\bar{z}(\bar{z} - \bar{h})}{2\bar{r}\bar{\eta}} \frac{\partial \bar{P}}{\partial \theta} + \frac{\bar{r}\omega\bar{z}}{\bar{h}}; \quad \bar{V}_r = \frac{\bar{z}\left(\bar{z} - \bar{h}\right)}{2\bar{\eta}} \frac{\partial \bar{P}}{\partial \bar{r}} \tag{5.6}$$

As the lubricant temperature is increased, the heat is transferred to the surrounding solids [2013]. The heat transfer between the second node in the solid and the second node in the fluid was calculated using Fourier's law and is illustrated in Equation 5.7.

$$\mathrm{q} = -\mathrm{kA} \frac{\partial \mathrm{T}}{\partial \mathrm{z}} \quad and \quad \frac{\mathrm{q}}{\mathrm{A}} = \frac{\mathrm{T}_{2_{\mathrm{FLUID}}} - \mathrm{T}_{2_{\mathrm{SOLID}}}}{\frac{\Delta \mathrm{z}_{\mathrm{FLUID}}}{\mathrm{k}_{\mathrm{FLUID}}} + \frac{\Delta \mathrm{z}_{\mathrm{SOLID}}}{\mathrm{k}_{\mathrm{SOLID}}}} \tag{5.7}$$

With the heat flux calculated, the temperatures at the fluid solid interface are calculated as follows:

$$\frac{q}{A} = k_{FLUID}\frac{T_{2_{FLUID}} - T_{1_{FLUID}}}{\Delta z_{FLUID}} = k_{SOLID}\frac{T_{2_{SOLID}} - T_{1_{SOLID}}}{\Delta z_{SOLID}} \tag{5.8}$$

On order to describe the temperature distribution in the valve plate and cylinder block a reduced form of the energy equation as described by Yu and Sadeghi [2002] was used. Equations 5.9 and 5.10 represent the energy equation for the valve plate and cylinder block respectively. Equation 5.10 has an additional term to include the effects of rotation on the cylinder block.

$$0 = k_{vp}\left(\frac{1}{\bar{r}}\frac{\partial}{\partial \bar{r}}\left(\bar{r}\frac{\partial \overline{T_{vp}}}{\partial \bar{r}}\right) + \frac{1}{\bar{r}^2}\frac{\partial^2 \overline{T_{vp}}}{\partial \theta^2} + \frac{\partial^2 \overline{T_{vp}}}{\partial \bar{z}^2}\right) \tag{5.9}$$

$$\rho C_{cb}\omega\frac{\partial \overline{T_{cb}}}{\partial \theta} = k_{cb}\left(\frac{1}{\bar{r}}\frac{\partial}{\partial \bar{r}}\left(\bar{r}\frac{\partial \overline{T_{cb}}}{\partial \bar{r}}\right) + \frac{1}{\bar{r}^2}\frac{\partial^2 \overline{T}_{cb}}{\partial \theta^2} + \frac{\partial^2 \overline{T_{cb}}}{\partial \bar{z}^2}\right) \tag{5.10}$$

When cavitation occurs in the lubricant, the heat transfer to the surrounding solids will be affected. Boncompain et al. [1986] have suggested that in fully cavitated regions the thermal conductivity of the lubricant is reduced to that of air. Therefore, in any cavitated region the thermal conductivity of the lubricant was reduced to that of air when calculating the energy flow "q" in Equation 5.9. The model does not account for the specific properties of the gas released.

The Roelands' viscosity model [1986] was used to account for the lubricant viscosity variation with respect to temperature.

$$\log\left(\log(1000\,\bar{\eta}) + 1.20\right) = -S_0 \log\left[1 + \frac{\overline{T} - 273.15}{135.0}\right] + \log G_0 \tag{5.12}$$

The constants S_0 and G_0 were calibrated from experimental measurements which are shown in Figure 5.5. The above equation matches the experimental data with a confidence level $R^2 = 0.9994$.

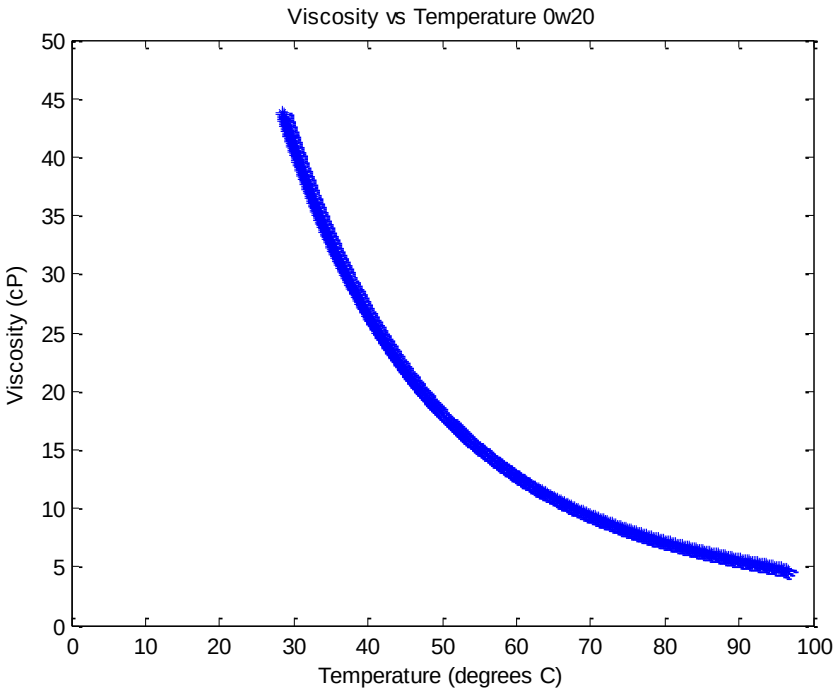

Figure 5.5: Temperature Viscosity Relationship for 0w20

Lubricant pressure is often the main source of deformation of the valve plate [15]. Because the fluid at the discharge port was kept at 35oC and the thickness of the floating valve plate is 11 mm, deformations due to thermal effects were assumed to be negligible. Therefore, lubricant pressure was assumed to be the dominating cause of valve plate deformation and thermal deformations were neglected. The elastic deformation due to pressure was calculated using the influence matrices as described by Zecchi and Ivantysynova [15]. In this approach, the floating valve plate geometry is imported into ABAQUS and meshed using tetrahedron linear elements as illustrated in Figure 5.6. Figure 5.7 depicts the deformation of the valve plate due to the reference pressure acting over a single differential area on the surface of the valve plate. The backside of the valve plate was fixed along the direction of the applied load. The resulting deformation of the valve plate surface is stored in an influence matrix and can be scaled to represent any pressure acting over that area assuming linear elastic behavior. The process is then repeated for every differential area of the floating valve plate. The total deformation of the valve plate is then calculated by applying the principle of superposition, where the elastic deformation

from each differential pressure can be summed to represent the total deformation as shown in Equation 5.13.

$$u_{total} = \sum_{i=1}^{n} \frac{p_i}{p_{ref}} * IM_i \tag{5.13}$$

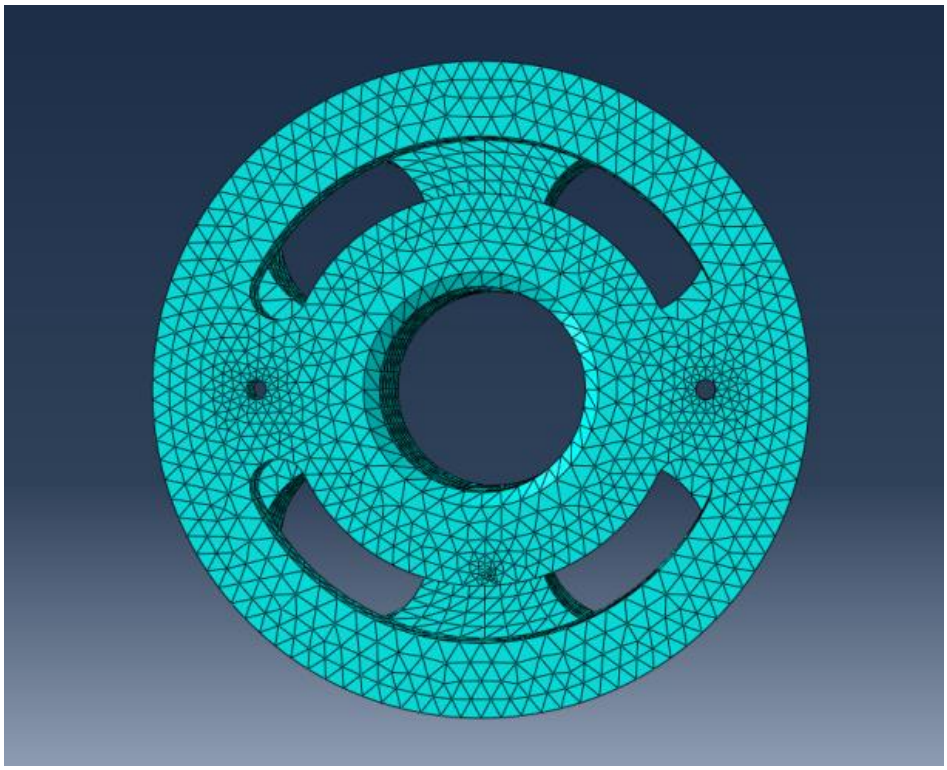

Figure 5.6: ABAQUS Mesh of floating Valve Plate

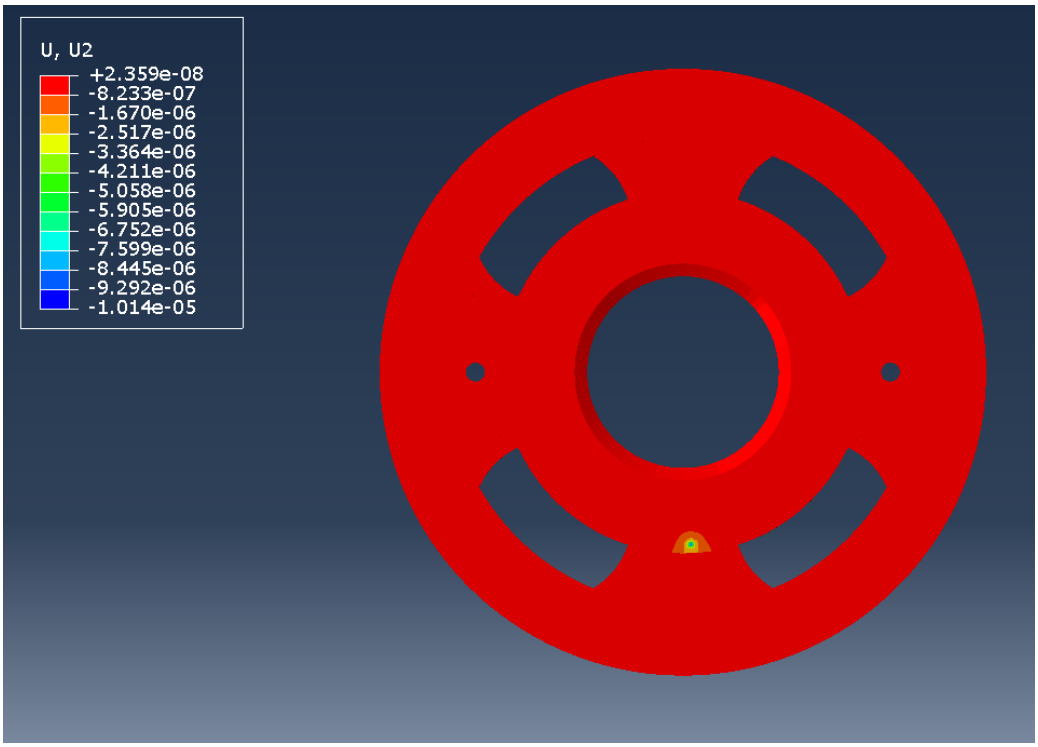

Figure 5.7: Floating valve plate displacement due to the reference pressure

A Gauss-Seidel Newton-Raphson scheme was used to solve the system governing equations (5.1-5.11). As part of the temperature boundary conditions, the fluid located at the inlet and outlet ports of the pump were held at the experimentally measured temperatures of 34° C (307.15 K) and 35.5° C (308.65 K) respectively. Additionally, convective boundary conditions are applied at the inner and outer radius to describe the fully flooded condition of the valve plate. The convective boundary conditions are given by Equation 14. The discretized form of the Reynolds and energy equations with a detailed description of the appropriate boundary conditions are given by Cross et al. [12] and Yu and Sadeghi [14]

$$\frac{\partial T_{vp}}{\partial r} = H_P\left(T_{vp} - 1\right) \; at \; the \; inner \; radius; \quad \frac{\partial T_{vp}}{\partial r} = -H_P\left(T_{vp} - 1\right) \; at \; the \; outer \; radius \qquad (5.14)$$

$$H_P = \frac{k_{vp}}{h_{FLUID} r dr R_O}$$

A nodal resolution of 300 nodes in the tangential and 100 nodes radial directions produced accurate results for the lubricant pressures, temperatures, and deformation of the valve plate.

Additionally, a nodal resolution of 20 nodes was used across the fluid film to solve for the 3D temperature profiles of the lubricant.

Figure 5.8 displays a flow chart of the model developed for this investigation. After initializing the matrices, the pressure and cavitation are obtained from the solution to the thermal Reynolds equation. The valve plate deformation is then calculated using the lubricant pressure. The lubricant pressure is recalculated with the deformation of the valve plate added to the film thickness. The process is repeated until the valve plate deformation has converged. The energy equation is used to determine the temperature distribution in the lubricant, cylinder block and valve plate using the flow velocities calculated from the pressure field. The equations of motion for the valve plate are then used to determine the film thickness at the next time step. The dynamic lubrication model developed in this investigation was used to simulate for the same operating conditions as the experiments. The time step was set to 1 millisecond and was simulated for a total of 1000 steps or 1 second. Table 2 contains the simulation parameters used for this model.

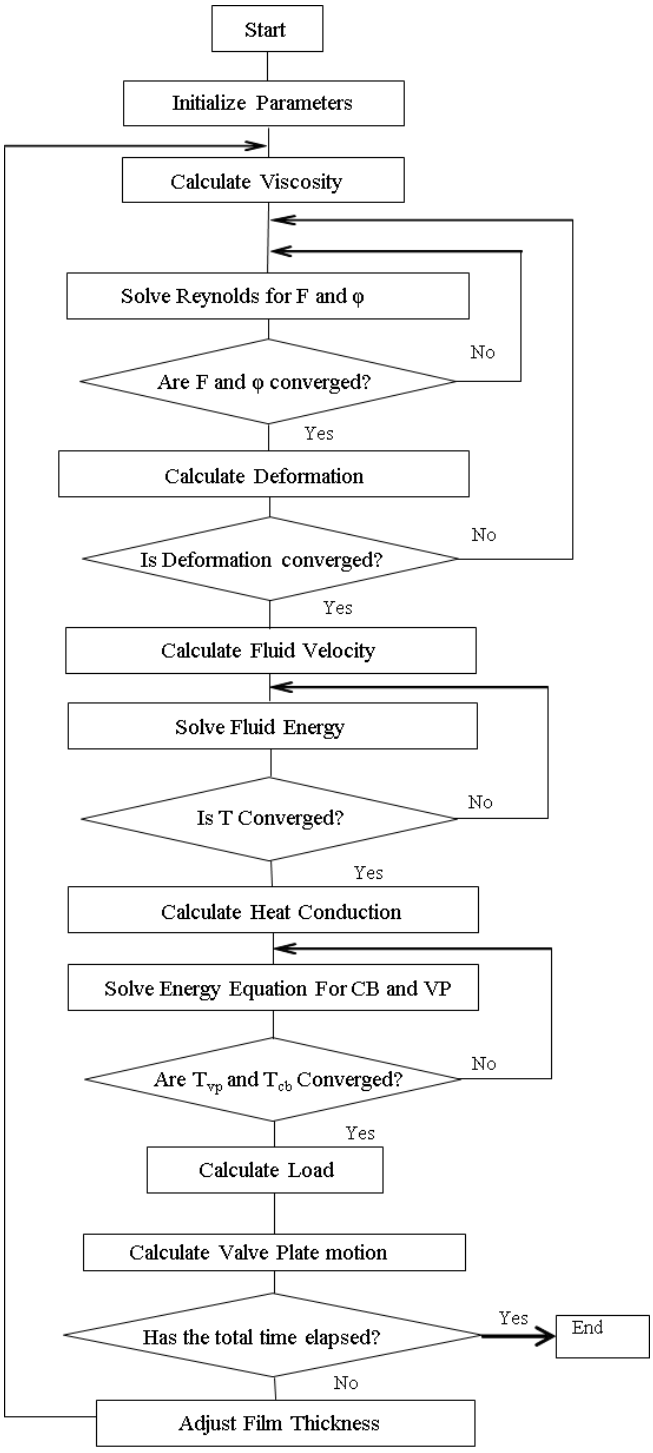

Figure 5.8: Flow Chart for the Solution Procedure

Table 5.2: Simulation Parameters

Oil Viscosity	Roelands' Model
S_0 (Roelands' Model)	1.173
G_0 (Roelands' Model)	2.743
Valve Plate Thickness	10.1 mm
Cylinder Block Thickness	31.2 mm
Fluid Specific Heat	1966 J/kgK
Cylinder Block Specific Heat	600 J/kgK
Cylinder Block Thermal Conductivity	46.7 W/mK
Valve Plate Thermal Conductivity	46.7 W/mK
Fluid Conductivity	0.14 W/mK
Fluid Convection Coefficient	100 W/m^2K
Cylinder Block Density	7840 kg/m^3
Valve Plate Density	7840 kg/m^3
Fluid Density	881.9 kg/m^3
Fluid Bulk Modulus	1.5 GPa
Atmospheric Pressure	101325 Pa
Cavitation Pressure	90000 Pa
Initial Temperature	34ºC

5.4 Dynamic Lubrication Model Results

Using the parametric study approach described by Richardson et al. [2017] the stiffness and damping coefficients of the valve plate system were found to be 7.23x107 N/m and 6.95x105 Ns/m respectively. The spring and damping coefficients were then used in the dynamic lubrication model and the film thicknesses were then calculated. Figures 5.9 and 5.10 depict the minimum and Δfilm thicknesses from the model compared to the experimental results, and demonstrate excellent correlation between the experiments and the dynamic model. The same film thickness trends observed in the experiments were also observed with the numerical model, such as an increase in speed increased minimum film thickness and an increase in pressure increased the Δfilm thickness. Additionally, the calculated Δfilm thicknesses stay well within the error bounds of the experiments for all operating conditions and the calculated minimum film thicknesses are at most 1.1% outside of the error bounds of the experiments. Figure 5.11 illustrates the calculated film thickness at 1200 psi (8.27 MPa) and 1800 rpm depicting that the valve plate operates at an angle relative to the motion of the cylinder block.

Figure 5.11 also illustrates that the model predicted the location of the minimum film thickness occurs on the inlet side of the valve plate at an angular position of 183°.

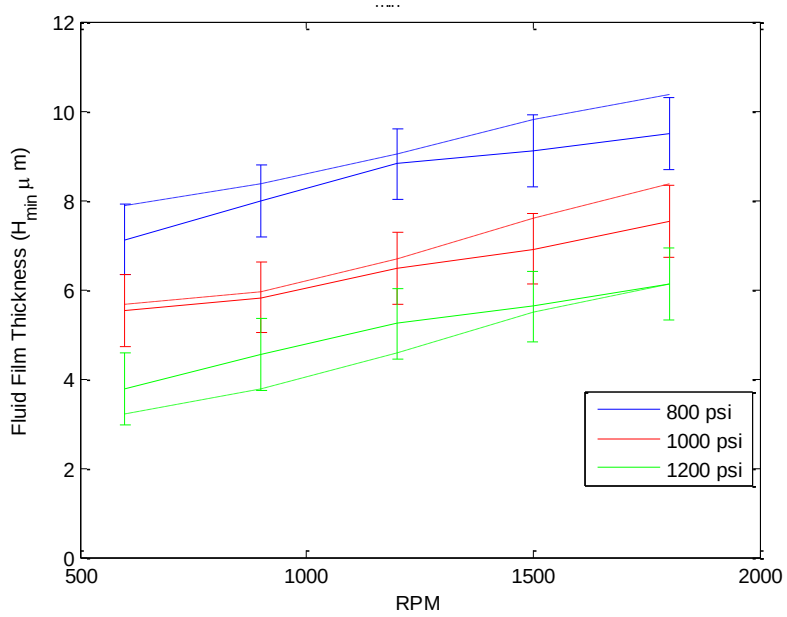

Figure 5.9: Hmin vs Operating Conditions using New Stiffness and Damping Coefficients

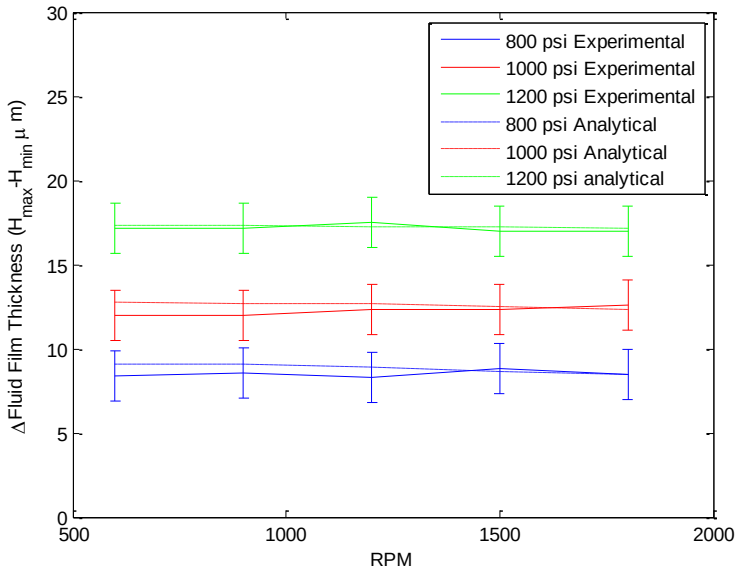

Figure 5.10: ΔFluid Film Thickness vs Operating Conditions using New Stiffness and Damping Coefficients

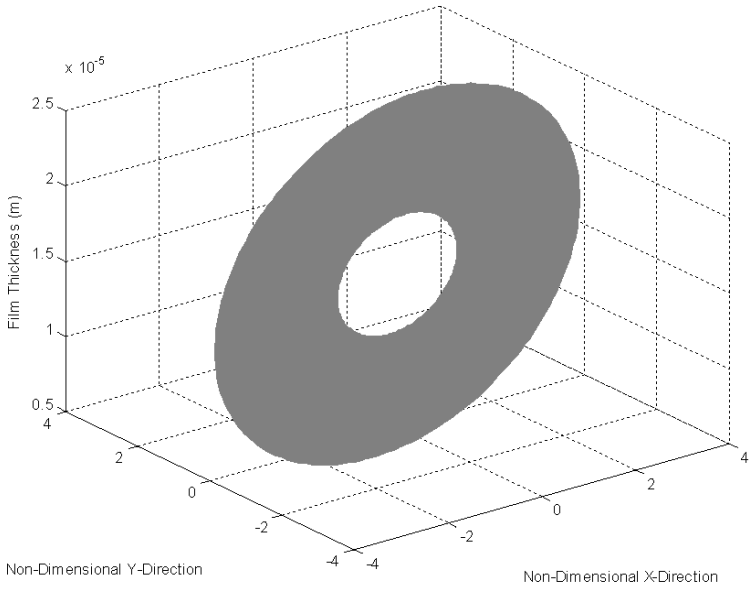

Figure 5.11: Film Thickness of Valve plate at 1200 psi (8.27MPa) and 1800 rpm

The lubricant temperature variation at 1200 psi (8.27 MPa) and 1500 rpm is shown in Figure 5.12. The lubricant begins at a constant temperature of 34° C (307.15 K) and is shown to increase as a function of time. Figure 5.12 demonstrates that after 0.4 seconds the lubricant reached a steady state temperature. For every operating condition the lubricant was found to reach steady state temperature at approximately 400 time steps, or at 0.4 seconds. When comparing the temperatures at the different operating conditions, only the steady state temperatures were considered. The maximum temperature of the lubricant always occurred at the location of minimum film thickness. At this location, the velocity gradient reaches a maximum. Because the velocity gradient is directly related to the viscous shear by lubricant viscosity, the maximum shear also occurs at the location of minimum film thickness resulting in an increase in lubricant temperature. Figure 5.13 shows the temperature at the location of minimum film thickness for different operating conditions. Speed greatly affects the temperature of the lubricant causing the temperature to rise from 39.65°C (312.8 K) at 600 rpm to 46.65°C (319.8 K) at 1800 rpm for the case of 1200 psi (8.27 MPa). The increase in discharge pressure results in an increase in the lubricant temperature as well. By reducing the outlet pressure from 1200 psi (8.27 MPa) to 1000 psi (6.89 MPa) an average 1.7°C reduction is observed at the location of minimum film thickness.

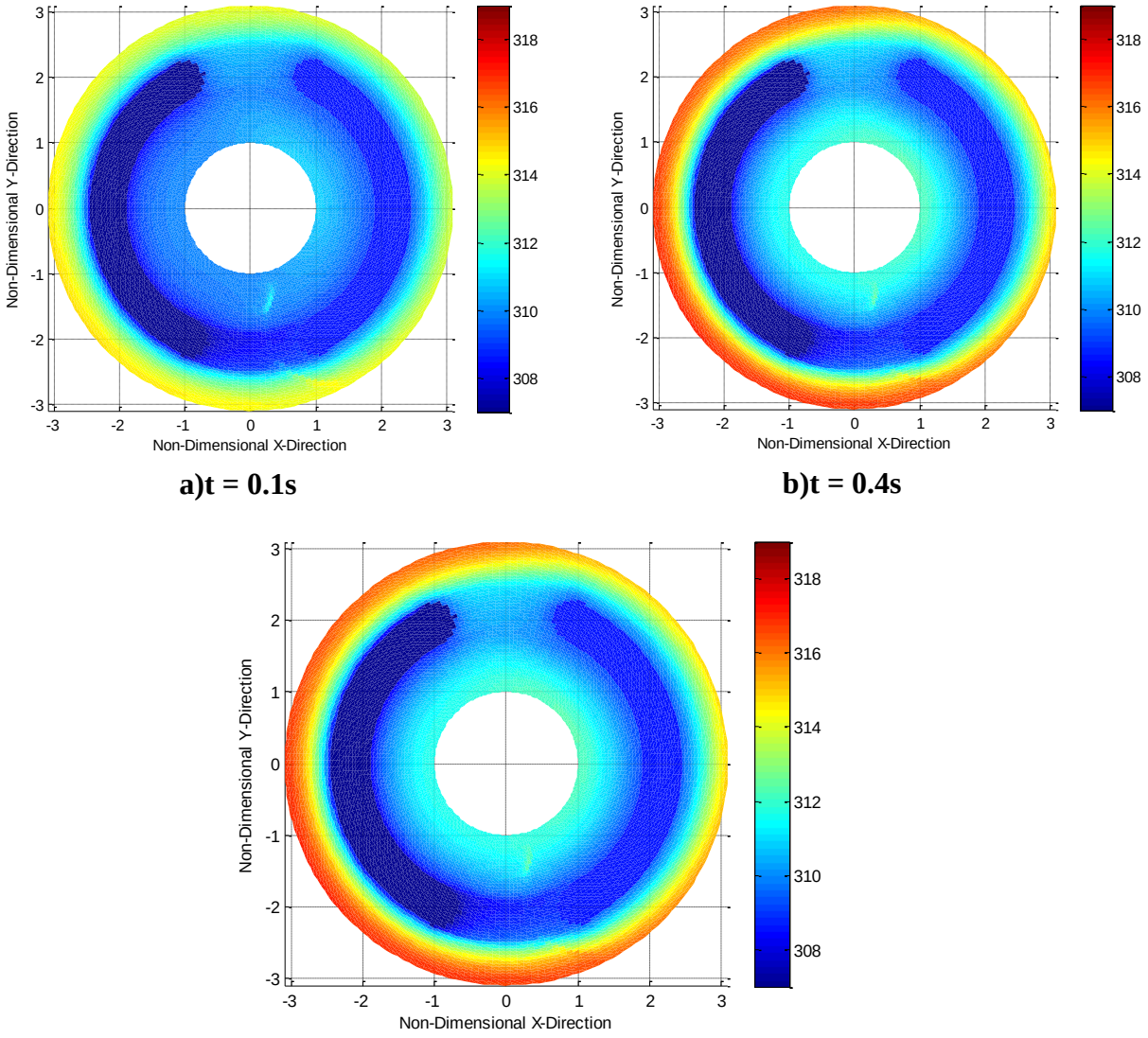

Figure 5.12: Lubricant Temperature in Kelvin at 1200 psi (8.27MPa), 1500 rpm, z = 0.5h

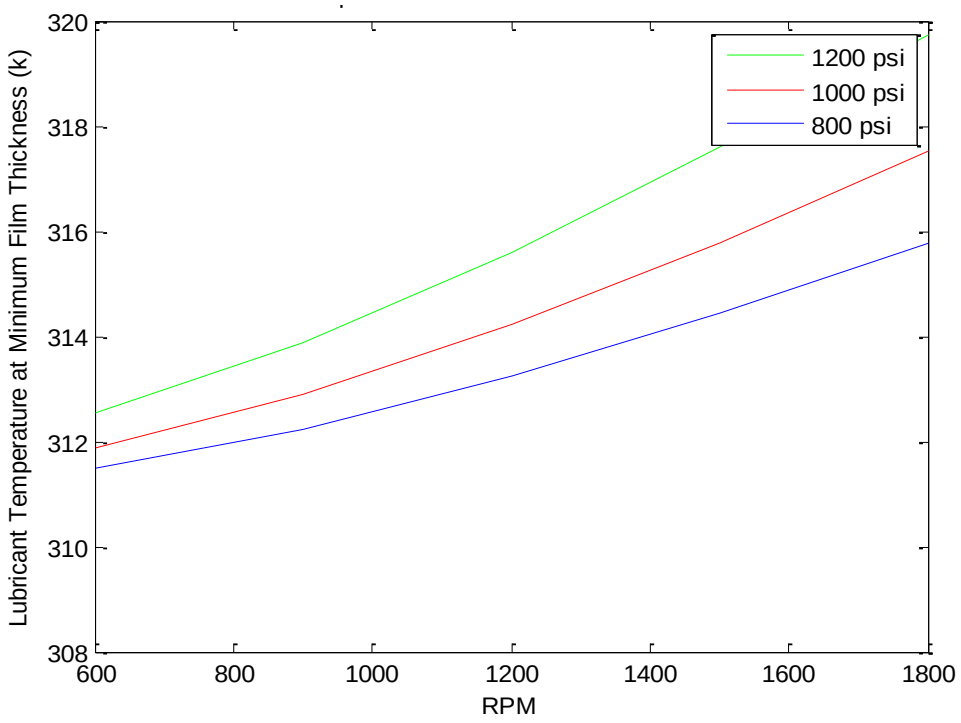

Figure 5.13: Lubricant Temperature at Location of Minimum Film Thickness vs. Operating Conditions

The calculated pressure profiles are similar to the ones described by Richardson et al. [2017]. Figure 5.14 shows the pressure profile of the lubricant for the case of 1200 psi (8.27 MPa) at 1800 rpm and illustrates how the inlet and outlet pressures dominate the lubricant pressure. Also observed was the pressure spike and drop at the location of minimum film thickness due to the converging and diverging geometry. For the case demonstrated in Figure 5.13, the pressure rose to 185 psi (1.28 MPa) and then decreased to 55 psi (0.39 MPa). Cavitation was never observed at any of the operating conditions used in the model.

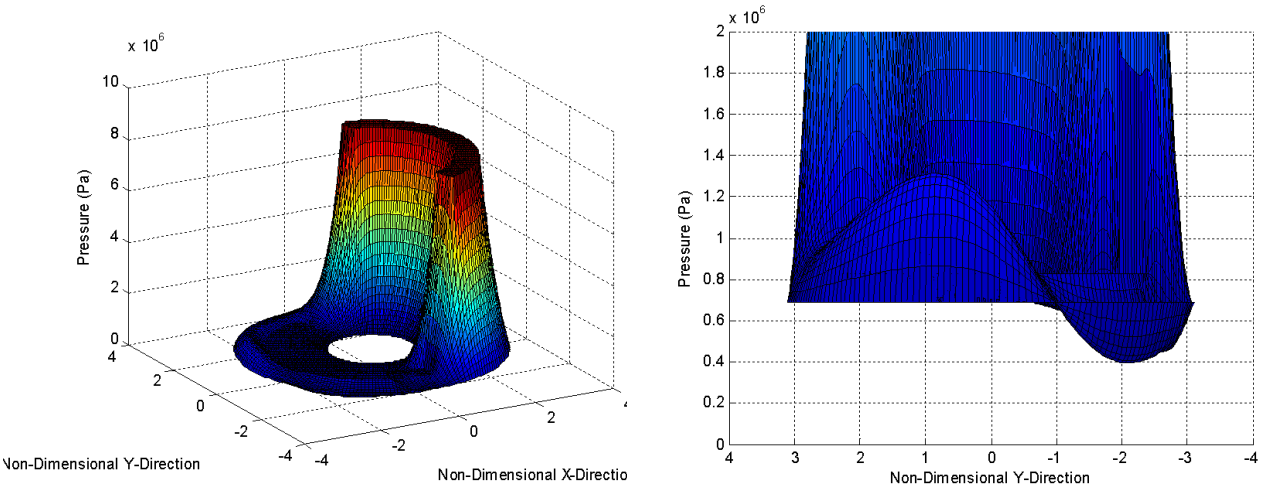

Figure 5.14: Lubricant Pressure at 1200 psi (8.27MPa) and 1800 rpm

Figure 5.15 shows the elastic deformation of the valve plate at the most extreme operating condition of 1200 psi (8.27 MPa) and 1800 rpm. The maximum deflection was 0.243 µm and was observed around the high pressure outlet. The film thickness along the high pressure outlet is 20.2 µm which indicates that the deformation of the valve plate constitutes 1.2% of the overall film thickness at that location. Along the low pressure inlet, the valve plate deformation constitutes 0.7% of the film thickness. Similar comparisons were observed across all operating conditions, thus the valve plate can be assumed to behave rigidly, which validates the experimental assumption of rigid body dynamics. The reasons for such small elastic deformations are due to the operating pressures used in the experiments and model being relatively low and the uniqueness of the floating valve plate system. A floating valve plate can be up to twice as thick as a fixed valve plate in a similarly sized pump.

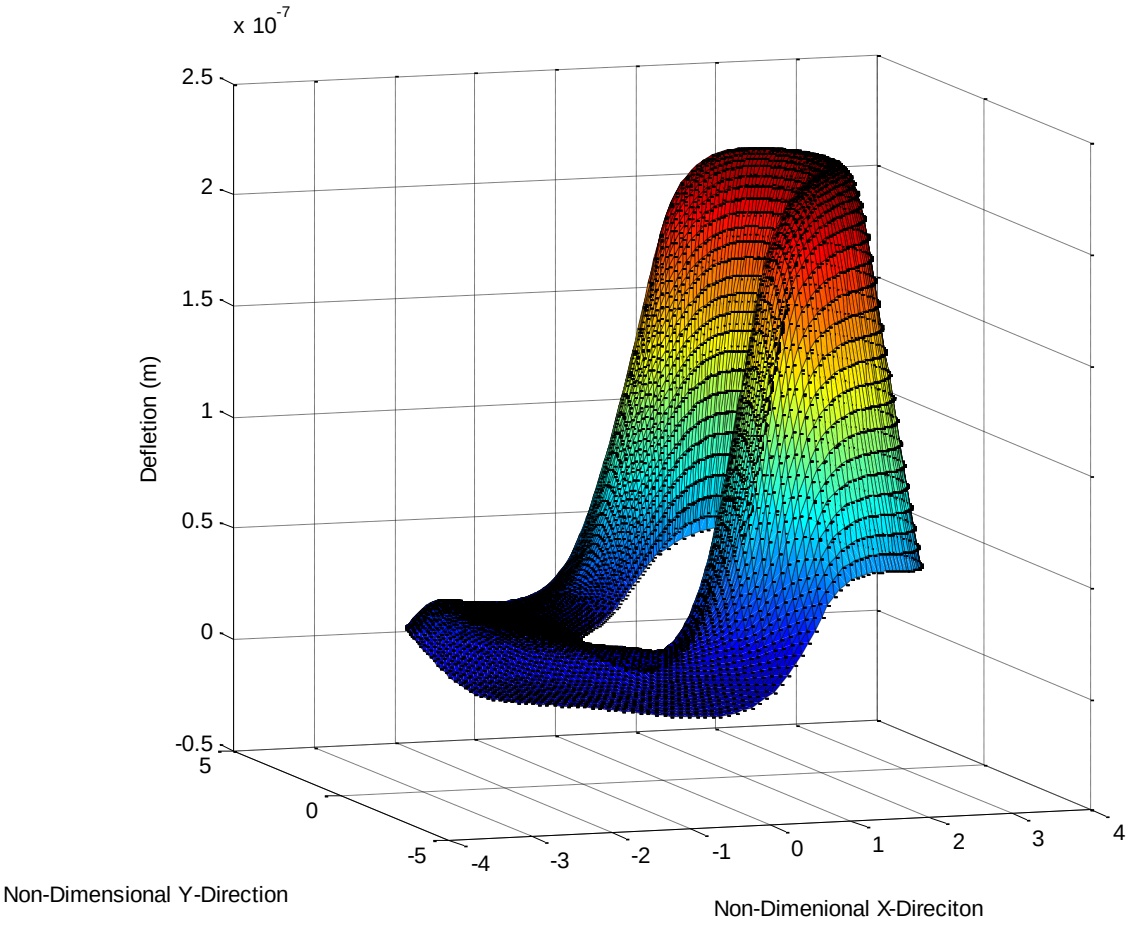

Figure 5.15: Elastic Deformation of Valve Plate due to Lubricant Pressure at 1800 rpm and 1200 psi (8.27MPa)

5.5 Surface Modification Results

Richardson et al. [2018] measured the lubricant flow in and out 4 and 8-pocket thrust bearings and compared the results with a numerical model that calculated lubricant pressures, flow, and film thicknesses. The investigation illustrated the efficacy of this type of pocketed geometry and design in generating a lubricant film thickness and providing lubricant to the bearing surfaces. Because the valve plate/cylinder block system is similarly loaded system to the thrust bearings, 4 and 8-pocket designs were used as surface modifications on floating the valve plate. Figure 5.16 illustrates the valve plate geometry with the added 4 and 8-pocket designs; the added pockets are 2.5 mm in diameter with a depth of 20 µm. The diameter of the pockets was governed by the geometry of the valve plate, in that the 2.5 mm was the maximum allowable

distance between the inlet or outlet port and the edge of the valve plate. Vaidya and Sadeghi [2009] demonstrated that the widest and shallowest pockets yield the best results for pressure generation and load carrying capacity, thus a 20 µm pocket depth was selected for this investigation.

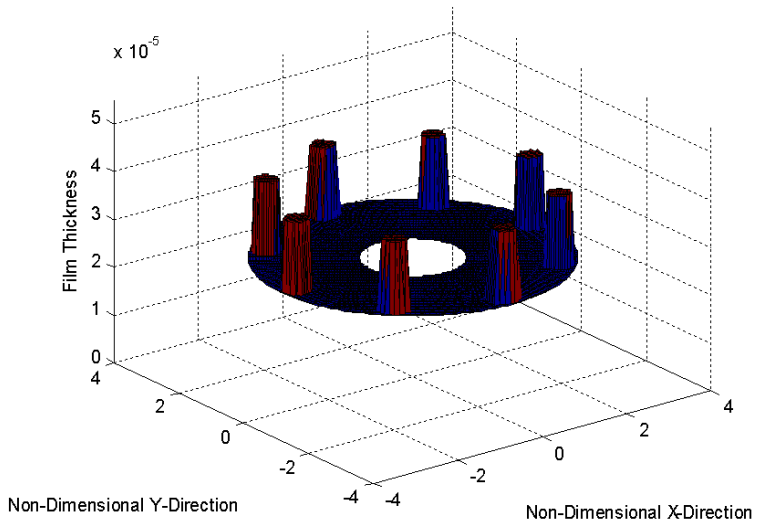

a) 8-pocket Design

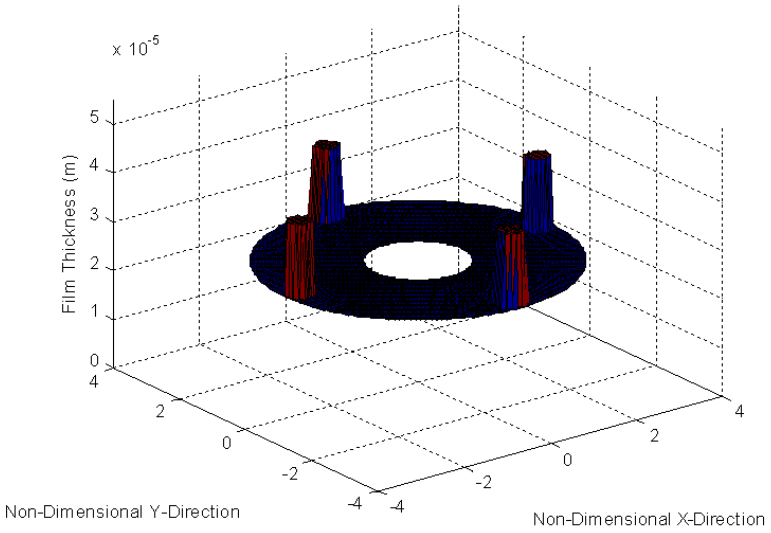

b) 4-pocket Design

Figure 5.16: 4 and 8-Pocket Designs for Floating Valve Plate

Figure 5.17 demonstrates the lubricant pressure profiles for a surface modified valve plate at 1200 psi (8.27 MPa) and 1800 rpm. Due to the rapid converging and diverging geometries of the pockets, pressure spikes as well as cavitation areas occurred at the pocket locations. The type of cavitation induced at these locations is gaseous cavitation and has been observed by Cross et al. [2015] and Yu and Sadeghi [2002] using similar geometries. The pressure generated due to the converging geometry of the pockets is shown to be much higher than the converging geometry of a standard valve plate. As previously discussed, at 1200 psi (8.27 MPa) and 1800 rpm the lubricant for a standard valve plate builds up to 185 psi (1.28 MPa) at the location of minimum film thickness, whereas the 4 and 8-pocket designs generate 427 psi (2.95 MPa) and 415 psi (2.85 MPa) respectively at the location of minimum film thickness.

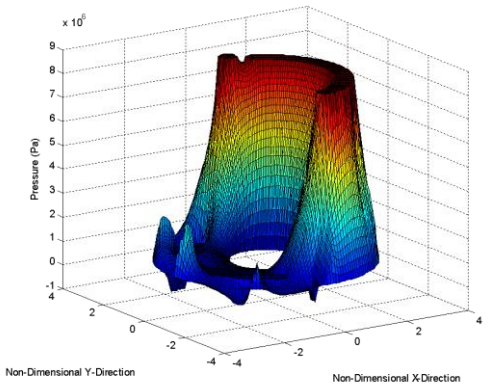

a) 8-pocket

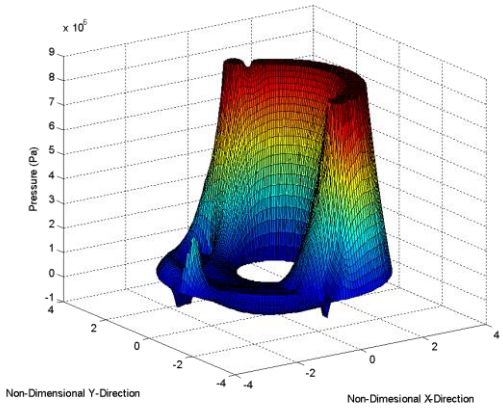

b) 4-pocket

Figure 5.17: Lubricant pressures with surface modifications at 1200 psi (8.27MPa) and 1800 rpm

Figures 5.18 and 5.19 illustrate the minimum and Δfilm thicknesses of the 4 and 8-pocket designs compared to the measured values across the various operating conditions. The minimum film thickness showed a significant increase with both a 4 and 8-pocket design. For example, at an operating condition of 1200 psi (8.27 MPa) the 4 and 8-pocket designs showed an average increase in minimum film thickness of 0.81 μm and 1.12 μm respectively when compared to the average experimental values. Larger increases in minimum film thickness were observed at lower operating pressures. The calculated Δfilm thicknesses stay within the error bounds of the experimental values. However, a slight decrease in Δfilm thickness was observed with an increase in RPM. For example, at an operating condition of 1000 psi (6.89 MPa) with an 8-pocket design the Δfilm thickness decreases by 1.21 μm when increasing the speed from 600 rpm to 1800 rpm. The decrease in Δfilm thickness occurs because as the speed is increased, the pressure generated from the pockets near the location of minimum film thickness increases greatly whereas the pressure generated near the location of maximum film thickness shows no significant increase. It should be noted that just as with the previous cases for the floating valve plate, the minimum film thickness calculated for the 4 and 8-pocket design occurred on the inlet side of the valve plate at an angular position of 175-190°. The maximum deformation calculated for the 4 and 8-pocket designs was 0.244 μm, which again confirms that the valve plate will behave as a rigid body for the operating conditions tested.

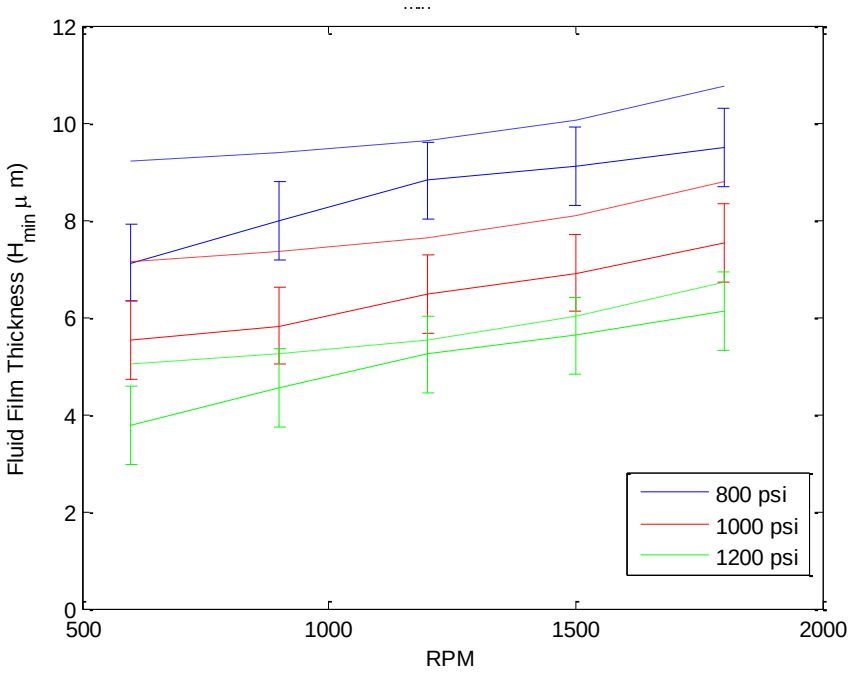

a) Minimum Film Thickness

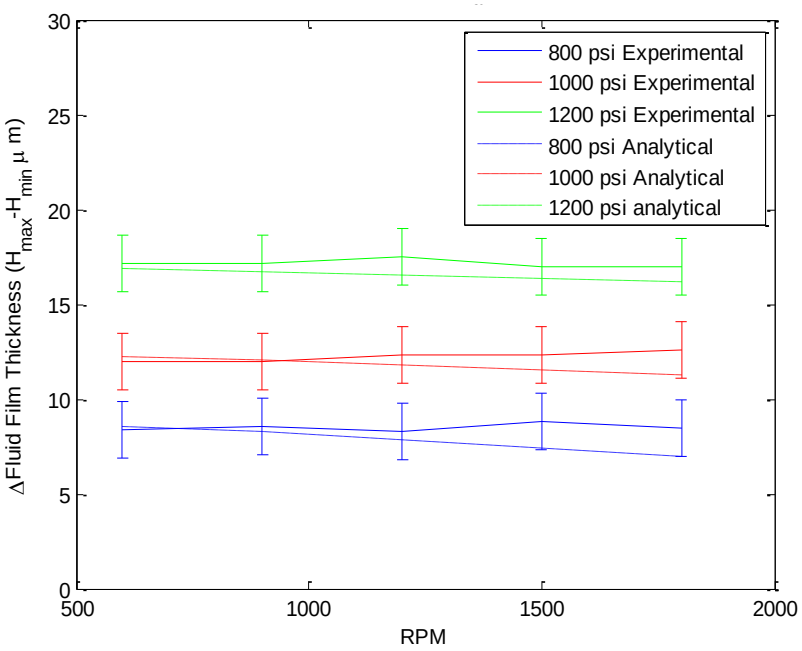

b) ΔFilm Thickness

Figure 5.18: Minimum and ΔFluid Film Thickness vs Operating conditions for a 4-Pocket design

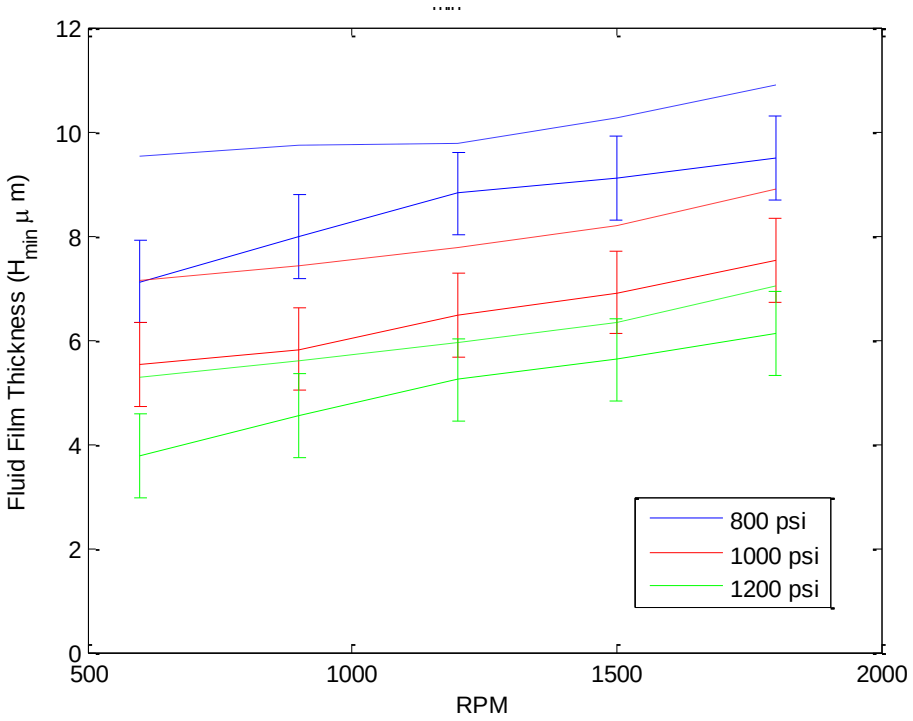

a) Minimum Film Thickness

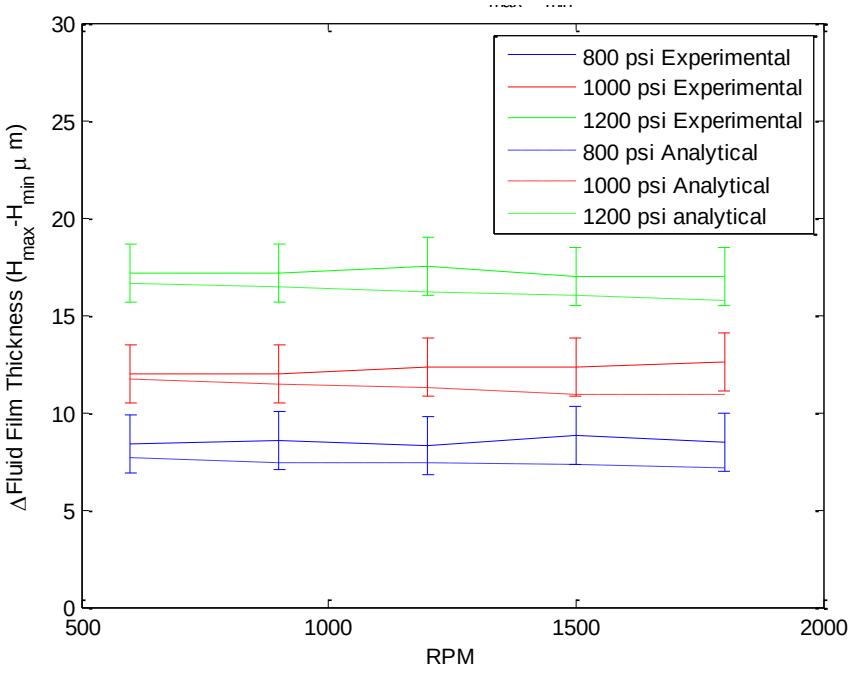

b) ΔFilm Thickness

Figure 5.19: Minimum and ΔFluid Film Thickness vs Operating conditions for an 8-Pocket design

Due to the change in the lubricant pressures and film thickness the resulting lubricant temperatures vary from a standard unmodified valve plate design. Figure 5.20 illustrates how the added pockets affect the lubricant temperature as a direct result of the cavitation and lubricant pressure build up that occurs. A slight temperature drop and sharp temperature increase is observed at the pocket locations. The increase in temperature at the pockets can even at times exceed the temperature at the location of minimum film thickness where the viscous shear is at a maximum. The rapid change in pressures at the pocket locations is what induces such a temperature change. Figure 5.20 also demonstrates that similar to a standard valve plate design the lubricant temperature reaches a local maximum at the location of minimum film thickness. Figure 5.21 illustrates the lubricant temperature at the location of minimum film thickness across the various operating conditions for a 4 and 8-pocket design. Just as with a standard unmodified floating valve plate design speed significantly increased the temperature of the lubricant and an increase in operating pressure results in higher lubricant temperatures. A reduction in temperature is observed with the surface modified valve plate when compared to the standard floating valve plate design. For the case of 1200 psi (8.27 MPa) and 1800 rpm the 4 and 8-pocket designs yielded a 2.54° C and 3.36° C reduction in temperature. The reduction of temperature can result in an increase of viscosity of up to 13.2%, which yields higher lubricant pressures and thicker film thicknesses. At lower speeds the reduction in temperature for the 4 and 8-pocket designs is not as significant yielding only a 1.79 ° C and 2.48° C reduction at 1200 psi (8.27 MPa) and 600 rpm.

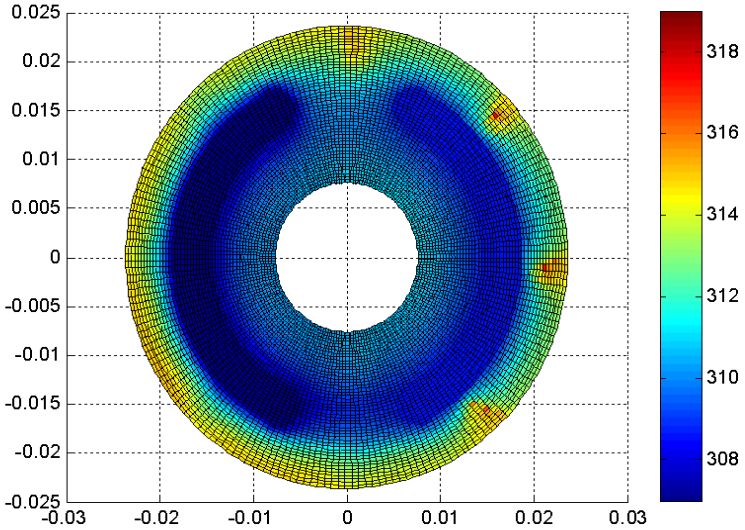

a) 8-pocket

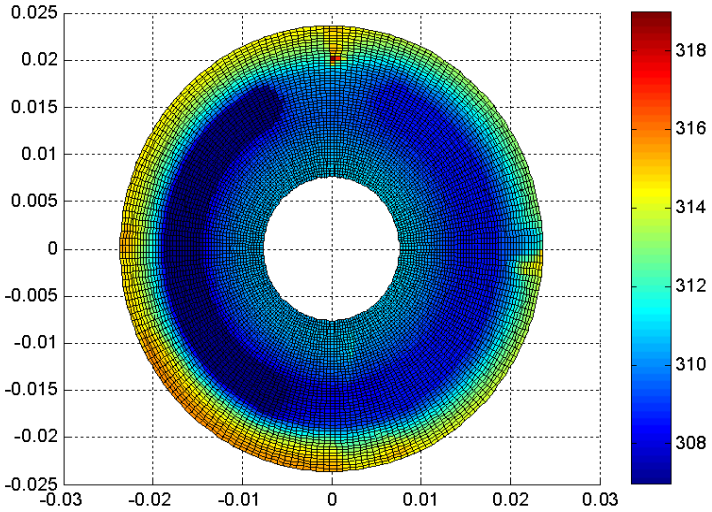

b) 4-pocket

Figure 5.20: Lubricant Temperature in Kelvin at 1200 psi (8.27MPa), 1800 rpm, z = 0.5h

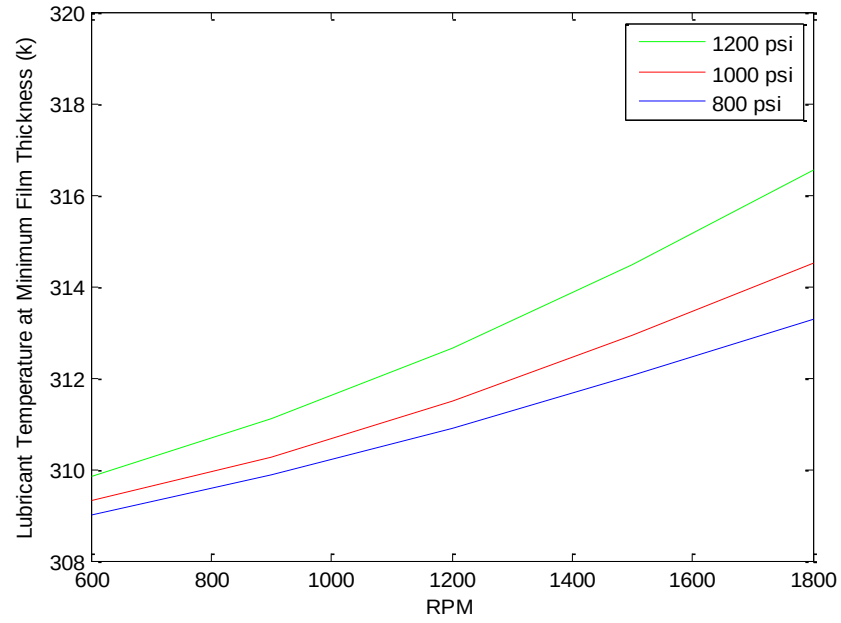

a) 8-pocket

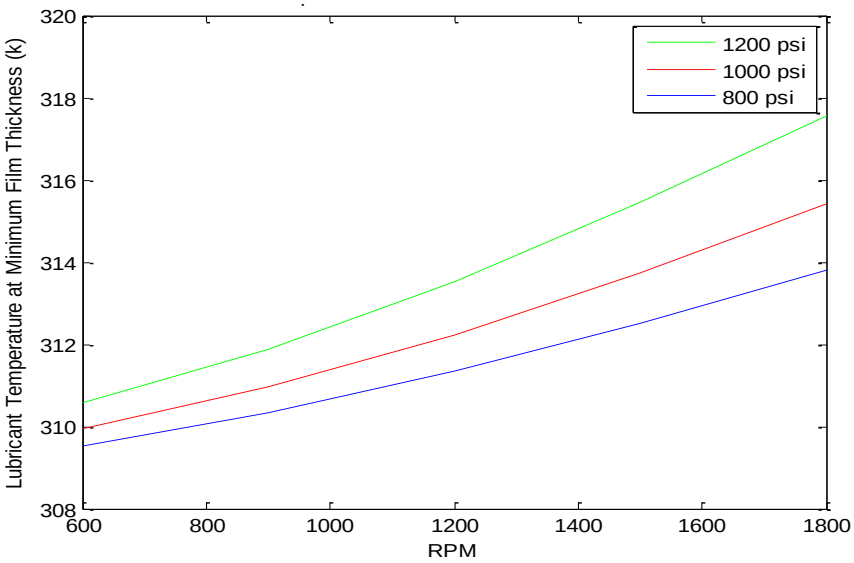

b) 4-pocket

Figure 5.21: Lubricant Temperature at Location of Minimum Film Thickness vs. Operating Conditions for the 4 and 8-Pocket Designs

5.6 Conclusions

In this investigation, an axial piston pump with floating valve plate was instrumented with three proximity probes to measure the displacement (film thickness) of the floating valve plate under various operating conditions. A lubrication model was also developed using the thermal Reynolds augmented with the JFO boundary condition and energy equation to determine the valve plate motion, lubricant pressure, cavitation, and temperature. Elastic deformation was also considered and calculated using an influence coefficient method as described by Zecchi and Ivantysynova [2012].

In the dynamic model, the balance pistons which support the valve plate were replaced by equivalent spring dashpot systems. The spring and damping coefficients were determined through a parametric study described by Richardson et al. [2017]. An analysis was then performed across all operating conditions and excellent correlation was observed between the measured and calculated film thicknesses. The resulting calculated pressure profiles showed an increase and decrease at the location of minimum film thickness due to the converging and diverging geometries. The amount of calculated elastic deformation from the lubricant pressures was minimal and found to be at most 0.243 microns. This small calculated elastic deformation confirms that the valve plate can be considered to behave rigidly for the operating conditions considered in this investigation. The lubricant temperature was found to be at a maximum at the location of minimum film thickness. At this location the lubricant shear is also at a maximum causing the spike in temperature. The temperature was also found to increase with an increase in operating speed and pressure.

Surface modifications were then added in a 4 and 8-pocket design around the floating valve plate in the dynamic lubrication model and an analysis was performed across the various operating conditions. Due to the rapid converging and diverging geometries of the pocket, gaseous cavitation was observed at the pocket locations as well as a sharp increase in lubricant pressure. The increase in pressure due to the pockets resulted in larger film thicknesses and lower lubricant temperatures. At the operating condition of 1200 psi (8.27 MPa) the 4 and 8-pocket designs showed an average increase in minimum film thickness of 0.81 μm and 1.12 μm, and an average decrease in temperature at the location of minimum film thickness of 2.16° C and

2.89° C. These trends can be seen across all operating conditions and demonstrate that the addition of pockets on a floating valve plate improves the lubricating conditions.

6. SUMMARY, CONCLUSIONS AND FUTURE WORK

6.1 Summary and Conclusions

Chapter 1 presents a background on axial piston pumps. It discusses the previous researchers' investigations on the tribological interfaces in an axial piston pump. For example, E. Koc et al. [1992] presented the experimental and theoretical investigation of the effect of clamping ratio and orifice size on the performance of slippers in an axial piston pump. Zecchi and Ivantysynova [2012] have experimentally investigated the thermal effects and deformation of the valve plate and its effect on the lubricating pressure. Surface modifications have been used to mitigate wear that occurs in axial piston pumps and between lubricated surfaces. Chacon et al. [2014] developed a numerical model to investigate the effects of adding a wavy surface texture to the valve plate. Etsion et. al. [2000] and Wang et al. [2012] experimentally investigated surface modifications and demonstrated an improvement in the friction and wear of their bearing surfaces.

Chapter 2 described a novel approach for measuring floating valve plate motion and the film thickness between the valve plate and the cylinder block. An axial piston pump apparatus (APPA) was developed and operated at a given condition while the film thickness was measured through the use of three non-contact proximity probes. The minimum film thickness and Δfilm thickness where then compared across all operating conditions. Results showed that the discharge pressure had a significant effect on both the minimum film thickness and Δfilm thickness. As the pressure was increased the minimum film thickness decreased whereas the Δfilm thickness increased. As the operational speed a slight increase in the minimum film thickness was also observed. The experimentally measured film thicknesses were then used in a Reynolds lubrication model to calculate the pressures that occur between the valve plate and cylinder block. Appropriate boundary conditions such as, instantaneous piston pressure and the inlet and outlet pressures were applied to the model. The calculated pressures illustrated a peak immediately followed by a drop in pressure at the location of minimum film thickness. This was due to the converging and diverging geometries that occur at the location of minimum film thickness. It was showed that the location of minimum film thickness always occurred on the inlet side of the pump at an angular location of between 170-190 degrees. Due to the vibrations

that occur in the valve plate, the resulting pressures illustrated a pulsation that occurs due to the squeeze effect of the lubricant.

Chapter 3 focused on developing a dynamic lubrication model to predict floating valve plate motion. The equations of motion of the floating valve plate were developed by summing the forces and moments about the center of mass. The valve plate was determined to have 3 degrees of freedom with the balance pistons which support the valve plate being represented as springs and dashpot. The equations of motion were then coupled with the Reynolds cavitation model by reducing the calculated pressures to an equivalent force and location.

The spring and damping coefficients for that represent the balance pistons were determined through the logarithmic decrement method. The resulting spring and damping coefficients were $5.10x10^7$ N/m and $3.34x10^4$ Ns/m, respectively. The calculated minimum and Δfilm thicknesses calculated using these spring and damping coefficients did not compare well to the experimental results. Due to the fully flooded environment during valve plate operation, additional lubricant pressures could not be accounted for using the logarithmic decrement method and therefore it could not accurately measure the stiffness and damping of the valve plate system. Using a parametric study new stiffness and damping coefficients were calculated to be $8.72x10^7$ N/m and $6.51x10^5$ Ns/m respectively. These coefficients resulted in excellent corroboration between the experiments and the model.

Chapter 4 investigated lubricant flow out of pocketed thrust washers at various speeds. A thrust washer test rig (TWTR) was developed to visualize lubricant flow using Micro Particle Image Velocimetry (μPIV). The measured flow fields showed flow reversal that occurred after the reformation boundary in the pocket. In addition, the cavitation areas were measured and compared at different operating conditions and illustrated that an increase in speed or viscosity resulted in an increase in cavitation area.

A numerical model was then developed which calculated the 3D velocity fields of the lubricant at the desired operating conditions. The calculated velocity fields also demonstrated flow reversal after the reformation boundary. In addition, the analytic cavitation areas corroborated well with the experiments. Through the use of a novel interpolation method the z-location of the experimental velocities could be calculated by comparison with the analytical velocity fields. The interpolated 3D velocity fields demonstrated that the lubricant in the pocket

was trapped in a recirculation vortex and that much of the lubricant was actually passing over the pocketed thrust washer.

Chapter 5 illustrated how surface modifications affect the lubricating conditions at the valve plate/cylinder block interface. A lubrication model was also developed using the thermal Reynolds augmented with the JFO boundary condition and energy equation to determine the valve plate motion, lubricant pressure, cavitation, and temperature. Elastic deformation was also considered and calculated using an influence coefficient method as described by Zecchi and Ivantysynova [2012].

The resulting calculated pressure profiles showed an increase and decrease at the location of minimum film thickness due to the converging and diverging geometries. The amount of calculated elastic deformation from the lubricant pressures was minimal and found to be at most 0.243 microns, meaning that the valve plate can be assumed to behave rigidly. The lubricant temperature was found to be at a maximum at the location of minimum film thickness. At this location the lubricant shear is also at a maximum causing the spike in temperature. With the addition of pockets on the valve plate, gaseous cavitation was observed at the pocket locations as well as a sharp increase in lubricant pressure. The increase in pressure due to the pockets resulted in larger film thicknesses and lower lubricant temperatures. At the operating condition of 1200 psi (8.27 MPa) the 4 and 8-pocket designs showed an average increase in minimum film thickness of 0.81 μm and 1.12 μm, and an average decrease in temperature at the location of minimum film thickness of 2.16° C and 2.89° C. These trends can be seen across all operating conditions and demonstrate that the addition of pockets on a floating valve plate improves the lubricating conditions.

In conclusion, these experiments and simulations demonstrated the behavior and motion of a floating valve plate, the lubricant will flow in a pocketed thrust washer under similar loading conditions, and how surface modifications like pockets will affect the lubricant temperature and valve plate deformation. Analysis of pressure profiles between the valve plate and cylinder block provided valuable insight into the locations of potential cavitation and wear. Enhanced simulations using the dynamic equation of the floating valve plate are providing new methods to simulate valve plate motion. Further development of both experimental measurements and

simulation techniques will lead to a greater understanding of the lubricant flow between the valve plate/cylinder block interface.

6.2 Future Work

6.2.1 Flow Visualization in Axial Piston Pump

In this study, μPIV was applied to acquire velocity vectors of a flow field. The future application of this technique could be to measure the flow and visualize any cavitation that might occur in the lubricant between the floating valve plate and cylinder block. A new Lexan housing seen in Figure 6.1 has been developed which allows for complete visualization of the pump during operation. Using μPIV will allow for the shear driven lubricating flow between the valve plate and cylinder block to be measured from a side view of the pump similar to Wang et al. [2012]. The valve plate motion and film thickness between the valve plate and cylinder block could also be measured using an image correlation technique with a side view. Additionally the valve plate can be modified with surface modifications and using μPIV optimization tests can be performed to determinte the best surface geometry for the valve plate/cylinderblock interface.

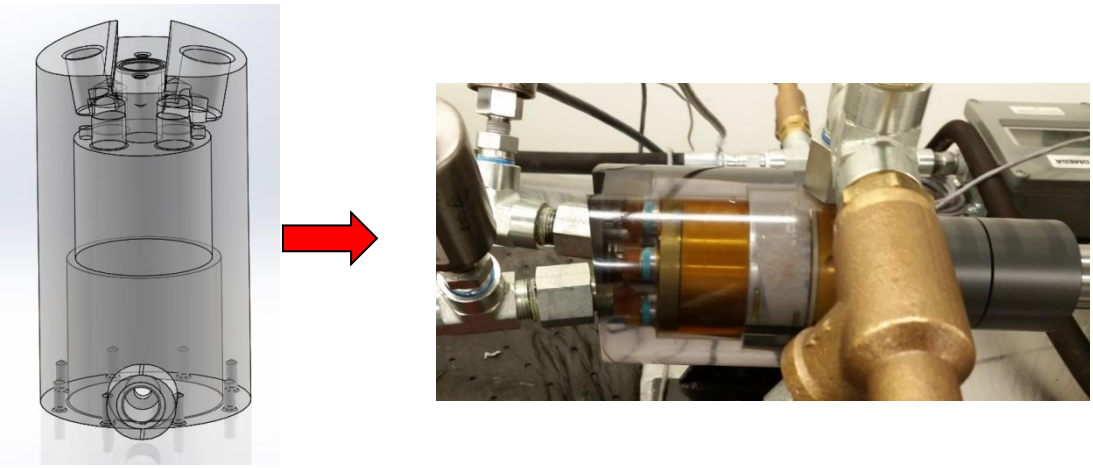

Figure 6.1: Lexan Housing Design

Attempts have already been made to measure the film thickness between the valve plate and cylinder block using visualization techniques. Using the current lexan housing and a high speed camera the lubricating gap was measured at an operating speed of 600 RPM and a frame rate of 1000 fps illustrated in Figure 6.2. The vibrations measured using this method are very similar in frequency to the vibrations measured using the proximity probes as demonstrated in

the FFT analysis in Figure 6.3. The frequency of the valve plate vibration directly correlates to the operating frequency of the pump, just as was observed using the proximity probes.

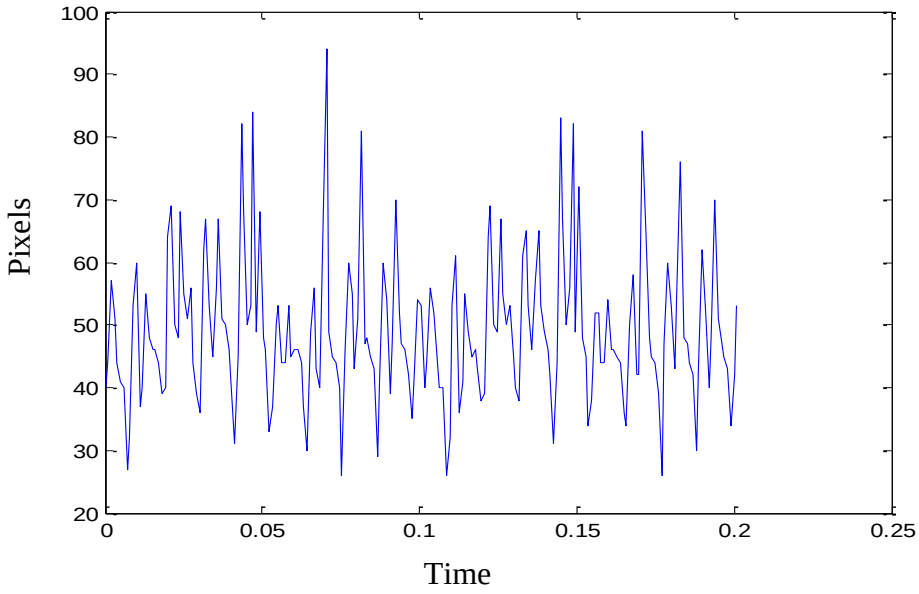

Figure 6.2: Film Thickness Measured using Lexan Housing

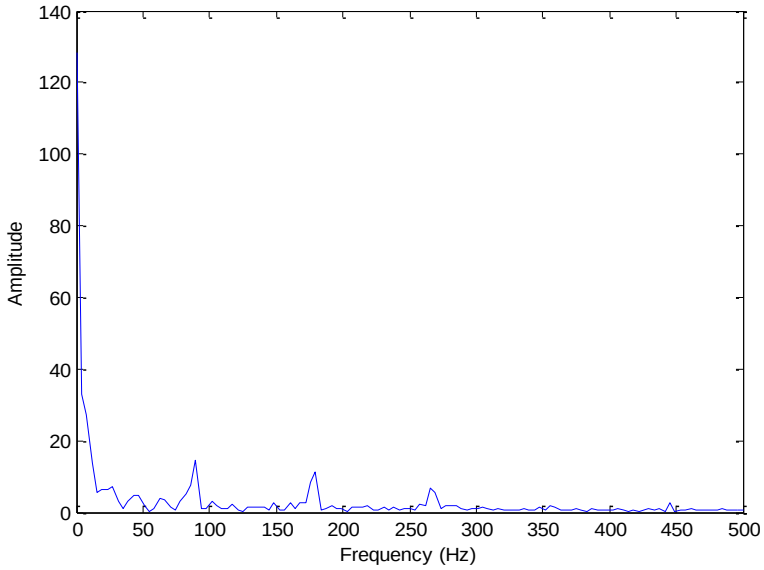

Figure 6.3: FFT Analysis of Visualized Film Thickness Measurements

Plans could also be made to create a clear valve plate, which will allow for a top view of the lubricant flow. A top view will allow for μPIV measurements to be taken at various points across the valve plate simultaneously. Utilizing the interpolation approach described in chapter 4, the measured velocity field could then be interpolated to 3D velocity fields allowing for a more critical examination of the flow between a floating valve plate and cylinder block.

6.2.2 Lubricant Effects on Axial Piston Pump Performance

The ability to generate a lubricant film between the parts is completely heavily dependent on the physical properties of the lubricant. For the previous investigations, the lubrication conditions were favorable with low loads, high viscosity lubricants, and well-designed contact geometries. Using the existing model and test rigs, surface modifications could be optimized for use in more extreme conditions. In application fuel (jet, diesel, or gasoline) is often used as a lubricant. Fuel often results in less than optimal lubrication conditions. JP8-100 jet fuel has a viscosity over 200 times lower than 0W-40 motor oil at the same temperature. Low viscosity means lower film thicknesses and delayed transition to the hydrodynamic regime leading to higher friction and wear. If pockets can be designed and implemented for these low viscosity lubricants, they could speed the transition to the hydrodynamic regime and maintain minimal wear at the lubricating interface.

Geometries can be first simulated using the dynamic lubrication model with the desired low viscosity fuels. Designs can be optimized using the proven numerical model; if pockets are found ineffective, then a number of other surface feature designs can be evaluated. Each application will have an optimal design but external system requirements and manufacturing capabilities may require compromises that can be evaluated. The adaptability of both the APPA and the TWTR will lend well to changing experimental requirements, and testing a variety of designs. Applications ranging as high as 3600 rpm at significant contact pressures can easily be tested using existing equipment.

The models and experimental tools developed here can be applied and scaled to many future applications. As previously described many invesitigations have been performed at the slipper/swashplate and piston/cylinder block interface. The dynamic lubrication model can account for new interfaces by simply changing geometry definition and the material and operational variables. The tools are robust and easily adapted to changing needs.

REFERENCES

Bergada, J.M., Davies, D.L., Kumar, S., and Watton, J., (2011),"The Effect of Oil Pressure and Temperature on Barrel Film Thickness and Barrel Dynamics of an Axial Piston Pump," *Meccanica*, **47**(3), pp. 639-654

Boncompain, R., Fillon, M. and Frene, J., " Analysis of Thermal Effects in Hydrodynamic Bearings," *ASME Journal of Tribology* **108**(2): 219-224, 1986

Chen H. X., Patrick, S. K,. Chua and Lim, G. H., (2006), " Dynamic vibration analysis of a swash-platetype water hydraulic motor," *Mechanism and Machine Theory*, Volume 41, Issue 5, pp. 487-504.

Chacon, R. (2014). An Investigation of the Impact of Micro Surface on the Cylinder Block/Valve Plate Interface Performance. In: *Proceedings of the* 7*th FPNI PhD Symposium*

Cross, A. T., Sadeghi, F., Rateick, R. G., Rowan, S., and Laboda, D., 2015, "Temperature Distribution in Pocketed Thrust Washers," Tribology Transactions, **58**(1), pp 31–43.

Cross, A. T., Sadeghi, F., Cao, L., Rateick, R. G., and Rowan, S., 2012, "Flow Visualization in a Pocketed Thrust Washer," Tribol. Trans., **55**(5), pp. 571–581.

Cross, A. T., Sadeghi, F., Rateick, R. G., and Rowan, S., 2013, "Hydrodynamic Pressure Generation in a Pocketed Thrust Washer," Tribol. Trans., **56**(4), pp. 652–662.

EDPIV was completed at the National Center for Physical Acoustics (NCPA) at the University of Mississippi in cooperation with the Micro Fluidics Laboratory at Purdue University for micro-scale PIV application. http://www.edpiv.com

Elrod, H. G. (1981), "A Cavitation Algorithm," Journal of Lubrication Technology, **103**, pp 350–354.

Etsion, I., Klingerman, Y. and Halperin, G. (1999), "Analytical and Experimental Investigation of Laser-Textured Mechanical Seal Faces," Tribology Transactions, **42**(3), pp 511-516.

Franco, N., (1961), "Pump Design by Force Balance," *Hydraulics and Pneumatics*, **14**(11), pp. 101-107

Fogg, A., 1949, "Fluid Film Lubrication of a Parallel Thrust Surface," Proc. Inst. Mech. Eng., **55**, p. 49.

Gui, L. and Wereley, S. T. (2002), "A Correlation-Based Continuous Window-Shift Technique to Reduce the Peak-Locking Effect in Digital PIV Image Evaluation," Experiments in Fluids, **32**, pp 506-517.

Han, L., Wang, S., and Zhang, C., (2014), "A partial lubrication model between valve plate and cylinder block in axial piston pumps," *Journal of Mechanical Engineering Science,* **229**(37), pp. 3201–3217.

Holman, J.P. *Heat Transfer*. 8th ed. New York: McGraw Hill,1997

Ivantysyn, J. and Ivantysynova, M. Hydrostatic Pumps and Motors. New Delhi, India: Technip Books International, 2001

Ivantysynova, M., Huang, C. and Christiansen, S.-K., (2004), "Computer Aided Valve Plate Design - An Effective Way to Reduce Noise,"*Proceedings of the SAE Commercial Vehicle Engineering Congress & Exhibition,* Chicago, IL, USA. SAE Technical Paper 2004-01-2621.

Ivantysynova, M. and S.K. Christiansen, (2005), "Automatic Valve Plate Design based on optimized Pressure Profile,"*IFPE Technical Conference,* Las Vegas, USA. Technical Paper NCFP I05-14.1.

Jakobsson, B., and Floberg, L., 1957, "The Finite Journal Bearings Considering Vaporization," Trans. Chalmers University of Technology, Gotenburg, Sweden, **190**, pp. 1–116.

Jakobsson, B., and Floberg, L., 1957, ‘‘The Finite Journal Bearings Considering Vaporization,’’ Trans. Chalmers University of Technology, Gotenburg, Sweden, **190**, pp. 1–116.

Kim, J.-K., Kim, H.-E., Lee, Y.-B., Jung, J.-Y., and Oh, S.-H., (2005), “Measurment of fluid film thickness on the valve plate in oil hydraulic axial piston pumps (Part II: Spherical design effects),” *J. Mech. Sci. Technol.*, **19**(2), pp. 655–663.

Kim, J.-K., and Jung, J.-Y., (2003), “Measurment of fluid film thickness on the valve plate in oil hydraulic axial piston pumps (Part I: Bearing Pad Effects),” *KSME International*, **17**(2), pp. 246-153.

Koc, E., Hooke, C., and Li, K., (1992), “Slipper Balance in Axial Piston Pumps and Motors,” Transactions of the ASME, v. 114, pp.766-772

Latas, W., Stojek, J., (2011), “Dynamic Model of Axial Piston Swash-Plate Pump for Diagnostics of Wear in Elements,” *Archive of Mechanical Engineering*, **58**(2), pp. 135-155

Meinhart, C.D., Wereley, S.T. and Santiago, J.G. (1999), “PIV Measurements of a Microchannel Flow,” Experiments in Fluids, **27**, pp 414-419.

Mizell, D., and Ivantysynova, M. Material Combinations for the Piston-Cylinder Interface of Axial Piston Machines: A Simulation Study. In: 8th FPNI Ph.D Symposium on Fluid Power, Lappeenrata, Finland, 11-3 June 2014, Technical Paper FPNI2014-7841.

Nishimura T., Umeda T., Tsuta T., Fujimara M., Kamakami M., (1995), “Dynamic response analysis of a swash-plate type hydraulic piston pump,” *ASME*, pp.145-155.

O’Hern, T. J., Torczynski, J. R., Blanchat,T. K., Chu, T. Y. and Tassin, A. L. (1994), “Shear-Driven Flow in a Square Cavity: A Comparative Study Using PIV, LDV, and Computational Simulations”, *Laser Anemometry-1994: Advanced and Applications, ASME*, v.191, pp.135-142

Qiu, Y. and Khonsari, M. M. (2009), "On the Prediction of Cavitation in Dimples Using a Mass-Conservative Algorithm," Journal of Tribology, **131**, pp 041702–1–041702–11.

Payvar, P., and Salant, R. F. "A Computational Method for Cavitation in Wavy Mechanical Seal" *ASME Journal of Tribology 1992*; **114**: 199–204.

Ryk, G., Klingerman, Y. and Etsion, I. (2002), "Experimental Investigation of Laser Surface Texturing for Reciprocating Automotive Components," *Tribology Transactions*, **45**(4), pp 444-449.

Richardson, D., Sadeghi, F., Rateick, R. G., and Rowan, S. "Experimental and Analytical Investigation of Floating Valve Plate Motion in an Axial Piston Pump" *Tribology Transactions* 2017; **60**:537 - 547

Shaw, M. C., 1947, "An Analysis of the Parallel-Surface Thrust Bearing," Trans. ASME, **69**, p. 381.

Shen, C., Khonsari, M. M. :On the Magnitude of Cavitation Pressure of Steady-State Lubrication," *Tribology Letters* 2013; **51**:pp 153-160.

Taneda, S. (1979), "Visualization of Seperating Stokes Flows," *Journal of the Physical Society of Japan*, v.46, n.6, pp.1935-1942

Vacca, A., Klop R. and Ivantysynova, M. (2010), "A Numerical Approach for the Evaluation of The Effects of Air Release And Vapour Cavitation on Effective Flow Rate of Axial Piston Machines," *International Journal of Fluid Power*, Vol. 11, No. 1, pp. 33 - 46.

Vaidya, A. and Sadeghi, F. (2008), "Hydrodynamic Lubrication of Scroll Compressor Thrust Bearing with Grooves and Circular Pockets," ASHRAE Transactions, **114**(2), pp 411–421.

Vaidya, A. and Sadeghi, F. (2009), "Experimental Investigation of Orbiting Thrust Bearing Using Wide and Shallow Circular Pockets," ASHRAE Transactions, **115**(2), pp 668–675.

Vijayaraghavan, D., Keith, T.G., (1989), "Development and Evaluation of a Cavitation Algorithm," *Tribology Transactions*,32:2, pp.225-233

Wang, C., Sadeghi, F., Wereley, S. T., and Chung, H. (2009), "Investigation of Fluid Flow out of a Microcavity Using μPIV," Tribology Transactions, **52**(6), pp 817–832.

Wang, C., Sadeghi, F., Wereley, S. T., Rateick, R. G., Jr., and Scott, R. (2011), "Experimental Investigation of Lubricant Extraction from a MicroPocket," Tribology Transactions, **54(**3**)**, pp 404–416.

Wereley, S. T. and Gui, L. (2003), "A Correlation-Based Central Difference Image Correction (CDIC) Method and Application in a Four Roll Mill Flow PIV Measurement," Experiments in Fluids, **34**, pp 42-51

Yu, T. H. and Sadeghi, F. (2000), "Groove Effects on Thrust Washer Lubrication," Journal of Tribology, **123**, pp 295–304.

Yu, T. H. and Sadeghi, F. (2002), "Thermal Effect on Thrust Washer Lubrication," American Society of Mechanical Engineers, Journal of Tribology, **124**, pp 166–177.

Zhao, J., Sadeghi, F., and Nixon, H. M. (2000), "A Finite Element Analysis of Surface Pocket Effects in Hertzian Line Contact," Journal of Tribology, **122**, pp 47-54.

Zecchi, M. and Ivantysynova, M., (2012), "Cylinder block/valve plate interface - a novel approach to predict thermal surface loads," *Proceedings of 8th IFK International Conference on Fluid Power*, Dresden, Germany, Vol. 1, pp.285-298.

Zecchi, M. and Ivantysynova, M., (2012), “A novel approach to predict the cylinder block / valve plate interface performance in swash plate type axial piston

Zhang, X., Cho, J., and Nair, S. S., 2008, “Indexing Valve Plate Pump: Modeling and Control,” *Asian J. Control*, **5**(2), pp. 261–270.

APPENDIX - DETAILS OF THERMAL CAVITATION MODEL

The non-dimensional Reynolds Lubrication Equation is discretized using a finite volume formulation. This follows the derivation presented in Vijayaraghavan and Keith [1989] in polar coordinates and allowing for variable viscosity. Figure A1 shows the model orientation

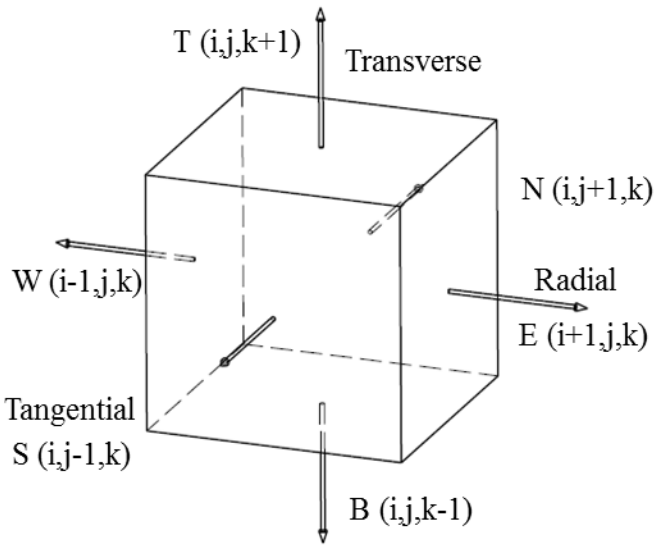

Figure A.1: Simulation Orientation.

Reynolds lubrication theory reduces the Navier-Stokes equations by neglecting inertia and assuming a thin film with minimal pressure variation across its thickness.

$$\frac{\partial}{\partial r}\left(\frac{\bar{r}\bar{\rho}\bar{h}^3}{12\bar{\eta}}\frac{\partial P}{\partial \bar{r}}\right)+\frac{1}{\bar{r}}\frac{\partial}{\partial \theta}\left(\frac{\bar{\rho}\bar{h}^3}{12\bar{\eta}}\frac{\partial P}{\partial \theta}\right)=\frac{\bar{r}\omega}{2}\frac{\partial}{\partial \theta}\left(\bar{\rho}\bar{h}\right)+\frac{\partial(\bar{\rho}\overline{\overline{h}})}{\partial t}$$

Elrod's Cavitation Algorithm for the JFO boundary condition accounts for gaseous or vaporous cavitation occurring in the fluid film. A switching function (F) changes the partial differential equation from elliptic in the full film region to hyperbolic in the cavitated region. The function activates when the pressure drops below the set cavitation pressure.

$$\frac{\partial}{\partial r}\left(\frac{\rho_C \bar{r}\bar{\beta}\bar{h}^3 F}{12\bar{\eta}}\frac{\partial\phi}{\partial\bar{r}}\right)+\frac{1}{\bar{r}}\frac{\partial}{\partial\theta}\left(\frac{\rho_C\bar{\beta}\bar{h}^3F}{12\bar{\eta}}\frac{\partial\phi}{\partial\theta}\right)=\frac{\bar{r}\omega\rho_C}{2}\frac{\partial}{\partial\theta}(\bar{h}\phi)+\ \frac{\partial(\phi\overline{\overline{h}})}{\partial t}$$

$$\beta=\rho\frac{\partial P}{\partial\rho}\therefore P=P_c+\beta\ln\phi\ \ where\ \phi=\frac{\rho}{\rho_c}$$

$$F=\begin{cases}1\ for\ \phi>1\\0\ for\ \phi\le 1\end{cases}$$

$$P=\begin{cases}P=P_c+\beta\ln\phi\ \ for\ \phi>1\\ \quad P=\ P_c\ \ for\ \phi\le 1\end{cases}$$

Non-dimensionalizing this scheme where viscosity variable "G" is defined in the following Viscosity Calculation section

$$\frac{\partial}{\partial r}\left(Grh^3F\frac{\partial\phi}{\partial r}\right)+\frac{1}{r}\frac{\partial}{\partial\theta}\left(Gh^3F\frac{\partial\phi}{\partial\theta}\right)=\gamma\frac{\partial}{\partial\theta}(rh\phi)+\ \frac{\gamma R_0}{\omega}\frac{\partial(\phi\bar{h})}{\partial t}\quad where\ \gamma$$
$$=\frac{\eta_0\omega R_0}{2h_0^2\beta};$$

The derivation is as follows:

$$H_{half}=h^3_{i\pm\frac{1}{2}}=\left(\frac{h_{i\pm1}+h_i}{2}\right)^3;\ r_{half}=r_{i\pm\frac{1}{2}}=\frac{r_{i\pm1}+r_i}{2};\ G_{half}=G_{i\pm\frac{1}{2}}=\frac{G_{i\pm1}+G_i}{2}$$

From Vijayaraghavan and Keith [1989], the switch function F is not explicitly differenced. This was the result of their efforts to provide a consistent scheme that could be centrally differenced.

$$F\frac{\partial\phi}{\partial\theta}=F\frac{\partial}{\partial\theta}(\phi-1)=\frac{\partial F(\phi-1)}{\partial\theta}-(\phi-1)\frac{\partial F}{\partial\theta}$$

The last term on the right hand side of the equation is shown to be zero for all values. F is zero in the cavitated region and $\partial F/\partial\theta$ is zero in the full film region. At the cavitation rupture and reformation boundaries $\phi = 1$ again resulting in the final term equaling zero. This is then applied to each of the terms in the non-dimensional Reynolds equation.

Pressure Driven Flow (θ – Direction N/S)

$$\frac{1}{r}\frac{\partial}{\partial\theta}\left(Gh^3F\frac{\partial\phi}{\partial\theta}\right)\rightarrow-\frac{1}{r}\frac{\partial}{\partial\theta}\left(Gh^3\frac{\partial F(\phi-1)}{\partial\theta}\right)_i$$

$$= -\frac{1}{rd\theta^2}\left[G_{i+\frac{1}{2}}h^3_{i+\frac{1}{2}}F_{i+1}(\phi_{i+1}-1) - \left(h^3_{i+\frac{1}{2}} + h^3_{i-\frac{1}{2}}\right)G_iF_i(\phi_i-1) + G_{i-\frac{1}{2}}h^3_{i-\frac{1}{2}}F_{i-1}(\phi_{i-1}-1)\right]$$

$$h^3_{i\pm\frac{1}{2}} = \left(\frac{h_{i\pm1}+h_i}{2}\right)^3 = H_{half};\ G_{i\pm\frac{1}{2}} = \left(\frac{G_{i\pm1}+G_i}{2}\right) = G_{half}$$

$$= -\frac{1}{r_Pd\theta^2}\big[G_{halfN}H_{halfN}F_N(\phi_N-1)$$
$$-\left(G_{halfN}H_{halfN}+G_{halfS}H_{halfS}\right)F_P(\phi_P-1)$$
$$+G_{halfS}H_{halfS}F_S(\phi_S-1)\big]$$

Pressure Driven Flow (r – Direction E/W)

$$\frac{\partial}{\partial r}\left(Grh^3F\frac{\partial\phi}{\partial r}\right) \rightarrow -\frac{\partial}{\partial r}\left(Grh^3\frac{\partial F(\phi-1)}{\partial r}\right)_j$$

$$= -\frac{1}{dr^2}\left[G_{j+\frac{1}{2}}r_{j+\frac{1}{2}}h^3_{j+\frac{1}{2}}F_{j+1}(\phi_{j+1}-1) - \left(G_{j+\frac{1}{2}}r_{j+\frac{1}{2}}h^3_{j+\frac{1}{2}} + G_{j-\frac{1}{2}}r_{j-\frac{1}{2}}h^3_{j-\frac{1}{2}}\right)F_j(\phi_j-1)\right.$$
$$\left. - G_{j-\frac{1}{2}}r_{j-\frac{1}{2}}h^3_{j-\frac{1}{2}}F_{j-1}(\phi_{j-1}-1)\right]$$

$$= -\frac{1}{dr^2}\big[G_{halfE}r_{halfE}H_{halfE}F_E(\phi_E-1)$$
$$-\left(G_{halfE}r_{halfE}H_{halfE}+G_{halfW}r_{halfW}H_{halfW}\right)F_P(\phi_P-1)$$
$$-G_{halfW}H_{halfW}F_W(\phi_W-1)\big]$$

Shear Flow:

$$E = \frac{r\omega\rho_c}{2}h\phi$$

$$\frac{\partial}{\partial\theta}\left[\frac{r\omega\rho_c}{2}h\phi\right]_i = \frac{E_{i+\frac{1}{2}}-E_{i-\frac{1}{2}}}{d\theta} - \frac{1}{2}\left[\left(F\frac{\partial E}{\partial\theta}\right)_{i+\frac{1}{2}} - \left(F\frac{\partial E}{\partial\theta}\right)_{i-\frac{1}{2}}\right] = \frac{(aE_{i+1}+bE_i+cE_{i-1})}{2d\theta}$$

$$a = \frac{F_{i+1}+F_i}{2};\ b = 2-\frac{F_{i+1}+2F_i+F_{i-1}}{2};\ c = -\left[2-\frac{F_i+F_{i-1}}{2}\right]$$

$$= \frac{\gamma}{2d\theta}r_P\left[\left(\frac{F_N+F_P}{2}\right)h_N\phi_N + \left(2-\frac{F_N+2F_P+F_S}{2}\right)h_P\phi_P - \left(2-\frac{F_P+F_S}{2}\right)h_S\phi_S\right]$$

Time Dependent flow:

$$\frac{\gamma R_0}{\omega}\frac{\partial(\phi\bar{h})}{\partial t} = T_c\left(\frac{\phi^i H^i - \phi^{i-1}H^{i-1}}{\Delta t}\right), where\ T_c = \frac{\gamma R_0}{\omega}$$

$$A_P = -\frac{\gamma}{2d\theta}r_P h_P\left(2 - \frac{F_N}{2} - F_p - \frac{F_S}{2}\right) - \frac{1}{2r_P d\theta^2}F_P\left(H_{halfN}G_{halfN} + H_{halfS}G_{halfS}\right)$$
$$- \frac{1}{dr^2}F_P\left(r_{halfE}H_{halfE}G_{halfE} + r_{halfW}H_{halfW}G_{halfW}\right) - T_c\frac{H^i}{\Delta t}$$

$$A_N = -\frac{\gamma}{2d\theta}r_P h_N\left(\frac{F_N + F_P}{2}\right) + \frac{1}{r_P d\theta^2}H_{halfN}F_N G_{halfN}$$

$$A_S = -\frac{\gamma}{2d\theta}r_P h_S\left(-2 + \frac{F_S + F_P}{2}\right) + \frac{1}{r_P d\theta^2}H_{halfS}F_S G_{halfS}$$

$$A_E = \frac{1}{dr^2}r_{halfE}H_{halfE}F_E G_{halfE}$$

$$A_W = \frac{1}{dr^2}r_{halfW}H_{halfW}F_W G_{halfW}$$

$$S_P = -\frac{1}{r_P d\theta^2}\left[H_{halfN}F_N G_{halfN} - \left(H_{halfN}G_{halfN} + H_{halfS}G_{halfS}\right)F_P + H_{halfS}F_S G_{halfS}\right]$$
$$- \frac{1}{dr^2}\left[r_{halfE}H_{halfE}F_E G_{halfE} - \left(r_{halfE}H_{halfE}G_{halfE} + r_{halfW}H_{halfW}G_{halfW}\right)F_P\right.$$
$$\left. + r_{halfW}H_{halfW}F_W G_{halfW}\right] + T_c\frac{H^{i-1}\phi^{i-1}}{\Delta t}$$

$$A_P\phi_P + A_N\phi_N + A_S\phi_S + A_E\phi_E + A_W\phi_W + S_P = 0$$

This equation can now be solved using a Gauss-Seidel scheme with a Newton-Raphson root finding method.

Boundary Conditions:

Along the inner and outer radius the thrust washer is exposed to atmospheric conditions. This was then translated to the proper value of ϕ.

$$\bar{P} = P_a \rightarrow \phi = \exp\left(\frac{P_a - P_c}{\beta}\right) for\ r = R_I\ and\ r = R_O$$

Initially the film was considered fully liquid meaning F = 1 throughout the entire domain.

Viscosity Calculations

Viscosity is defined over a three dimensional domain corresponding to the temperature profile. Roelands' viscosity model [Roelands 1966] was used to predict the temperature-viscosity relationship.

$$\log\left(\log\left(\frac{\bar{\eta}}{1000.0}\right)+1.20\right) = -S_0\log\left[1+\frac{\overline{T}-273.15}{135.0}\right]+\log G_0$$

The constants S_0 and G_0 must be calibrated from experimental measurements. Viscosity is measured in centipoise and the temperature is presented in Celsius. The field must then be averaged for use in the Reynolds equation.

$$h = \frac{\overline{h}}{\overline{R_o}}, dz = \frac{h}{n_z}$$

$$F_1 = \int_0^1 \frac{z}{\eta}dz\,, F_2 = \int_0^1 \frac{1}{\eta}dz$$

$$J_1(z) = \int_0^z \frac{\psi}{\eta}d\psi, J_2(z) = \int_0^z \frac{1}{\eta}d\psi$$

$$J_1(1) = F_1, J_2(1) = F_2$$

$$G = \left(\frac{F_1}{F_2}\right)\int_0^1 J_2(z)dz - \int_0^1 J_1(z)dz\,;\ \eta_{2D\ avg} = \frac{1}{12G}\ (average\ viscosity\ across\ the\ film)$$

Temperature Calculations

Dimensional film energy equation (Pinkus 1990)

$$\rho C_f\left(\frac{\partial\bar{T}}{\partial\bar{t}}+V_r\frac{\partial T}{\partial r}+\frac{V_\theta}{r}\frac{\partial T}{\partial\theta}+V_z\frac{\partial T}{\partial z}\right)$$

$$= k_f\left(\frac{1}{r}\frac{\partial}{\partial r}\left(r\frac{\partial T}{\partial r}\right)+\frac{1}{r^2}\frac{\partial^2 T}{\partial\theta^2}+\frac{\partial^2 T}{\partial z^2}\right)+\eta\left[\left(\frac{\partial V_r}{\partial z}\right)^2+\left(\frac{\partial V_\theta}{\partial z}\right)^2\right]$$

Non-dimensionalizing the Thin-Film Energy equation and applying conservation of mass returns the following form of the energy equation.

r = non-dimensional radius ($\bar{r}/R_O$)

$h =$ non-dimensional film thickness ($\bar{h}/R_O$)

$$\left(\frac{1}{\omega t_o}\frac{\partial \bar{T}}{\partial \bar{t}} + \frac{1}{r}\frac{\partial (r\rho T V_r)}{\partial r} + \frac{1}{r}\frac{\partial \rho T V_\theta}{\partial \theta} + \frac{\partial (\rho V_z T)}{\partial z}\right)$$

$$= \frac{1}{Pe}\left(\frac{1}{r}\frac{\partial}{\partial r}\left(r\frac{\partial T}{\partial r}\right) + \frac{1}{r^2}\frac{\partial^2 T}{\partial \theta^2} + \frac{\partial^2 T}{\partial z^2}\right) + \Gamma\eta\left[\left(\frac{\partial V_r}{\partial z}\right)^2 + \left(\frac{\partial V_\theta}{\partial z}\right)^2\right]$$

$$Pe = \frac{\rho_c C_f \omega R_0^2}{k_f};\ \Gamma = \frac{\eta_0 \omega}{\rho_c C_f T_0};\ h = \frac{\overline{h}}{\overline{R_o}};\ dz = \frac{h}{n_z};\ P = \frac{\bar{P} + P_a}{P_a - P_c};\ r = \frac{\bar{r}}{R_O}$$

In vector form [Yu and Sadeghi 2002]

$$\nabla \cdot (\bar{U} \cdot \rho T) = \frac{1}{Pe}\left(\nabla \cdot (\nabla T)\right) + \Gamma\eta\left[\left(\frac{\partial V_r}{\partial z}\right)^2 + \left(\frac{\partial V_\theta}{\partial z}\right)^2\right]$$

Using Divergence Theorem

$$\int_{CV} \nabla \cdot \vec{B} dV = \int_{CS} \vec{B} \cdot \vec{n} dS$$

$$\int_{CS} \rho T(\bar{U} \cdot \hat{n}) dS = \frac{1}{Pe}\int_{CS} (\nabla T \cdot \hat{n}) dS + \int_{CV} \Gamma\eta\left[\left(\frac{\partial V_r}{\partial z}\right)^2 + \left(\frac{\partial V_\theta}{\partial z}\right)^2\right] dV$$

For surface W:

$$\hat{n} = -\hat{e}_r, \widehat{U} \cdot \hat{n} = -V_r$$

$$\nabla T \cdot \hat{n} = -\frac{\partial T}{\partial r}$$

$$dS = r d\theta dz$$

For surface S:

$$\hat{n} = -\hat{e}_\theta, \widehat{U} \cdot \hat{n} = -V_\theta$$

$$\nabla T \cdot \hat{n} = -\frac{\partial T}{\partial \theta}$$

$$dS = dr dz$$

For surface B:

$$\hat{n} = -\hat{k}, \widehat{U} \cdot \hat{n} = -V_z$$

$$\nabla T \cdot \hat{n} = -\frac{\partial T}{\partial z}$$

$$dS = rdrd\theta$$

Control Volume:

$$dV = rdrd\theta dz$$

The surfaces E, N, and T are the same with a reversed sign.

Integrating the first term results in the spatial convective terms

$$\int_{CS} \rho T(\overline{U} \cdot \hat{n}) dS = F_E T_E - F_W T_W + \mathrm{F_N T_N} - \mathrm{F_S T_S} + \mathrm{F_T T_T} - \mathrm{F_B T_B}$$

$$F_W = (\phi V_r r)_W dtdz; \;\; F_E = (\phi V_r r)_E dtdz$$

$$F_S = (\phi V_\theta)_S drdz; \;\; F_N = (\phi V_\theta)_N drdz$$

$$F_B = (\phi V_Z)_B rd\theta dr; \;\; F_T = (\phi V_z) rd\theta dr$$

Integrating the second term produces the conduction coefficients

$$\frac{1}{Pe}\int_{CS} (\nabla T \cdot \hat{n}) dS = -D_S \Delta T_S + D_N \Delta T_N - D_W \Delta T_W + D_E \Delta T_E - D_B \Delta T_B + D_T \Delta T_T$$

where

$$D_W = \frac{r_W d\theta dz}{Pe\ dr}; \;\; D_E = \frac{r_E d\theta dz}{Pe\ dr}$$

$$D_S = \frac{drdz}{Pe\ d\theta}; \;\; D_N = \frac{drdz}{Pe\ d\theta}$$

$$D_B = \frac{rdrd\theta}{Pe\ dz}; \; D_T = \frac{rdrd\theta}{Pe\ dz}$$

Source Term:

$$S_P = \Gamma\eta \left[\left(\frac{\partial V_\theta}{\partial z}\right)^2 + \left(\frac{\partial V_r}{\partial z}\right)^2 \right] rdrd\theta dz \; + \phi T^{i-1} \frac{rdrd\theta dz}{\Delta t\ \omega}$$

The solution method for A is described by Patankar's Power Law scheme. The operator [X, Y] chooses the larger of the two values X and Y.

$$A_W = D_W \left[0, \left(1 - 0.1 \left|\frac{F_W}{D_W}\right|\right)^5 \right] + [F_W, 0]$$

$$A_E = D_E\left[0,\left(1-0.1\left|\frac{F_E}{D_E}\right|\right)^5\right]+[-F_E,0]$$

$$A_S = D_S\left[0,\left(1-0.1\left|\frac{F_S}{D_S}\right|\right)^5\right]+[F_S,0]$$

$$A_N = D_N\left[0,\left(1-0.1\left|\frac{F_N}{D_N}\right|\right)^5\right]+[-F_N,0]$$

$$A_B = D_B\left[0,\left(1-0.1\left|\frac{F_B}{D_B}\right|\right)^5\right]+[F_B,0]$$

$$A_T = D_T\left[0,\left(1-0.1\left|\frac{F_T}{D_T}\right|\right)^5\right]+[-F_T,0]$$

$$A_t = \phi\frac{rdrd\theta dz}{\Delta t\ \omega}$$

$$A_P = A_W + A_E + A_N + A_S + A_B + A_T + A_t$$

$$A_P T_P = A_W T_W + A_E T_E + A_S T_S + A_N T_N + A_B T_B + A_T T_T + A_t T_P + S_P \qquad ($$

Boundary Conditions:

Along the inner and outer radii:

$$\frac{\partial T}{\partial r} = 0$$

Periodic conditions were applied to the leading and trailing edges of the domain to represent the entire ring

$$T_{\theta=0} = T_{\theta=\frac{2\pi}{N_P}}$$

The upper and lower boundary conditions were defined by the conduction to the solid runner and pad surfaces.

$$q = -kA\frac{\partial T}{\partial z}\ where\ \frac{q}{A} = \frac{T_{2_{FLUID}} - T_{2_{SOLID}}}{\frac{\Delta z_{FLUID}}{k_{FLUID}} + \frac{\Delta z_{SOLID}}{k_{SOLID}}}$$

Once the heat flow per unit area was solved the temperatures on the boundaries were solved.

$$\frac{q}{A} = k_{FLUID}\frac{T_{2_{FLUID}} - T_{1_{FLUID}}}{\Delta z_{FLUID}} = k_{SOLID}\frac{T_{2_{SOLID}} - T_{1_{SOLID}}}{\Delta z_{SOLID}}$$

The energy flow rate (q/A) was reduced in the cavitation region by the density ratio ($\rho/\rho_c = \phi$).

For the velocity calculations, J_1, J_2, F_1, and F_2 are defined as before

$$V_\theta = \frac{6h^2}{\gamma r}\frac{\partial P}{\partial \theta}\left[J_1(z) - \frac{F_1}{F_2}J_2(z)\right] + r\left[1 - \frac{J_2(z)}{F_2}\right]$$

$$V_r = \frac{6h^2}{\gamma}\frac{\partial P}{\partial r}\left[J_1(z) - \frac{F_1}{F_2}J_2(z)\right]$$

Valve Plate Energy Equation

$$0 = \left(\frac{1}{r}\frac{\partial}{\partial r}\left(r\frac{\partial T}{\partial r}\right) + \frac{1}{r^2}\frac{\partial^2 T}{\partial \theta^2} + \frac{\partial^2 T}{\partial {z_P}^2}\right)$$

$$dz_P = \frac{D_P}{n_{ZP}R_O}$$

Integrating over the control volume

$$dV = rdrd\theta dz_P$$

$$\iiint_{B\,S\,W}^{T\,N\,E}\left(\frac{1}{r}\frac{\partial}{\partial r}\left(r\frac{\partial T_P}{\partial r}\right) + \frac{1}{r^2}\frac{\partial^2 T_P}{\partial \theta^2} + \frac{\partial^2 T_P}{\partial {z_P}^2}\right)rdrd\theta dz_P = 0$$

$$\iiint_{B\,S\,W}^{T\,N\,E}\left(\frac{1}{r}\frac{\partial}{\partial r}\left(r\frac{\partial T_P}{\partial r}\right)\right)rdrd\theta dz_P = \left[\left(r\frac{\partial T_P}{\partial r}\right)_E - \left(r\frac{\partial T_P}{\partial r}\right)_W\right]d\theta dz_P$$

$$\iiint_{B\,S\,W}^{T\,N\,E}\left(\frac{1}{r^2}\frac{\partial^2 T_P}{\partial \theta^2}\right)rdrd\theta dz_P = \left[\left(\frac{1}{r}\frac{\partial T_P}{\partial \theta}\right)_N - \left(\frac{1}{r}\frac{\partial T_P}{\partial \theta}\right)_S\right]drdz_P$$

$$\iiint_{B\,S\,W}^{T\,N\,E}\left(\frac{\partial^2 T_P}{\partial {z_P}^2}\right)rdrd\theta dz_P = \left[\left(\frac{\partial T_P}{\partial z_P}\right)_T - \left(\frac{\partial T_P}{\partial z_P}\right)_B\right]rdrd\theta$$

$$A_W = \frac{rdtdz_P}{dr};\ A_E = \frac{rdtdz_P}{dr}$$

$$A_S = \frac{drdz_P}{rdt};\ A_N = \frac{drdz_P}{rdt}$$

$$A_B = A_T = \frac{rdrdt}{dz_P}$$

$$A_P = A_W + A_E + A_S + A_N + A_T + A_B$$

$$A_P T_P = A_E(T_P)_E + A_W(T_P)_W + A_N(T_P)_N + A_S(T_P)_S + A_T(T_P)_T + A_B(T_P)_B$$

Boundary Conditions:

Periodic conditions were applied for the temperature such that

$(T_P)_{\theta=0} = (T_P)_{\theta=\frac{2\pi}{N_P}}$.

Convective boundary conditions we added to the inner and outer radii of the pad to simulate oil in the flooded reservoir.

$$\frac{\partial T_P}{\partial r} = H_P(T_P - 1)\ at\ the\ inner\ radius;\quad \frac{\partial T_P}{\partial r} = -H_P(T_P - 1)\ at\ the\ outer\ radius$$

$$H_P = \frac{k_{vp}}{h_{FLUID} r dr R_O}$$

The lower surface was insulated such that $\frac{\partial T_P}{\partial z_P} = 0.$

Cylinder block Energy Equation

$$\frac{\partial T_R}{\partial \theta} = K_{cb}\left(\frac{1}{r}\frac{\partial}{\partial r}\left(r\frac{\partial T_R}{\partial r}\right) + \frac{1}{r^2}\frac{\partial^2 T_R}{\partial \theta^2} + \frac{\partial^2 T_R}{\partial z_R^2}\right)$$

$$dz_R = \frac{D_R}{n_{ZR} R_O};\ K_{RUN} = \frac{k_{cb}}{\rho_{cb} C_{cb} \omega}$$

Integrating over the control volume

$$dV = r dr d\theta dz_R$$

$$\iiint_{B\,S\,W}^{T\,N\,E} \left(\frac{\partial T_R}{\partial \theta}\right) r dr d\theta dz_R = K_{cb} \iiint_{B\,S\,W}^{T\,N\,E} \left(\frac{1}{r}\frac{\partial}{\partial r}\left(r\frac{\partial T_R}{\partial r}\right) + \frac{1}{r^2}\frac{\partial^2 T_R}{\partial \theta^2} + \frac{\partial^2 T_R}{\partial {z_R}^2}\right) r dr d\theta dz_R$$

where

$$\iiint_{B\,S\,W}^{T\,N\,E} \left(\frac{\partial T_R}{\partial \theta}\right) r dr d\theta dz_R = [(T_R)_N - (T_R)_S] r dr dz_R$$

$$\iiint_{B\,S\,W}^{T\,N\,E} \left(\frac{1}{r}\frac{\partial}{\partial r}\left(r\frac{\partial T_R}{\partial r}\right)\right) r dr d\theta dz_R = \left[\left(r\frac{\partial T_R}{\partial r}\right)_E - \left(r\frac{\partial T_R}{\partial r}\right)_W\right] d\theta dz_R$$

$$\iiint_{B\,S\,W}^{T\,N\,E} \left(\frac{1}{r^2}\frac{\partial^2 T_R}{\partial \theta^2}\right) r dr d\theta dz_R = \left[\left(\frac{1}{r}\frac{\partial T_R}{\partial \theta}\right)_N - \left(\frac{1}{r}\frac{\partial T_R}{\partial \theta}\right)_S\right] dr dz_R$$

$$\iiint_{B\,S\,W}^{T\,N\,E}\left(\frac{\partial^2 T_R}{\partial {z_R}^2}\right) r dr d\theta dz_R = \left[\left(\frac{\partial T_R}{\partial z_R}\right)_T - \left(\frac{\partial T_R}{\partial z_R}\right)_B\right] r dr d\theta$$

$$A_W = \frac{r dt dz_R}{dr};\ A_E = \frac{r dt dz_R}{dr}$$

$$A_S = \frac{dr dz_R}{r dt} + \left[\frac{r dr dz_R}{K_{cb}}, 0\right];\ A_N = \frac{dr dz_R}{r dt} + \left[-\frac{r dr dz_R}{K_{cb}}, 0\right]$$

$$A_B = A_T = \frac{r dr dt}{dz_R}$$

$$A_P = A_W + A_E + A_S + A_N + A_T + A_B$$

$$A_P T_P = A_E (T_R)_E + A_W (T_R)_W + A_N (T_R)_N + A_S (T_R)_S + A_T (T_R)_T + A_B (T_R)_B \qquad \text{(A.1)}$$

Boundary Conditions:

Periodic conditions were applied for the temperature such that

$(T_R)_{\theta=0} = (T_R)_{\theta=\frac{2\pi}{N_P}}$.

Convective boundary conditions we added to the inner and outer radii of the pad to simulate oil in the flooded reservoir.

$$\frac{\partial T_R}{\partial r} = H_R(T-1)\ at\ the\ inner\ radius;\ \frac{\partial T_R}{\partial r} = -H_R(T-1)\ at\ the\ outer\ radius$$

$$H_R = \frac{k_{cb}}{h_{FLUID} r dr R_O}$$

The lower surface was insulated such that $\frac{\partial T_R}{\partial z} = 0$

Load Calculations

$$L = \iint_{0\,R_I}^{2\pi\,R_O} \bar{P} r dr d\theta$$

Shear Force Calculations

$$\tau = \bar{\eta}\frac{\partial V_\theta}{\partial \bar{z}}$$

$$\tau = -\frac{\bar{h}}{2\bar{r}}\frac{\partial \bar{P}}{\partial \theta} - \frac{\bar{\eta}\bar{r}\omega}{\bar{h}}$$

$$f = N_P \iint_{\theta_i R_I}^{\theta_f R_O} \tau_B \bar{r} dr d\theta$$

$$f = N_P \sum_{i=1}^{n_R} \sum_{j=1}^{n_\theta} \left(\frac{-\bar{h}_{i,j}}{2\bar{r}_{i,j}} \left[\frac{\bar{P}_{i,j+1} - \bar{P}_{i,j-1}}{2d\theta} \right] - \frac{\omega \bar{\eta} \bar{r}_{i,j}}{\bar{h}_{i,j}} \right) \bar{r}_{i,j} dr d\theta$$

Convergence Tolerances

$$Film\ Temperature\ \frac{1}{N_Z N_R N_\theta} \sum_{1}^{N_Z} \sum_{1}^{N_R} \sum_{1}^{N_\theta} \left| \frac{T^{n+1} - T^n}{T^{n+1}} \right| < 1x10^{-10}$$

$$Valve\ Plate\ Temperature\ \frac{1}{N_{ZP} N_R N_\theta} \sum_{1}^{N_{ZP}} \sum_{1}^{N_R} \sum_{1}^{N_\theta} \left| \frac{T_P^{n+1} - T_P^n}{T_P^{n+1}} \right| < 1x10^{-8}$$

$$Cylinder\ Bl\ Temperature\ \frac{1}{N_{ZR} N_R N_\theta} \sum_{1}^{N_{ZR}} \sum_{1}^{N_R} \sum_{1}^{N_\theta} \left| \frac{T_R^{n+1} - T_R^n}{T_R^{n+1}} \right| < 1x10^{-8}$$

$$Pressure\ \frac{1}{N_R N_\theta} \sum_{1}^{N_R} \sum_{1}^{N_\theta} \left| \frac{\phi^{n+1} - \phi^n}{\phi^{n+1}} \right| < 1x10^{-6}$$